SYNTHESIS AND CHARACTERIZATION OF 5-FU LOADED MAGNETIC NANOCOMPOSITE SPHERES FOR ADVANCED DRUG DELIVERY

A Dissertation by

Humphrey Lusenaka Wamocha

MS, Physics, Wichita State University, 2003

B.ED, Science, Egerton University, 1998

Submitted to the Department of Mechanical Engineering

and the Faculty of the Graduate school of

Wichita State University

in partial fulfillment of

the requirements of the degree of

Doctor of Philosophy

August 2010

SYNTHESIS AND CHARACTERIZATION OF 5-FU LOADED MAGNETIC NANOCOMPOSITE SPHERES FOR ADVANCED DRUG DELIVERY

The following faculty members have examined the dissertation for form and content and recommend that it be accepted in the partial fulfillment of the requirement for the degree of Doctor of philosophy with a major in Mechanical Engineering.

_____

Ramazan Asmatulu, committee chair

We have read this Dissertation

and recommend its acceptance

_____

Tiruvadi Ravigururajan, Committee member

_____

Don Malzahn, committee member

_____

David Koert, committee member

_____

Shang-You Yang, Committee member

Accepted for the College of Engineering

_____

Zulma Toro-Ramos, Dean

Accepted for the Graduate School

_____

J. David McDonald, Dean

DEDICATION

To my Dad, –The cure is still out there”

ACKNOWLEDGMENTS

First, I would like to thank God for his guidance and provisions. Special thanks to my parents; Mom Joyce Lusenaka and my late father Allan Wamocha Lusenaka. Thanks to my wife Judy and my siblings for their love, support and encouragement on this long journey.

I would like to thank my advisor, Dr. R. Asmatulu, for his patience, input, guidance and tireless support in this research work. He has been a source of motivation to do more and achieve a higher level of excellence. I am forever grateful for the many hours we spend with him looking at ways to make this research work better.

I would also like to extend my gratitude to members of my committee Dr. Ravi, Dr. Malzahn, Dr. Koert and Dr. Yang for their helpful comments and suggestions in improving this research. Thanks are also due to Dr. James Ho for his support in characterizing the samples and for using his laboratory. He has encouraged me to ask and analyze beyond what is written

Special thanks to Dr. H. Hamdeh for the work done on sample characterization and the use of his lab. Thanks to Dr. Lankarani, Dr. Weheba, Dr. Nyakiti and Dr. Eltabey for getting this research moving forward. Thanks to Zheng Song, Tandel Rupali and Anusha Garikapati for their tireless support and help with cytotoxicity testing and CFD analysis. Thanks to Joanna Farmer, Lindsey Clark and all my friends who encouraged me to stay the course.

Finally, I am grateful to the Faculty of the Department of Mechanical engineering and the Department of Physics for the knowledge and support I have gained from them.

ABSTRACT

Magnetic targeted drug delivery, the science concerned with the design, characterization and use of magnetic materials as carriers of therapeutic agents presents promising advances in the study of drug delivery and pharmacokinetics. This is made possible by use of nanotechnology in the areas, such as engineering, biotechnology, chemistry and other sciences to develop new materials and mechanisms that can be channeled to improve the way diseases are identified and treated.

The aim of this research was to introduce the use of cobalt zinc ferrite ($Co_{0.5}Zn_{0.5}Fe_2O_4$) nanoparticles as magnetic materials that could be formulated and used for targeted drug delivery, and compare the results with the commonly used magnetite. This study focused on the preparation, characterization, particle flow characteristics and cytotoxicity evaluation of magnetic materials. Cobalt zinc ferrite and magnetite (Fe_3O_4) nanoparticles (~10 nm) were synthesized by chemical co-precipitation of initial reagents. An oil-in-oil emulsion/solvent evaporation technique was used to embed the magnetic nanoparticles (MNP) plus a sample drug in a biodegradable polymer poly (DL-lactide-co-glycolide) (PLGA) to produce a magnetic nanocomposite (MNC) spheres.

MNC spheres with different MNP concentrations (10%, 15%, 20%, and 25%) were prepared and characterized to determine their physical and magnetic properties by various techniques including; X-ray diffraction, dynamic laser light scattering (DLLS), scanning electron microscopy (SEM), Transmission electron microscopy (TEM), Mossbauer spectroscopy(MS) and superconducting quantum interference magnetometer (SQUID). The hydrodynamic flow

characteristics of MNP and MNC spheres were also evaluated using experimental techniques. The cytotoxicity effects of these materials on normal cells were further determined from in-vitro cell trials.

Results show that MNC spheres (200 nm to 1.1 μm in diameter) retained superparamagnetic properties when embedded with $Co_{0.5}Zn_{0.5}Fe_2O_4$ nanoparticles, and had a blocking temperature ranging from 120K to 140K and a saturation magnetization above 2,000 Oe. The magnetic properties of the embedded $Co_{0.5}Zn_{0.5}Fe_2O_4$ were close to those of magnetite. The effectiveness of these nanomaterials as carrier particles in drug delivery under various flow conditions depended on the vessel diameter, strength of magnetic field and concentration of MNP. An increase in the number of MNC captured could be achieved by increasing the MNP content, vessel diameter and magnetic field at optimal flow conditions. Cytotoxicity testing showed that the use of cobalt zinc ferrite delivery systems was viable though with some identifiable constraints when compared with magnetite. A reduction in sample concentration improved cell viability significantly making it potentially useful in drug delivery.

TABLE OF CONTENTS

TABLE OF CONTENTS (continued)

Chapter Page

TABLE OF CONTENTS (continued)

Chapter Page

TABLE OF CONTENTS (continued)

Chapter Page

LIST OF TABLES

LIST OF FIGURES

Figure Page

LIST OF FIGURES (continued)

Figure Page

LIST OF FIGURES (continued)

Figure Page

LIST OF FIGURES (continued)

Figure Page

LIST OF ABBREVIATIONS

ATCC	American Type Culture Collection
CAD	Computer Aided Design
CFD	Computational Fluid dynamics
DMEM	Dulbecco's Modified Eagle Medium
EDX	Energy Dispersive X-Ray
FBS	Fasting blood sugar
FC	Field Cooling
FDA	Food and Drug Administration
FU	Fluorouracil
IS	Isomer Shift
MNC	Magnetic Nanocomposite
MNP	Magnetic Nanoparticles
MS	Mossbauer Spectroscopy
MTT	(3-(4, 5-Dimethylthiazol-2-yl)-2,5-diphenyltetrazolium bromide
NCI	National Cancer Institute

LIST OF ABBREVIATIONS (continued)

PBS	Phosphate Buffered Saline
PLGA	Poly (d, l- Lactide –Co-Glycolide)
QS	Quadrupole Splitting
SEM	Scanning Electron Microscopy
SQUID	Superconducting Quantum Interference Device
TEM	Transmission Microscopy
XRD	X-Ray Diffraction
ZFC	Zero Field Cooling

LIST OF SYMBOLS

μ/ρ	Mass Absorption Coefficient
μ_B	Bohr Magneton
μm	Micrometer
μl	Microliter
E	Energy
KeV	Kilo Electron Volt
m	Mass
Q	Heat Supplied to Substance
S	Entropy
Sec	Second
T	Temperature (K)
T_B	Blocking temperature (K)
U	Internal Energy
Z	Atomic Number
βn	Half–Width of XRD Peak

LIST OF SYMBOLS (continued)

γ	Gamma Ray
λ	Wavelength
χ	Susceptibility
Θ	Diffraction Angle
Oe	Oersted
B	External magnetic flux (T)
F_M	Magnetic force (N)
F_D	Hydrodynamic drag force (N)
H	Magnetic field (A m^{-1})
d	Nanoparticles diameter

CHAPTER 1

INTRODUCTION

1.1 Targeted Drug Delivery

The idea behind targeted drug delivery can be traced back to the 1800s with a well disserved recognition of Paul Ehlirch (1854-1915) who proposed that, if an agent could selectively target a disease causing organism, then a toxin for that organism could be delivered along with the agent of selectivity [1]. Targeted drug delivery involves identifying a specific drug receptor which may be a diseased tissue or lesion and transporting a therapeutic agent of choice to this site. The site specificity aims to improve pharmacological uptake while limiting drug toxicity and other side effects to neighboring cells, tissues and organs.

Previous limitations in drug delivery including inadequate drug reaching the target organs or tissue, side effects on healthy organs and poor treatment monitoring mechanisms have resulted in these current challenges. Nanotechnology has the potential to offer solutions to these obstacles through use of nanomagnetic materials which have unique sizes and larger surface to volume ratios [2-8]. There are various drug targeting systems currently in use and can be broadly classified either as physical, chemical or biological processes. These processes are summarized in Table 1.

Research on versatile therapeutic devices that can control the spatial and temporal release of therapeutic agents using external forces has been ongoing and expanded to include different techniques like magnetic fields, ultrasound, electric fields, temperature, light, and mechanical forces [2-3]. By applying externally generated forces, the drug carrying MNC sphere is first localized at the target site, and then activated to release of the drug where it is needed [5].

TABLE 1

ROUTES OF DRUG DELIVERY

• **Intraperitoneal drug delivery**
• **Intrathecal**
• **Nasal**
• **Oral** • **Rectal infusion**
• **Pulmonary inhalation**
• **Intramuscular injection** • **Subcutaneous injection**
• **Transdermal route** • **Intradermal route**
• **Vascular route**

Adapted from [4]

In a magnetic targeted system, MNC spheres carrying drug molecules are used to target specific sites of the body through application of external magnetic forces on those particles. Over time, the drug molecules will be steadily released from the carrier matrix. Thus, the targeted delivery of the drug to target cells or tissues can improve the therapeutic efficiency of the drugs by lowering the collateral toxic side effects on the healthy cells or tissues [6-11].

A magnetic targeted system generating a magnetic field of about 100 Oe and 2500 Oe is promising and serves as a basis of a drug localization system for targeted treatment [13]. This system is found to be effective, safe, less costly, and practical, when compared to other therapeutic devices [11, 12]. A controlled drug delivery system is composed of a therapeutic drug and MNP which are embedded in a biodegradable polymer forming a MNC sphere as shown in Figure 1.1. The drug carrying MNC spheres are then intravenously directed to the target site where the drug molecules are held and steadily released from the carrier to the tissue.

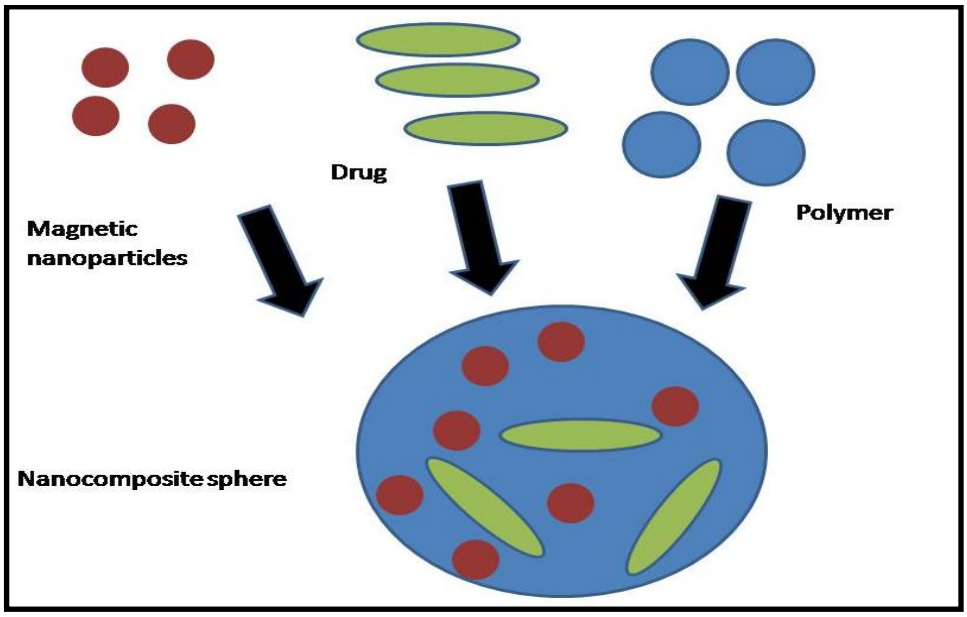

Figure 1.1 Composition of MNC sphere used in drug delivery.

The three main mechanisms of releasing drug molecules from the polymeric magnetic spheres into a blood vessel or tissue include degradation and or swelling followed by diffusion [13]. Diffusion occurs when drug molecules dissolve in bodily fluids around or within the particles and migrate away from the particles. Degradation takes place when the polymer chains hydrolyze into lower molecular weight species, effectively releasing drug molecules that were trapped by the polymer chains. Swelling-controlled release systems are initially dry. When they are placed in the body, they swell to increase inside pressure and porosity, enabling the drug molecules to diffuse from the swollen network. The release of active drug molecules can also be varied over a certain period based on external and internal parameters [11-13].

A polymer, Poly (dl-lactide-co-glycolide) (PLGA), approved by the Food and Drug Administration (FDA) for drug delivery [14-17], is used as a host matrix because of its biodegradability and biocompatibility. In this research, PLGA was embedded with MNP and a drug via the oil-in-oil emulsion/solvent evaporation technique [18, 19]. MNP concentrations in PLGA were varied in the range of 0% to 25%. After the fabrication step, biodegradable MNC spheres were characterized to determine their size distribution, morphology and magnetic properties using various methods like X-ray diffraction (XRD), scanning electron microscopy (SEM), transmission electron microscopy (TEM), Mössbauer spectroscopy (MS) and a superconducting quantum interference device (SQUID).

Fluid flow studies were carried out to study the blood flow profile and magnetic capture mechanisms in vessels with different cross-sections and varying flow rates. A cytotoxicity evaluation of cobalt zinc ferrite and magnetite was also carried out using cultured raw cells to determine their effectiveness for use in drug delivery.

1.2 Objective of the Study

The aim of this research was to study the preparation, fabrication, characterization of MNP and MNC spheres used in drug delivery. Further studies aimed to study way of improving the efficiency of these magnetic materials for use in advanced drug delivery. This was done by exploring experimental fluid flow mechanisms under high magnetic fields to determine optimum conditions necessary for successful targeted drug delivery. This study also focused on cytotoxicity effects of these magnetic materials and how to improve their efficiency for use in magnetic targeted drug delivery.

Magnetite nanoparticles have been used to fabricate MNC spheres, and extending this technique to cobalt zinc ferrites was proposed. The appropriate polymer that is biodegradable was selected for this study. The main goal was to study how the process fabrication, encapsulation and fluid flow affected the overall magnetic properties of the nanoparticles.

The specific goals were:

- To optimize the preparation and encapsulation efficiency of oil- in- oil emulsion/solvent evaporation method
- To determine significant magnetic properties of nanoparticles and how they are affected by the encapsulation mechanism
- To implement an experimental fluid flow scheme that would be a basis for understanding the effect of the magnetic capture on flowing nanoparticles
- To compare the cytotoxicity effects of cobalt zinc ferrites and magnetite on normal raw cells and the possibility of their use as alternative drug delivery agents.

Note that even though the mechanisms of targeted drug delivery have been researched in the past, there is currently very little success in the use of magnetic drug targeting beyond the laboratory setting hence a biologically active polymeric nanoparticle formulation with proven function remains to be developed [29].

1.3 Outline

In this dissertation, the second **chapter** provides a more detailed literature review on MNP, MNC, their fabrication and characterization. This chapter covers the theoretical background in detail on magnetic materials, biodegradable polymers, fluid flow mechanisms, modeling and cell cytotoxicity studies carried out in this research and what has been done by other researchers in this field. **Chapter 3** looks at the experimental mechanisms used in the preparation of MNP. This section also covers the methods used in characterizing MNP and the results obtained.

Chapter 4 covers the preparation and characterization techniques ofthe MNC spheres and how the drug is encapsulated in the polymer. Characterization methods and results obtained include DLLS, SEM, TEM and SQUID. The experimental fluid flow profile of the delivery system will be covered in **Chapter 5.** This chapter will cover the hydrodynamic characteristics of the magnetic materials flowing in a vessel in the presence of a magnetic field.

Chapter 6 gives detailed description of cytotoxicity experiments carried out to study the toxicity effects of the MNP and MNC spheres on normal phagocytes. **Chapter 7** provides the conclusion and recommendations and a discussion of future research in the area of drug delivery.

CHAPTER 2

LITERATURE REVIEW

2.1 Introduction

There has been a steady growth in research aimed at determining the appropriate carriers of therapeutic agents in treatment of diseases by targeted drug delivery. The use of MNP as carrier material for therapeutic agents has grown steadily in the last few decades [27, 32]. Interest in these particles is due to the unique properties they posses compared to their bulk counterparts [27- 35]. Extensive research work has been carried out by various groups to determine the properties and characteristics of nanoparticles and how they can be modified for different applications [27- 29].

In targeted delivery, the choice of the appropriate carrier depends on the efficiency of drug loading, their toxicity and the ease with which the drug can be encapsulated or embedded in them. In magnetic targeted drug delivery, MNP may be synthesized and their surface modified to serve as carrier agents. Surface modification involves processes like coatings or embedding the MNP in a biodegradable material that would transport the drug.

MNPs may be synthesized by either top –down or bottoms-up approaches and embedded in a suitable biodegradable polymer to form drug carrying MNC spheres. These MNP also find applications in magnetic resonance imaging (MRI) contrast agents and magnetic hypothermia therapy [28-30]. Once prepared, MNC spheres are then injected intravenously and guided towards the target site by use of an external magnetic field or may be surgically implanted and held in place by a magnetic field around the target region.

In this section, properties of magnetic materials commonly used in targeted drug delivery and common methods of fabricating and encapsulating both the drug and MNP in a polymer are discussed. Further literature review is carried out on biodegradable polymers that are commonly used in drug delivery with special emphasis on PLGA. The literature review of fluid flow will be covered in this section. Finally, the last section will look at the cytotoxicity effects of magnetic materials on normal cell proliferation.

2.2 Magnetic Materials

2.2.1 Classification

Nanomaterials have unique physicochemical properties that make them suitable for modification and use in a wide range of chemical, biological and engineering applications. In bioengineering, these materials find applications in areas like targeted drug delivery, magnetic hypothermia, implants, MRI and stents [36]. Most materials can be divided into 5 major classes based on their magnetic properties [37]. These includediamagnetic materials, paramagnetic materials, ferromagnetic materials, anti-ferromagnetic and ferrimagnetic materials.

Diamagnetism occurs in all substances due to the interaction of the magnetic field with the electrons of an atom. Diamagnetic materials have atoms with no net magnetic moment. It is observed that the magnetic moment induced in diamagnetic materials is extremely weak and in the opposite direction to the applied magnetic field; hence, these materials have negative magnetic susceptibility). The magnetic susceptibility of such materials is found to be independent of temperature effects [37] and can be determined from the slope. A magnetization curve of diamagnetic materials is as illustrated in Figure 2.1(a).

Paramagnetism occurs where the coupling between moments of different atoms is small or zero such that in the absence of an applied field H such substance exhibits zero magnetic moment. These materials have their magnetic dipole moments partially aligned. When a magnetic field is applied, the material gains a net positive magnetization and positive magnetic susceptibility as shown in Figure 2.1(b). Paramagnetic materials exhibit a magnetic susceptibility that depends on temperature unlike diamagnetic materials [37].

A variation in temperature affects the ability of magnetic moments to align as explained by the Curie law. At Curie temperature (T_c), the thermal energy overcomes the strong exchange interaction forces causing an arbitrary alignment of the magnetic moments leading to zero saturation magnetization [37].

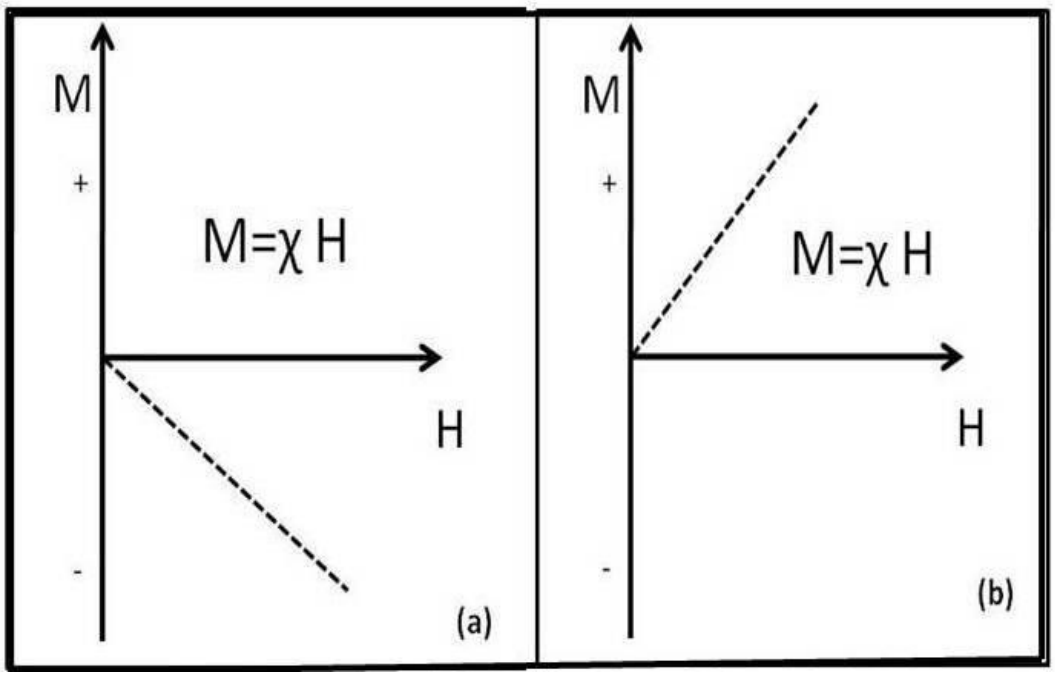

Figure 2.1 Typical magnetization curves of (a) diamagnetic materials and (b) paramagnetic materials [37].

Ferromagnetism occurs in materials where the coupling between the atomic moments is very large due to strong electron exchange forces and the atomic moments are aligned parallel in groups or pairs [37]. If the atomic pairs are aligned anti-parallel, then they form a class of anti-ferromagnetic materials. Ferromagnets have a large net magnetization even when the external magnetic field is removed. Distinctive characteristics of ferromagnetic materials are illustrated in Figure 2.2. It is an example of magnetic hysteresis obtained in ferromagnetism. Ferromagnetic materials can be identified from ferromagnetic materials by magnetic measurements if the measurements are taken over a sequence of temperatures.

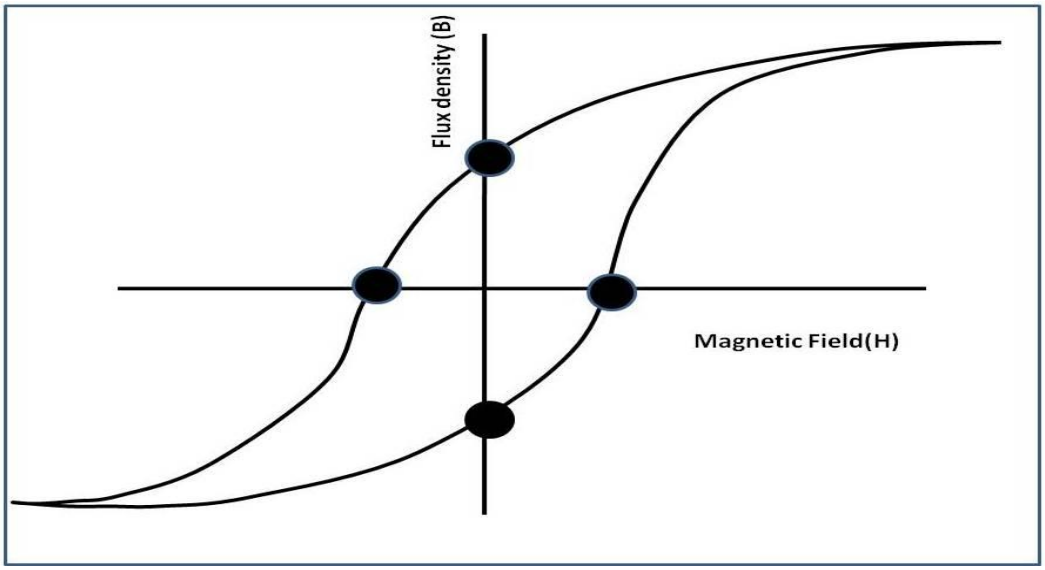

Figure 2.2 Magnetic hysteresis in ferromagnetic materials [92].

Ferrimagnetic materials have more intricate magnetic ordering due to their crystal structure. Such materials exhibit spontaneous magnetization below a certain temperature due to nonparallel arrangement of the strongly coupled atomic dipoles [38]. Ferrimagnetic materials consist of self

saturated domains and undergo magnetic saturation, remanence and hysteresis just like ferromagnetic materials.

Ferrimagnetic materials useful in targeted drug delivery include materials existing as spinels with a general chemical formula AB_2X_4 where X is non-magnetic divalent atom like oxygen. A is divalent ion of metals such as Ni, Co, Zn, Mn or Mg while B is a trivalent ion of metals such as Mn, Co, Fe or Al [39]. Depending on the position of metals in the tetrahedral and octahedral sites, spinel ferrites can either be normal ($A^{2+}[Fe_2^{3+}]O^{2-}_4$), inverse ($Fe^{3+}[A^{2+}Fe_2^{3+}]O^{2-}_4$), or a mixture of two divalent metal ions of varying ratios ($A_x B_{1-x} Fe_2^{3+}O^{2-}_4$) with X ranging from 0 up to 1 [40].

2.2.2 Superparamagnetism

Superparamagnetism is a property of magnetic nanoparticles with sizes around 10 nm. At this size, each magnetic dipole is considered a single domain. Below Curie temperature, the magnetic moments of each particle interact with neighboring particles due to high thermal energy. This energy overcomes the coupling forces causing the particle to flip the orientation. The material loses its internal magnetic order and its magnetic field becomes zero. When an external field is applied, the material exhibits paramagnetic characteristics. In paramagnetic materials, individual atoms are being influenced by the external field while in superparamagnetism the entire crystallite aligns itself with the magnetic field well below the Curie temperature [37-40].

Magnetite and maghemite nanoparticles are examples of ferrites that have gained significance in targeted drug delivery, magnetic imaging and magnetic hypothermia studies. These nanoparticles containing single domains are known to have superparamagnetic properties,

high saturation magnetic moments, zero remanance and highest ordering temperatures [36] among the spinels as depicted in Figure 2.3.

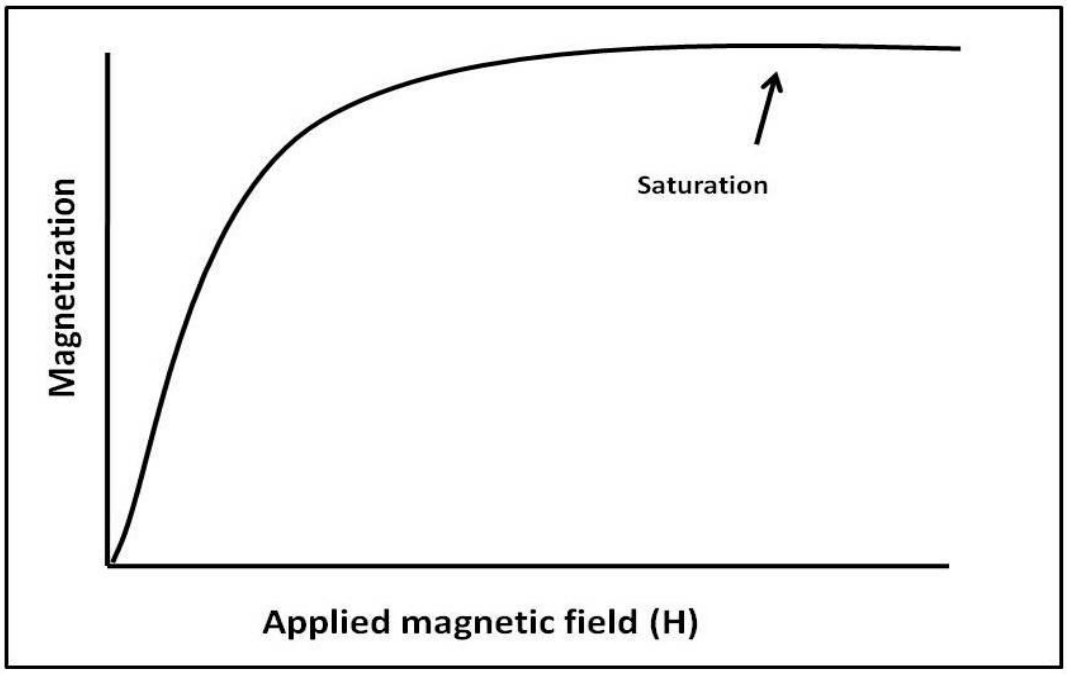

Figure 2.3 Magnetization curves showing superparamagnetism with a saturation magnetization and exhibiting zero remanence and coercivity as depicted by zero intercept [37].

Magnetite (Fe_3O_4) shown in Figure 2.4 can either have a cubic or hexagonal structure with the metal ions in a ferrite crystal occupying two distinct crystallographic positions called A site (tetrahedral) and B site (octahedral). Factors that may give rise to site preference include (a) ion size, (b) electron configuration of the ion, and (c) symmetry and strength of the crystalline field at site [38]. The site occupancy and magnetic exchange interactions between the A and B sites determine the magnetic properties of the ferrites. This is through changes in average anisotropy energy barriers which in turn determine the relaxation times, magnetic hardness and ordering temperature [41].

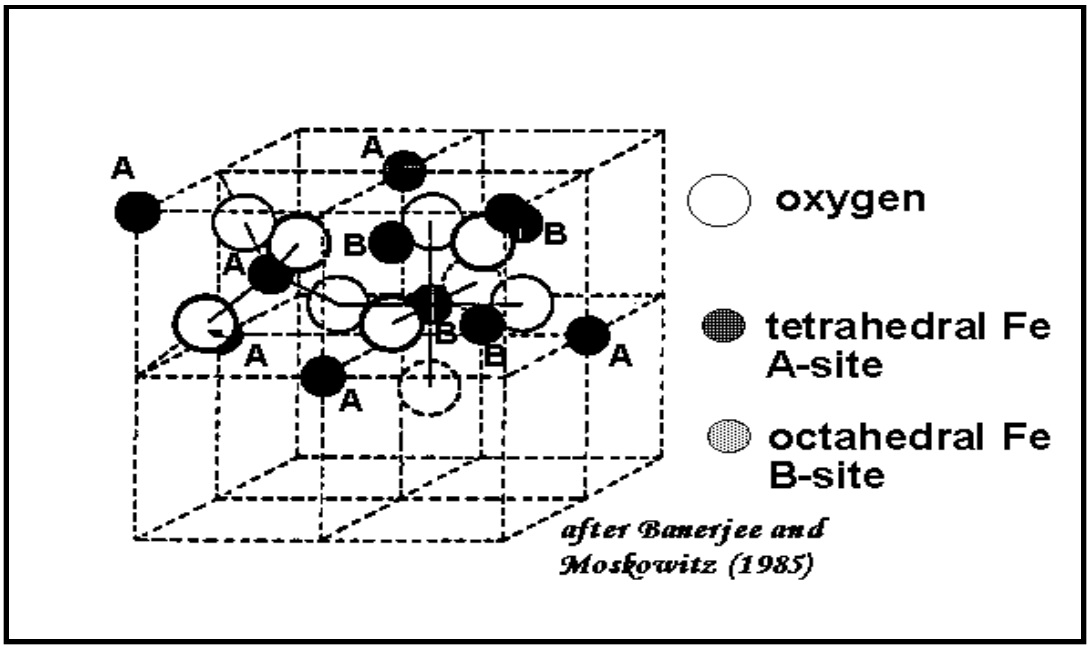

Figure 2.4 Crystal structure of Magnetite showing both the tetrahedral Fe A-site and Octahedral Fe B- site [38].

In this study magnetite and $Co_{0.5}Zn_{0.5}Fe_2O_4$ were selected and their properties evaluated to determine their physical and magnetic properties. When the MNP are embedded in a polymer or coated with another metal shell, the polymer or shell used acts to modify the magnetic interactions between the individual nanoparticles. The effect of polymer-MNP or shell- MNP interactions on their magnetic properties is yet to be fully understood. Palash et al., have synthesized maghemite (γ-Fe_2O_3) and coated MNP with gold conjugated to human/bovine serum albumin [56]. By comparing the magnetization against field strength for different coating thickness, they observed a reduction in the blocking temperature due to the diamagnetic shielding. The use of starch coated nanoparticles and its magnetic properties ahev been also investigated by Jurgons et al. [62].

Several techniques are commonly used to determine the physical and magnetic properties of the MNP and also MNC spheres. These methods include XRD, SEM, TEM, VSM or SQUID and MS. These methods provide valuable information about both structure and magnetic properties [43] of MNP and will be extensively covered in chapter 4.

2.3 Nanoparticle Fabrication

The desire to develop new MNP has generated lots of interest due to the need to improve on the size, structure and properties of these materials. A wide range of experimental work has been done on MNP because of the difference in their physical and chemical characteristics from bulk solids [44-47]. MNP, like other types of inorganic materials, are developed with the expectation of product uniformity, reliable reproducibility, and property control based on manipulation of processing parameter [73]. There are many techniques available in MNP synthesis. These techniques are broadly divided into either Top- down or Bottoms -up approaches.

Top-down approaches like ball milling; lithography and quenching have been used to produce fine particles with a relatively broad size distribution, varied shape and geometry and added impurities. These approaches are usually difficult to design and control and may be limited to materials with poor thermal conductivity [127]. Bottoms- up approaches involve both kinetic and thermodynamic processes that aim to control the process of super saturation, nucleation and growth of the nanoparticles. This is illustrated in Figure 2.5. The resulting particles are found to have a uniform size distribution, morphology, chemical composition with no agglomeration [127].

The three major routes used in synthesis of magnetic materials are physical vapor deposition, mechanical methods and chemical synthesis. These techniques have been extensively

covered in books and journals [23, 26, 46, 48,73]. In this research, we focus on the use of chemical synthesis technique. Chemical synthesis of nanoparticles has received wide acceptance due to the ability to control the size of the particles by manipulating the process parameters that determine the degree of crystal nucleation and growth. Chemical process also provides room for any surface modifications that may be necessary for their unique applications.

Examples of chemical synthesis techniques include chemical precipitation, so-gel, electro-deposition, hydrothermal, micro-emulsion, and sonolysis, electrochemical and other multisynthesis processes [73]. The use of these techniques in the synthesis has been covered in various books and journals [23, 26]. For example, Duong et al., have synthesized nanocrstalline $Co_{1-x}Zn_xFe_2O_4$ by forced hydrolysis [76]. Parrekh et al. used thermal decomposition to synthesize nanoparticles [79].

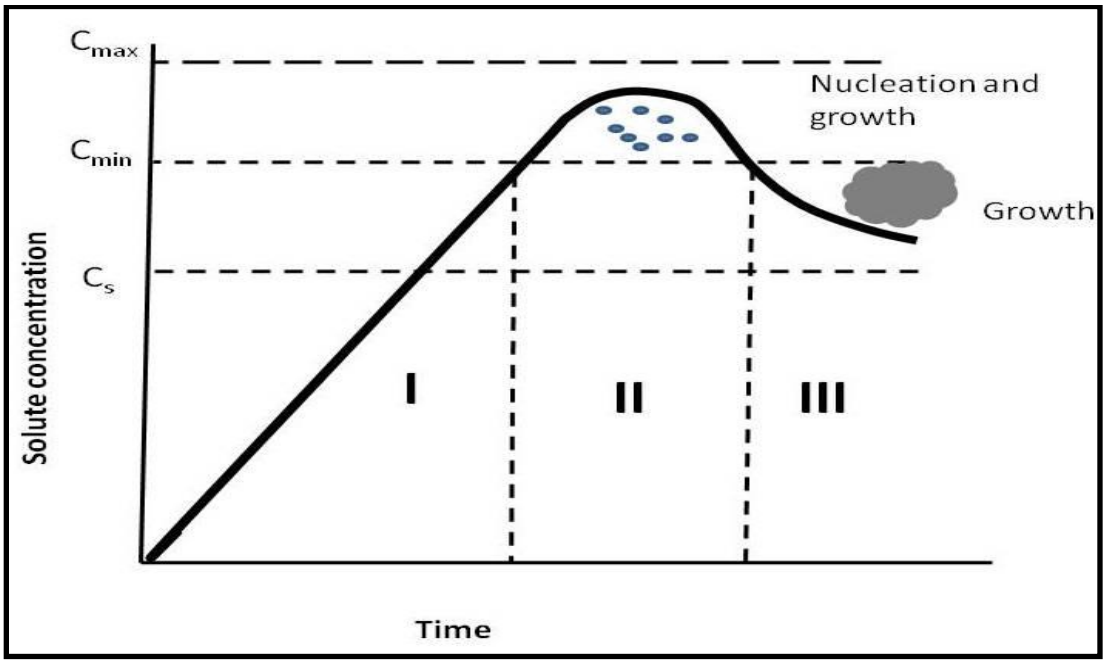

Figure 2.5 Schematic illustrating the process of nucleation and growth [127].

Chemical precipitation has been used for decades as a means to produce nanoparticles from their metal precursors. In this technique, the precursor material is dissolved in a solvent and a precipitant. These two are stirred together while increasing their temperature to promote chemical reaction. The product of this reaction is insoluble solid nanoparticles that are then washed to remove any residues. This method requires strict control of the nucleation temperature, the stirring rate and solution pH value in order to obtain MNP with appropriate size distribution, purity and crystallinity [95]. Hua et al. investigated the effect of varying synthesis temperature and the degree of agitation on the crystallite size of magnetite and found that lower temperatures and higher degree of agitation were necessary for producing smaller particles [97].

Previous attempts to use magnetic particles in these drug delivery applications have relied on high gradient magnetic fields produced by an external magnet and insufficient local forces on magnetite nanoparticles [56]. This can be improved in many ways including selecting nanoparticles with better magnetic properties. The focus of this research is on magnetite and mixed ferrites of cobalt and zinc ($Co_{0.5}Zn_{0.5}Fe_2O_4$) at the concentrations identified as X=0.5. The readjustment of cations in the lattice produces an initial constant increase of magnetization with increasing zinc content up to X=0.5, and then levels off before decreasing to zero at X=1 [77].

Recent research shows that these material posses maximum magnetization at these concentration [44]. While previous experimental studies have been done on the fabrication and characterization of these ferrites in various concentrations at nanoscale and in bulk [44-50], comprehensive and comperative work has not been done on the magnetic suitability of magnetite and cobalt - zinc ferrite for targeted drug delivery.

In this research, we have synthesized $Co_{0.5}Zn_{0.5}Fe_2O_4$, a mixed spinel ferrite with x=5. The cation distribution in cobalt-zinc ferrite nanoparticles can be represented by $Zn^{2+}_{x}Fe^{3+}_{1-x}$ $[Co^{2+}_{1-x}Fe^{3+}_{1+x}]O_4$ where the exchange of Zn^{2+} for Fe^{3+} leads to a decrease in the Curie temperature of the ferrite [34]. When the ratio of zinc content in cobalt-zinc ferrites is increased, a saturation magnetization of the ferrite nanoparticles decreases due to the reduced sub-lattice interactions [34].

2.4 Biodegradable Polymers

Biodegradable polymer carriers are an important part of all MNP- drug carriers for biomedical applications. Such polymers are useful in drug delivery because most of the MNP and drugs are often toxic to the body. The MNP are also able to corrode releasing harmful toxins. Polymeric coatings prevent nanoparticle agglomeration and avoid opsonization while providing a means to tailor the surface properties of MNPs such as surface charge and chemical functionality [74]. Biodegradation is a characteristic of a polymer to break down into byproducts that are easily recognized and cleared by the body without any toxic side effects.

Various types of carriers for MNP and therapeutic agents have been developed by researchers. These include nanocomposite spheres, liposomes, erythrocytes and microspheres. These carriers are developed with the aim of maximizing the encapsulation efficiency, controlling the drug release rate and protecting the body from harmful toxic effects of both the drug and MNP. PLGA, a synthetic polymeric carrier has been selected for our research due to its biodegradability. This polymer is also bioresorbable and approved for safe use in humans by FDA [96]. Other polymers that are commonly used include chitosan, dextran and co-polymers of lactic and glycolic acids.

A polymer is a large molecule composed of many smaller units called monomers that are bonded together [80]. Polymers exist both as synthetic and natural polymers. Synthetic polymers are commonly preferred for drug delivery due to their purity and ease of reproduction as compared to natural polymers. Different types of synthetic biodegradable polymers exist in the market today. The most common ones include polyanhydrides, poly (orthoesters), and polyesters.

Polyanhydrides are usually synthesized by dehydration of diacid or mixture of diacids by either melt condensation or solution polymerization from their constituent monomers and are connected together by anhydride bonds [81,142]. They are found to degrade to biocompatible monomers that are easily metabolized and cleared by the body. Studies on aliphatic polyanhydrides have shown that increasing the alkyl chain length (from n=4 to n=12) of the dicarboxylic acid monomers increases polymer hydrophobicity resulting in a decrease in both polymer degradation and drug release rates [81].

Polyorthoesters are found to be very stable in the absence of moisture and are highly biocompatible. This type of polymer is divided into three main groups; poly orthoesters I, II, and III. These polymers are synthetically prepared and easily hydrolyzed when exposed to an aqueous media. Polyorthoesters have been found quite useful and are being developed for use in surgery, contraception, protein release, post-operative pain treatment and post-operative cancer treatment [81].

Polyesters are a group of synthetic polymers that were first used in the development of suture materials for surgery. Drug delivery devices have also been developed through synthesis

of polymers and copolymers (PLGA) from lactic acid (PLA), glycolic acid (PGA), and ε-caprolactone.

2.4.1 Poly (DL-lactide –Co-Glycolide)

PLGA is the most widely used and well characterized polymers for biodegradable microspheres [51]. These copolymers are approved by FDA and have a history of safe use in humans as they degrade through hydrolysis of its ester linkages in the presence of water to yield biocompatible lactic and glycolic acids [52], by product easily removed by the body.

PLGA can be synthesized two major techniques; top down and bottom up techniques. The top- down techniques include solvent displacement, emulsion evaporation, salting out and emulsion diffusion. Bottom –up techniques involve polymerization techniques, or precipitation techniques. PLGA can be synthesized by means of random ring opening polymerization of two different monomers. By varying the ratio of lactide to glycolide used in the synthesis, different molecular weights of PLGA can be derived [58]. Figure 2.6 shows the structure of PLGA.

PLGA microspheres with diameter ranging from 1 to 250μm can be modified by changing the homopolymer ratio, molar mass and polymer crystallinity hence influencing their degradability and permeability [53, 81]. Biodegradable polymers were first developed and used in making suture materials for surgery. These materials were found to degrade in the body forming biologically inert and compatible by products that could be cleared by the body hence removing the need for follow-up procedures to remove the sutures. The choice of appropriate

polymer for use depends on whether it has been approved by FDA for safe use, its morphology, and structure or drug-polymer interactions.

The mode of drug delivery using a polymer may be in the form of a matrix where the drug is dispersed uniformly in the polymer or in the form of a reservoir where the drug is saturated in a reservoir inside the polymer [139]. The term 'biodegradation' is limited to the description of chemical processes (chemical changes that alter either the molecular weight or solubility of the polymer) while 'bioerosion' may be restricted to refer to physical processes that result in weight loss of a polymer device as illustrated in Figure 2.7 [81].

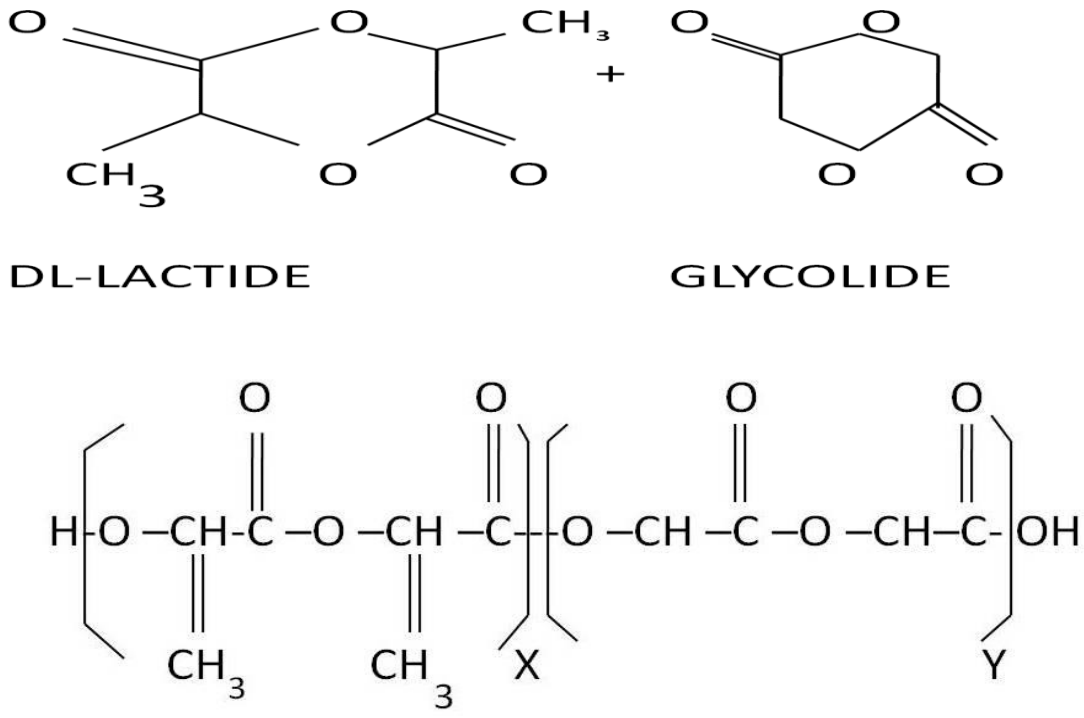

Figure 2.6 Co-polymers Dl-lactide and glycolide used in the synthesis of poly (DL-Lactide-Co-Glycolide) polymer [124].

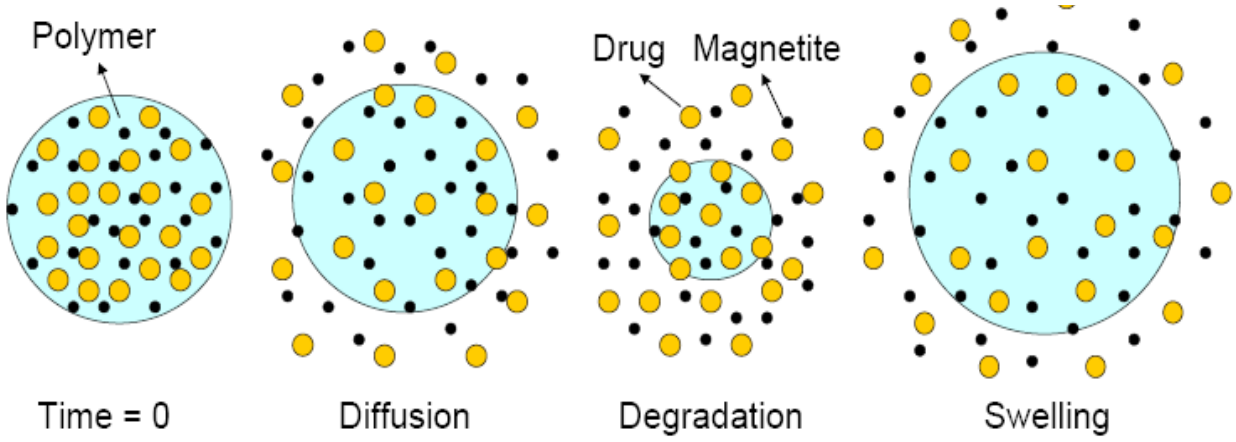

Figure 2.7 Schematic illustration swelling and release mechanisms of MNC spheres [19].

Polymer degradation can either be a chemical processes or a physical process. Chemical degradation processes usually act to transform the molecular weight and the solubility of the polymer matrix. These processes involve the hydrolysis, ionization, protonization or cleavage of the covalent bonds [125]. As the polymer matrix breaks down, the therapeutic agent is slowly released from the matrix. Physical degradation involves both heterogeneous attrition where the polymer preserves its physical integrity as it erodes and homogenous erosion of the shell of the polymer experiencing loss of matrix integrity [125].

It has been reported [19] that the weight average molecular weight (*Mw*) and number average molecular weight (*Mn*) of the polymer and polymeric implants can be determined using gel permeation chromatography. Then, an *in vivo* degradation process of PLGA can be expressed by the degradation index (*DI*) [82-84] as

$$DI = \frac{Mn^{o}}{Mn^{t}} - 1 \tag{2.1}$$

where Mn^{o} is the initial *Mn* value, while Mn^{t} is a given time value.

PLGA usually degrades in the body through the reduction of molecular weight followed by weight loss of the matrix [19]. When the polymer degradation process changes the internal structure of the polymer, the drug permeability increases based on the time and conditions of the media [82]. In this case, the release rate (*dX/dt*) is usually associated with the remaining peptide in the polymeric matrix (*X*) and the body condition. Thus, the degradation of the polymer causes the main changes in the structure of the PLGA matrix [19]. The following empirical equation may be employed for the release rate:

$$-\frac{dX}{dt} = kX \tag{2.2}$$

where k is a parameter related to the polymer molecular weight, which is given as

$$k = b_o + \frac{b_1}{M_W} \tag{2.3}$$

where b_o is the initial relative release rate and b_1 is the dependency of polymer permeability on *Mw* that provides information regarding the contribution of polymer degradation to the release rate. By combining equation 2.3 into equation 2.2, the following equation is achieved [83]:

$$\frac{dX}{dt} = -\left(b_o + b_1\left(\frac{1}{Mw}\right)\right)X \tag{2.4}$$

or by rearranging that

$$\frac{dLnX}{dt} = b_o + b_1 \frac{1}{Mw} \tag{2.5}$$

Equation 2.5 indicates eight possible cases of relative release-rate evolution as a function of inverse molecular weight, depending on whether b_0 and b_1 values are positive or negative, or are equal or not to zero [85].

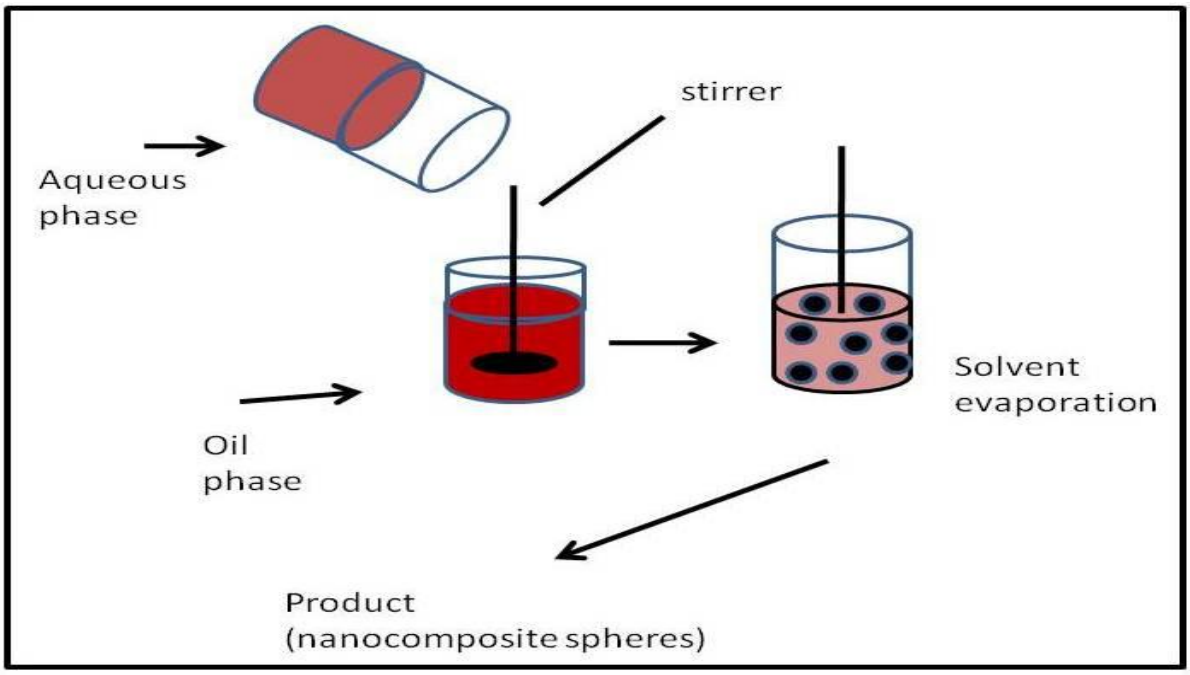

Figure 2.8 Schematic illustration of Single Emulsion- Solvent Evaporation Method [19].

PLGA microspheres can be synthesized by simple emulsification (O/W) as shown in Figure 2.8 or multiple emulsions like (W/O/W) with solvent evaporation [53, 54, 58, 59]. The technique of emulsion solvent evaporation is preferable to other techniques like spray drying, sonication and homogenization as it requires mild conditions that do not compromise the

integrity of the drug [54, 81]. During this process the drug and MNP are embedded in the polymer.

2.5 Hydrodynamic Behavior of Magnetic Nanocomposite Spheres

The current research on the hydrodynamic behavior of MNC developed from an experimental study by Asmatulu et al., on targeting MNC spheres by external magnetic fields [29]. The existing theory on fluid flow and particle capture under magnetic fields assumes that the MNC spheres are very small and are suspended in the fluid. These spheres are assumed to have no effect on the fluid flow behavior as the gravitational effects, inertia and Brownian motion effects on them are negligible [150].

The process of magnetic targeting involves preparation of the magnetic materials, intravenous administration and guided manipulation of these particles to the target site. As the particles move along the vessel, they are acted upon by the hydrodynamic forces due to the fluid flow and the applied magnetic field. In regions where the magnetic force is absent, the hydrodynamics forces are dominant and the particles will be carried along with the fluid. When a magnetic field is applied, the magnetic force-hydrodynamic force interaction will dictate the movement and trajectory of these particles inside the vessels. A higher magnetic field along the vessel than hydrodynamic field leads to magnetic capture.

The particles contained in the fluid will be acted upon by hydrodynamic forces or drag forces as they pass the target region given by Stokes law in equation expressed as:

$$F_D = 6\pi\eta v r \tag{2.6}$$

F_D represents the drag force, η is the viscosity, v is the relative velocity while r is the radius [71]. In order to overcome the drag force and maximize the capture of the particles, a magnetic field larger than these forces is applied perpendicular to the fluid flow as shown in Figure 2.9.

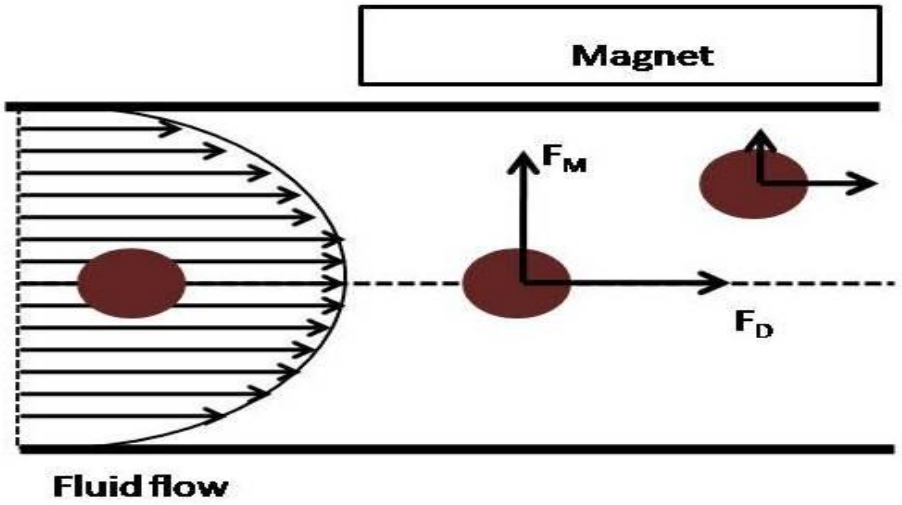

Figure 2.9 schematic of fluid flow and particle capture.

This magnetic force (F_m) is given by equation (2.7)

$$\overrightarrow{F_m} = (\mu_0 \pi M_p \nabla H d^3)/6 \tag{2.7}$$

μ_0 is the permeability of free space is, M_p is the total magnetic moment of the MNP, d is the size of the particles, ∇ is the gradient while H represents the magnetic field.

Asmatulu et al., have studied how the variation of magnetic distance and flow speed affects the percentage of particles captured by the system [29]. They investigated the guiding of MNP by changing the fluid speeds, magnetic distance, magnetic saturation and solid contents. Their results showed that positioning the magnetic field would improve the efficiency of the targeting system. Darton et al., have studied the inflow capture of superparamagnetic

nanoparticles [151]. Using 330 nm and 580 nm magnetite particles, Darton and co workers applied a magnetic field of 0.5 T using a neodymium iron boron magnet on a micro capillary flow. From their data, they found that smaller particles form a layer that is impervious to erosion by fluid shear.

Darton and co workers have also investigated the magnetic field requirement for capture of superparamagnetic nanoparticles flowing in a micro capillary array under constant pressure [152]. Several other in-vitro studies have been carried out by other groups with the aim of improving the magnetic capture. Liu et al., [153], Sheng et al., [154] and Kikura et al., [155] investigated blood embolization and cluster formation in magnetic fluids. This research aims to further improve the process of magnetic capture by studying the effect of changing the magnetic field, vessel diameter, magnetic particle content on the percentage of MNC spheres captured.

2.6 Cytotoxicity Evaluation of Drug Targeting Materials

The overall purpose of targeted drug delivery is to get the drug to the site where it is needed in the body with minimal side effect to other normal body organs. Common drug delivery mechanism like oral uptake or chemotherapy has been known to affect other body organs. This is because of the difference in dosage that is needed for therapeutic purpose and the minimum dosage that would be toxic to the body organs. The use of a biodegradable polymer aims to reduce the toxicity of the drug and MNP.

To overcome these side effects, the drug and MNP may be embedded in a biodegradable polymer and delivered to the target sites by use of a magnetic field. Care should be taken to ensure the toxicity of the MNP. This is especially important when slowly or non degradable particles are used for drug delivery which may show persistence and accumulation on the site of

the drug delivery, eventually resulting in chronic inflammation [75]. Cytotoxicity test are standardized mechanisms carried out on these materials and drugs to ensure that they do not have harmful side effects on normal biological systems. As a first step in any clinical trial, cytotoxicity tests helps to determine if the drug or carrier is biocompatible with normal body cells before animal trials are carried out.

5-Fluorouracil (5-FU) is one of the common drugs available in the market used in chemotherapy for treatment of most forms of cancer. 5-FU may be administered orally, through the skin or intravenously. This makes it easily adaptable for targeted drug delivery. With a very short life span, 5-FU lasts a few minutes in the blood stream or tissue; hence the need to find a slow release mechanism that would increase its therapeutic effect [143,144].

5-FU works by binding to an enzyme called thymidilate synthetase thereby inhibiting ribonucleic acid (RNA) processing, and therefore inhibiting cell growth [143, 145]. This drug has side effects that may be severe or mild depending on the quantity or the frequency of administration. Zhu and co workers have previously used chitosan coated MNP as carriers of 5-FU and also studied their cytotoxicity towards K562 cells [143].

Magnetite and cobalt zinc ferrite are MNP that have been used in this research. These ferrites contain iron, cobalt and zinc which are some of the essential elements of biological growth and development. Uptake of these elements, metabolism and clearance by the body system is essential in limited quantities. Excess quantities in the body may not be easily cleared by the liver and leads to complications like liver cirrhosis, heart arrhythmia and poisoning [146].

The cytotoxicity effects of iron based MNP and ferrofluids have been studied by various groups. Zefeng and coworkers have investigated the preparation and acute toxicology of

nanomagnetic ferrofluids. They found that these materials have low toxicity with minimal side effects on the alimentary tract after peritoneal application [147].

The cytotoxicity effects of metal coatings on magnetic nanoparticle have been investigated by Kirchner et al who prepared CdSe and Cdse/Zns nanoparticles [148]. Asharani and co workers investigated the effects of silver (Ag) nanoparticles on human cells and found that even in small doses Ag nanoparticles were toxic due to DNA damage and chromosomal aberrations [149]. Both in vivo and in vivo testing have found varying degrees of toxicity with many of the metals used to functionalize the MNP like gold silver, silica and copper. These materials have not been approved yet by FDA apart from magnetite. Research on suitable materials to supplement magnetite is ongoing.

In this work cobalt zinc ferrite at optimum concentrations was studied to determine its suitability for targeted delivery. The addition of cobalt and zinc are important as they reduce the amount of iron used in the sample. MNP were prepared by co-precipitation and cytotoxicity analysis carried out. We used magnetite nanoparticle to serve as our baseline for a comparison.

The cytotoxicity testing on the polymer PLGA, and the medium was carried out to check for any residual toxicity effects of the MNC sphere preparation technique. PLGA has been approved by FDA for use as it is biodegradable into biodegradable byproducts which can be easily cleared by the body. The possibility of toxicity due to solvents used in emulsion-solvent preparation was also investigated.

CHAPTER 3

METHODOLOGY I: SYNTHESIS AND CHARACTERIZATION OF MAGNETIC NANOPARTICLES FOR DRUG DELIVERY

3.1 Introduction

The field of targeted drug delivery has recently experienced major developments especially in the area of MNP preparation, surface coating and functionalization. Most drug delivery studies have focused on different methods of preparing MNP to maximize the ability of MNP to serve as carriers of therapeutic agents. MNP are known to posses unique magnetic properties and have the ability to function at basic molecular or cellular level where they provide a stage for magnetic drug delivery [94].

MNP commonly used in drug delivery are spinel ferrites like magnetite and maghemite. These materials posses superparamagnetic properties and are known to be biocompatible with a history of safe use in humans [97-100]. Cobalt zinc ferrite is another alternative material that has been selected in this research and its properties tested to determine its ability to serve as a choice material for targeted drug delivery. There are various methods of preparing monodispersed MNP. Magnetic materials have been prepared by wet chemical precipitation methods, chemical vapor deposition and sol-gel methods among others. The overall aim is to select methods that give rise to MNP of a high quality, narrow size distribution, reproducible physical properties and short process times [95].

In this study, magnetite and cobalt zinc ferrite were prepared by chemical co-precipitation method in an aqueous solution of the constituent metal ion salts and NaOH. The

highest magnetization in $Co_{1-X}Zn_XFe_2O_4$ occurs with a composition X=0.5 [34]. This composition was selected and used to prepare the MNP in this study. These particles were then characterized by XRD, SEM and Mössbauer spectroscopy to determine their size, structure and morphology. The MNP prepared were also encapsulated in PLGA to form a drug loaded nanocomposite sphere. The nanocomposite spheres were tested to evaluate their fluid flow characteristics under an applied magnetic field and their nanocomposite when exposed to normal cells.

3.2 Magnetic Nanoparticle Synthesis

3.2.1 Materials and Equipment

Cobalt sulphate($CoSO_4$), zinc sulphate($ZnSO_4$), sodium hydroxide(NaoH), ferric oxide(FeO_3), hydrochloric acid (HCl), ammonium hydroxide (NH_4OH), ferric chloride($FeCl_3$), and ferrous chloride tetra-hydrate ($FeCl_2.4H_2O$) reagents were purchased from Sigma- Aldrich and were used without any purification. Deionized (DI) water was prepared in the lab using a nanopure water system.

3.2.2 Cobalt Zinc ferrite Nanoparticle Synthesis

$Co_{0.5}$ $Zn_{0.5}Fe_2O_4$ was prepared by co-precipitation technique from $CoSO_4$, $ZnSO_4$ and $Fe_2(SO_4)_3$. The sulfates were first weighed to the required stoichometric ratios as obtained from the chemical equation and dissolved into a beaker containing DI water as shown in Figure 3.1. The beaker was then placed on a stirrer at 500 rpm. The mixture is then heated while stirring to a temperature of 80^0c and NaOH solution added dropwise. The particle nucleation process was observed when the intermediate precipitates changed into dark precipitates of $Co_{0.5}Zn_{0.5}Fe_2O_4$.

The pH of the precipitate was then determined and the solution decanted using an external magnet. At a pH of about 12, the resultant precipitate was then washed several times in DI water to remove the by-products of the reaction and lower the pH to a value of around 7.5.

The samples were then filtered and dried in an oven at 120 ^{0}C for six hours. The nanoparticles were then characterized by XRD and then the particle size was determined using the Debye-Scherrer formula. The MNP formed were then used in MNC preparation.

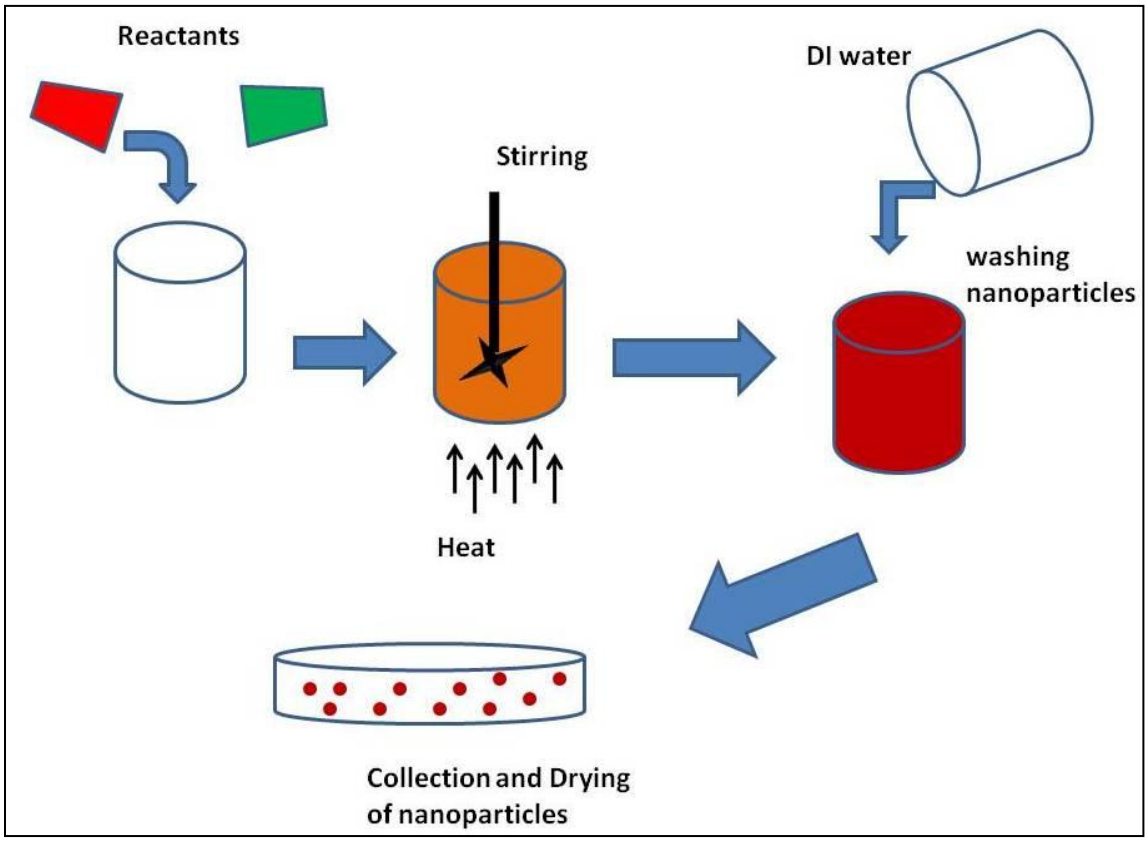

Figure 3.1 Schematics of MNC preparation by co-precipitation method

3.2.3 Magnetite Nanoparticle Synthesis

Magnetite nanoparticles were prepared by chemical precipitation of iron salts in the presence of a strong alkaline solution. The first step involves addition of 50ml of 2M HCl (36.5- 38%) to 55M ammonium hydroxide (NH_4OH) (28- 30%) solution in a 100ml beaker. 2g of ferric chloride($FeCl_3.6H_2O$) was then dissolved in 40ml of 2M HCl and 1.25 g of ferrous chloride($FeCl_2.4H2O$) in 10ml of 2M HCl in separate beakers. The two solutions are then combined and stirred vigorously at 1200 rpm. 55 ml of 5M NH_4OH solution is then added dropwise in 5 minutes at room temperature. The magnetite particles formed are then decanted and collected using a permanent magnet. The particles collected are then washed with DI water to get rid of any residues before being dried for six hours at 120^0C in an oven.

Mossbauer analysis of these samples was done to compare the consistency of our sample preparation technique and the purity of our sample with spectrum of pure samples of magnetite. Further analysis was done using SEM to determine the size distribution of these nanoparticles. Finally, the nanoparticles were analyzed to determine the effects of encapsulation on the magnetic properties of these particles using SQUID.

3.3 Nanoparticle Characterization

3.3.1 X-Ray Diffraction

X-ray is a form of electromagnetic radiation with characteristics similar to that of visible light. X-rays have a wavelength in the range of $0.5 – 2.5A^0$, much shorter than the wavelength of light ($6000A^0$) [101]. X-rays were first discovered by Rontgen, a German physicist in 1895 and quickly found several uses by scientists wishing to study the internal structure of materials. Through methods of radiography and x-ray diffraction, x-rays provides unique methods of

determining the internal structure of crystals with resolutions ranging from 10^{-3}mm to 10^{-7}mm [102]. Today, X-rays can be used to characterize different MNP used in drug delivery.

X-rays are produced when a beam of electrons are made to accelerate by use of a high voltage electric field and collide with a solid target in an x-ray tube. During the collision, X-rays and large amounts of heat are produced. A standard x-ray tube consists of a source of electrons kept at a high negative potential (cathode), a high accelerating voltage in the range of 30,000 to 50,000 volts [101-103], and a metal target kept at a high positive potential (anode). Common metal targets include Mo, Cu and Co. The wavelength of the X-rays produced depends on the characteristics of the metal target used and produces a characteristic spectrum with lines K, L, M, etc. in the order of increasing wavelength [101].

When focused on a solid object, X-ray beam is transmitted and partly absorbed. The process of absorption involves true absorption and scattering [101]. X-ray diffraction has found use in the analysis of the atomic and molecular structure of crystals. A crystal may be defined as a solid composed of atoms, ions or molecules arranged in a pattern periodic in three dimensions or lattice [101]. These crystals act as scattering centers for X-rays because X-rays have wavelength close to inter- atomic spacing in crystals [103]. In order to determine conditions necessary for diffraction to occur, WL Bragg formulated a relation given by equation (3.1) to explain the scattering phenomenon. He found that for diffraction to occur the scattered ray will be in a phase if the path difference is equal to a whole number n of wavelengths [102].

$$n\lambda = 2d_{hkl}\sin\theta \quad (\text{n as integer}) \tag{3.1}$$

The value n in the equation represents the order of diffraction (1, 2, 3 4 ….n), λ is the wavelength, d represents the inter-atomic spacing, while θ is the Bragg diffraction angle. Note

that the number of variables used to calculate the direction of the diffracted beam is reduced in Bragg's law compared to Laue's equations [102].

Two common method used in X-ray diffraction are powder and single crystal methods. In single crystal method shown in Figure 3.2, the single crystal diffractometer is used as an alternative to data collection using a film. This diffractometer is composed of a source of x-rays, a detector, a Goniostat whose function is to orient the crystal so that the chosen X-ray diffracted beam can be received by the detector and a computer. The computer controls the Goniostat and detector movements while performing the mathematical operations required to position the detector and the crystal [105].

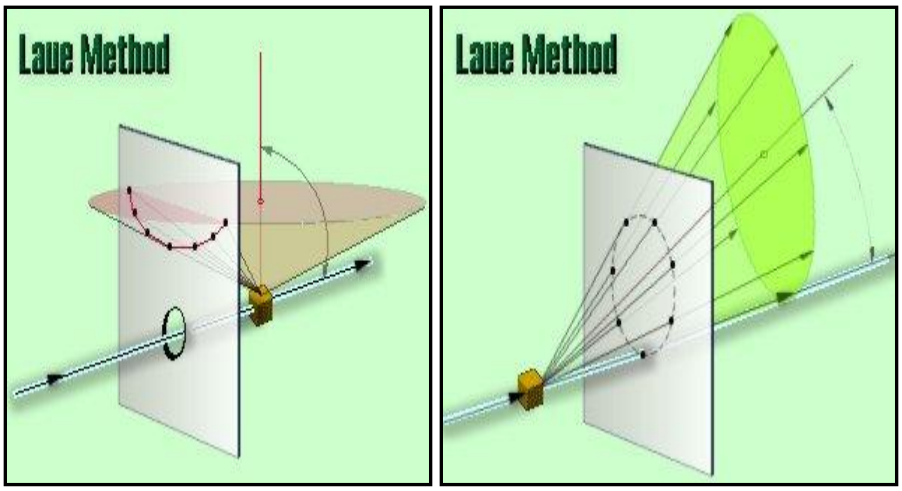

Figure 3.2 schematic showing single crystals (Laue) method (109**)**

In powder diffraction method, the crystals to be examined are composed of very fine particles due to the fabrication mechanism or by grinding. This technique is the best known and widely used analytical tool for both qualitative and quantitative analysis of crystalline materials [105]. The diffraction generated by a polycrystalline powder is usually obtained by placing a

film inside the transmission camera perpendicular to the x-ray beam. Of interest is the Debye-Scherrer camera that uses a geometry which allows the recording of the diffraction pattern of the powder sample at both high and low 2θ values [105].

The set up is composed of an X-ray source, and a detector which moves tracing a circle around the sample specimen. The incident X-ray beam is kept in the vertical position to the increasing values of 2θ. Each crystallite has its own reciprocal lattice producing a series of concentric spherical hkl shells. The diffraction pattern has a series of cones rather than spots [104] as illustrated in Figure 3.3. The positions and intensities of the diffracted beam are then recorded to yield a characteristic diffraction pattern.

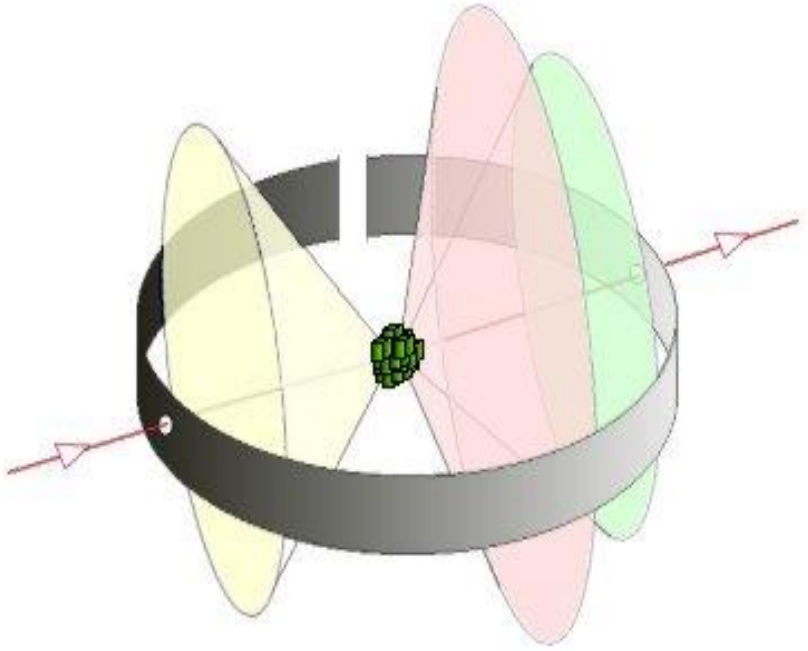

Figure 3.3 Schematic showing the powder diffraction method (109)

Measurement of the crystal grain size (t) is based on the determination of B the line broadening in Scherrer's equation (3.2). B is the full width of the beam at half the maximum peak intensity [102]

$$t = \frac{K\lambda}{B \cos \theta_B} \tag{3.2}$$

where k is a constant dependent on the crystallite shape and close to 0.9, λ is the X-ray wavelength while θ_B is the Bragg angle.

3.3.2 Transmission Electron Microscopy (TEM)

TEM has been a useful tool for characterization and analysis of different specimens in a wide range of areas of physical and biological research. In this technique, a stream of electrons is transmitted through the material sample. In the process, the electrons interact with the sample forming an image which can then be magnified and focused on a detector or photographic film. Due to their high resolution, TEM is found quite useful in magnifying extremely small particles better than other microscopes. From the TEM images formed one can easily determine the chemical structure, crystal orientation, electronic structure and sample induced phase shift [110].

The electron source at the top of Figure 3.4 represents an electron gun that produces a stream of electrons of one wavelength. The wavelength (λ) of an electron can be expressed by the De Broglie's' equation (3.3).

$$\lambda = \frac{h}{mv} \tag{3.3}$$

where h= (6.626 X 10^{-23}) ergs/sec is the Planck's constant, m is the mass of electron, and v is the electron velocity. When operating a TEM machine, the wavelength of the electrons can

be determined by the equation (3.4) which factors the mass, velocity and accelerating voltage (V) of the electrons.

$$\lambda = \frac{1.23}{\sqrt{V}} \tag{3.4}$$

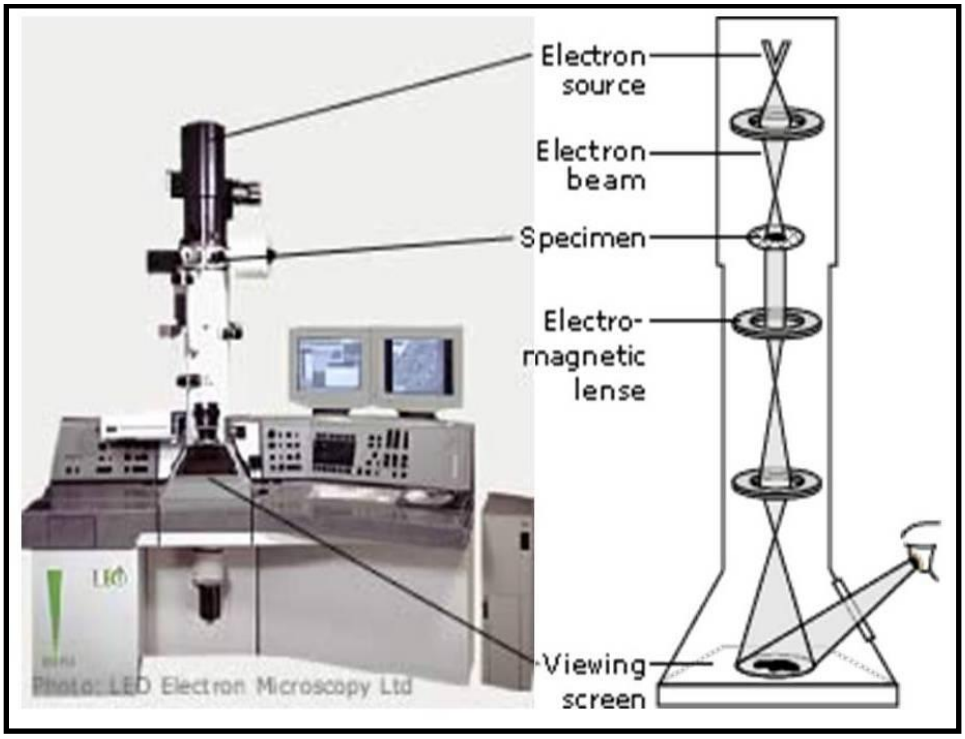

Figure 3.4 Standard TEM machine with the structure on the right [101]

Modern TEM's have very high resolutions with wavelengths in the range of 0.05nm to 1nm. The resolution capabilities of a TEM may be affected by lens defects like spherical aberration and astigmatism. The stream of electrons is made to pass through condenser lenses that act to focus the stream such that a thin or wide spot strikes the sample specimen. This can be done using an intensity brightness control knob. The beam then strikes the specimen. A portion of the stream will be transmitted while the rest is absorbed by the specimen. The part that is

transmitted is the focused by the electromagnetic lenses to form an image. This is done by refracting the electron beam so that it converges at the focal point. The focal length of the electromagnetic lenses can be varied by changing the DC current supplied to the solenoid and is governed by the equation (3.5).

$$\mathbf{f = K(\frac{V}{i^2})} \tag{3.5}$$

where K is a constant related to the geometry of the lens and no of turns, V is the accelerating voltage, and $\boldsymbol{i}$ is the current passing through the coil.

The image obtained is then enlarged by the next lenses to form a larger image on the viewing screen. The darker areas of the image represent those areas of the sample that fewer electrons were transmitted through (they are thicker or denser) while the lighter areas of the image represent those areas of the sample that more electrons were transmitted through (they are thinner or less dense) [100].

For any microscope, the magnification is seen as a ratio of the image to the object distances as in equation (3.5)

$$\text{Magnification} = \frac{\textbf{image distance}}{\textbf{Object distance}} \tag{3.6}$$

The total magnification for a TEM machine is the product of the individual magnifications of the respective lenses used. This is summarized in equation (3.6).

$$M_T = M_o \times M_I \times M_P \tag{3.7}$$

where M_T is the total magnification, M_O is the magnification of the objective lens, M_I is the magnification of the intermediate lens and M_P is the magnification of the projection lens.

The main disadvantage of the TEM lies in the fact that the specimen to be studied has to be thinly sliced such that it allows more electrons to pass through. This process can easily damage the sample if not done carefully. Preparation of the sample also involves placing the sample in a vacuum holder. Since the mass of the electrons are very small, they can be stopped or deflected easily by air molecules[99].

3.3.3 Mossbauer Spectroscopy

Mossbauer Effect was first discovered by a German physicist Rudolf Mossbauer in 1957. Mossbauer Effect, also called gamma resonance spectroscopy has been used as a tool to analyze basic physical, chemical and biological properties of materials. Figure 3.5 is an illustration of the Mössbauer set up. Mossbauer discovered that gamma ray emission and absorption were possible without recoil. In his experiment he expected that gamma-ray photons would induce recoil to the nucleus which emitted them causing the gamma-rays to have lower energy [115- 117].

For the gamma-rays to be absorbed by another nucleus, it needs more energy to compensate for the recoil effect on the absorber. To provide this energy, the gamma ray source is heated to increase the mean velocity and hence the energy of the emitted gamma ray. Since the atoms and molecules (or nuclei) emitting or absorbing the gamma rays are in thermal motion the gamma rays experience a Doppler shift leading to Doppler resonance broadening [116].

Mossbauer placed both the emitter and the absorber in liquid air expecting an increase in the transmitivity of the absorber and an increase in the counting rate of the gamma counter placed behind the absorber [115]. What he observed was actually opposite in that the count rate

decreased implying an increase in the Gamma ray absorption. This is what is referred to as a recoil-free emission and absorption at lower temperature.

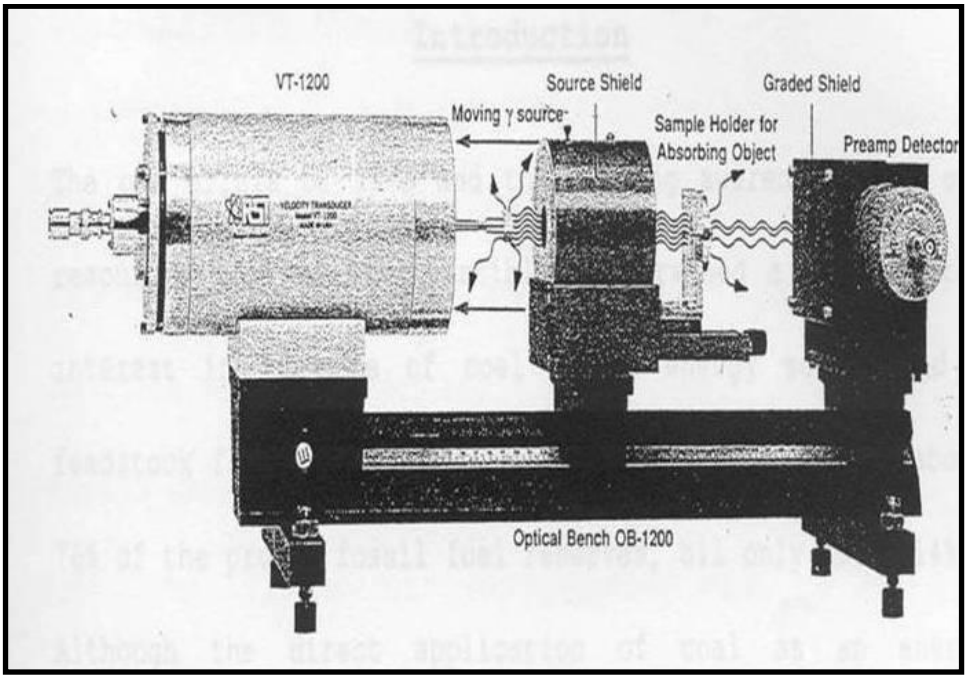

Figure 3.5 Illustration of Mossbauer equipment [117]

When an excited nucleus decays it emits a photon. In the process, the nucleus recoils in order to conserve its momentum. This recoil decreases energy of the photon, and is less than the excitation energy needed for absorption. However, if the emitted or absorbed atom form a part of a crystal lattice (through the cooling process), the emission or absorption process occurs without recoil leading to resonance scattering (Doppler broadening of resonance line ceases) [113,115,116].

When the excited nucleus jumps to the ground state, it emits a gamma ray as shown in Figure 3.6. The energy E of the gamma ray equal to the energy difference between the two states

is reduced by the amount of the recoil energy [115]. This is well explained by the case of a man firing a cannon ball from a boat towards land.

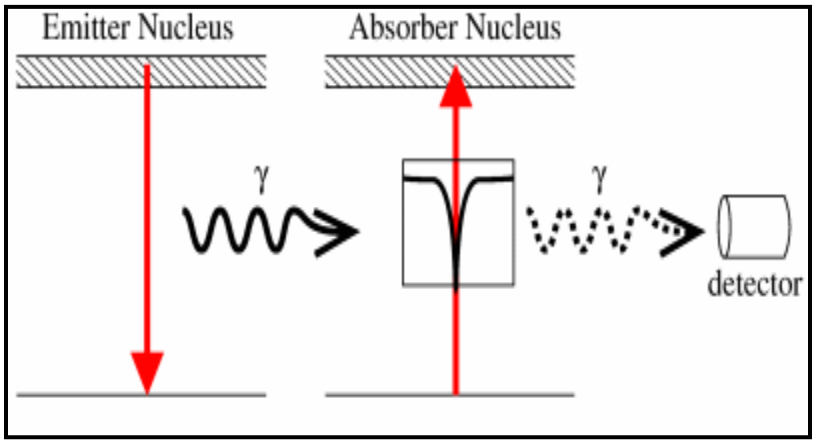

Figure 3.6 simple Mossbauer spectrums from identical source and absorber (113)

The basic set-up of a Mössbauer spectrometer shown in Figure 3.7 is composed of a source (radioactive emitter), an absorber (sample), a velocity transducer and a counter (detector) [117].

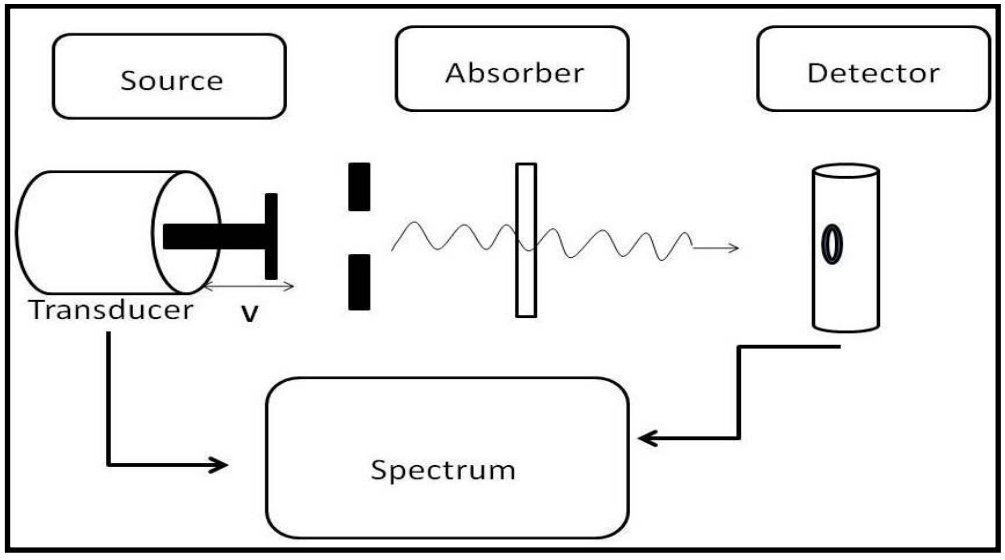

Figure 3.7 Schematic of Mossbauer set-up.

The Mössbauer spectroscopy technique uses a precursor radioactive nuclide contained in a solid matrix. The Mössbauer isotope commonly used is ^{57}Fe as it can be used over a wide range of magnetic materials containing iron [118]. The source used for ^{57}Fe resonance spectroscopy is ^{57}Co with an activity of 30 mCi and a half life of 270 days. This source has an atomic number (z=27). The nucleus captures an electron to decreases the charge to Z= 26 and balance the energy with emission of three gamma-rays with energies; 14.4 KeV, 122 KeV and 136 KeV shown in Figure 3.8 due to the high recoil free fraction(f), only the 14.4 KeV gamma- rays are used.

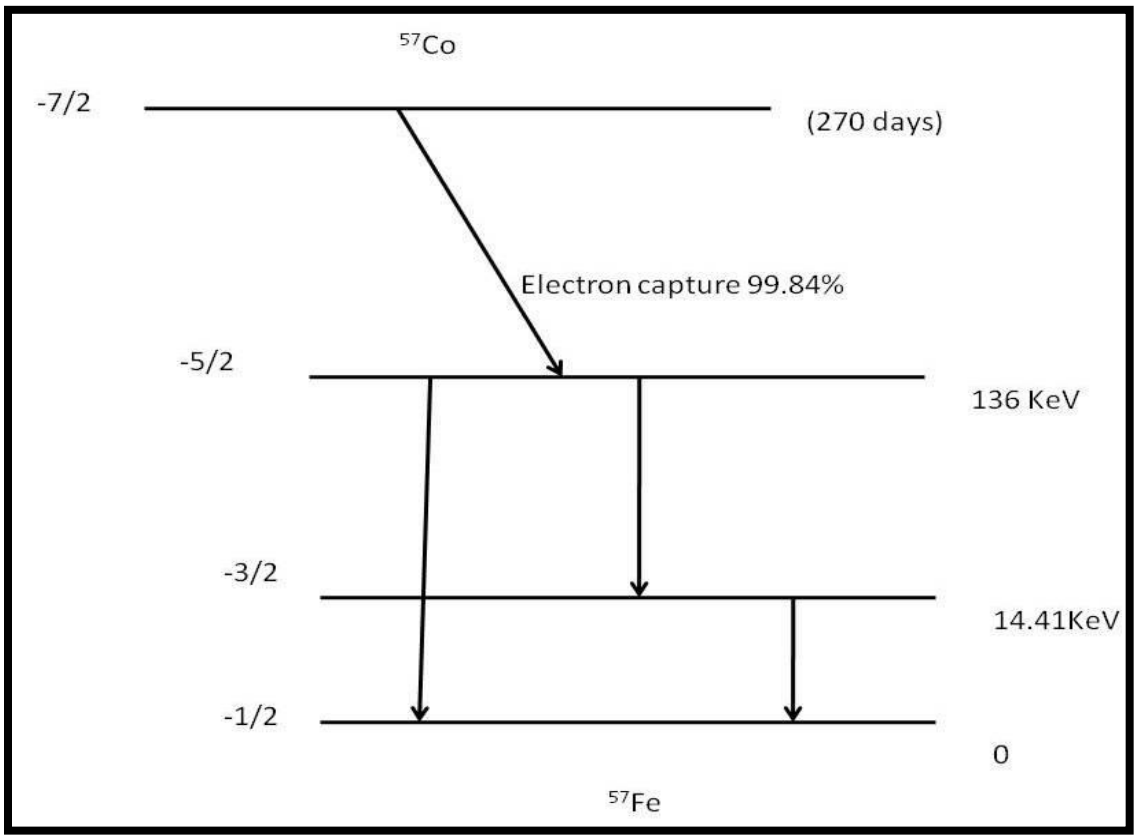

Figure 3.8 Shows the nuclear decay of ^{57}Co to ^{57}Fe.

The samples of magnetite were synthesized by co-precipitation method only and annealed at 120^0c. The samples were prepared by dispersing a thin layer of the magnetic material on to a plastic sample holder. The thickness of the sample was adjusted to ensure the data sampling rate produced optimum signal to noise ratio and allow reasonable time for a data collection. The transducer used was the Doppler modulator, VT1200 run by a triangular input waveform and by a feedback amplification system. The transducer was calibrated using ^{57}Fe in pure Fe [115,116]. While the transducer is capable of inducing a range of velocities, a constant velocity of 11.35 mm/s was used.

A gas-filled proportional counter is used for detecting the gamma rays. The detector is a Xe-CO_2 proportional counter that detects by conversion of electrons. The gamma-ray enters the beryllium window of the detector and knocks off one electron causing an avalanche [117]. The resulting electrons are then accelerated through voltage adjustment to the anode of the detector, and converted to a pulse corresponding to the energy of the initial γ-rays. After the detection, the signal is pre-amplified using a standard charge sensitive preamplifier and passed through a multi-channel analyzer [117] .

3.4 Results

3.4.1 X-Ray Diffraction Measurement Results

The crystallographic structure of the $Co_{0.5}Zn_{0.5}Fe_2O_4$ nanoparticles was obtained by X-ray diffraction at room temperature using Cu kα radiation. The samples were packed into a sample holder and placed on a movable sample platform. With the fixed X-ray source, the sample platform was allowed to rotate with respect to the X-ray beam through a given angle θ. On the opposite side, the X-ray detector swept an arc 2θ with respect to the beam of X-ray and at a speed twice the sample speed. The raw data obtained can be found in Appendix 1

TABLE 2

SUMMARY DATA FROM X-RAY DIFFRACTION PATTERN OBTAINED FROM A SAMPLE OF $Co_{0.5}Zn_{0.5}Fe_3O_4$

hkl	**FWHM (2θ)**	***size*(nm)**
111	0.98	10.02
220	0.97	10.20
311	0.90	9.87
400	1.00	10.44

The X-ray diffraction pattern was found to match with a single phase of cubic spinel cobalt zinc ferrite. The sample showed no evidence of separate phases or process contamination. The diffraction peaks observed appeared wider, suggestive of smaller chrytalline particles. The X-ray diffraction patterns of MNP are shown in Figure 3.9. These patterns display a fundamental peak characteristic of spinels and corresponding to a single phase of Co-Zn- ferrite.

A summary of the data from this diffraction pattern is shown in Table 2 where the crystallite size is determined using the Scherrer's equation.

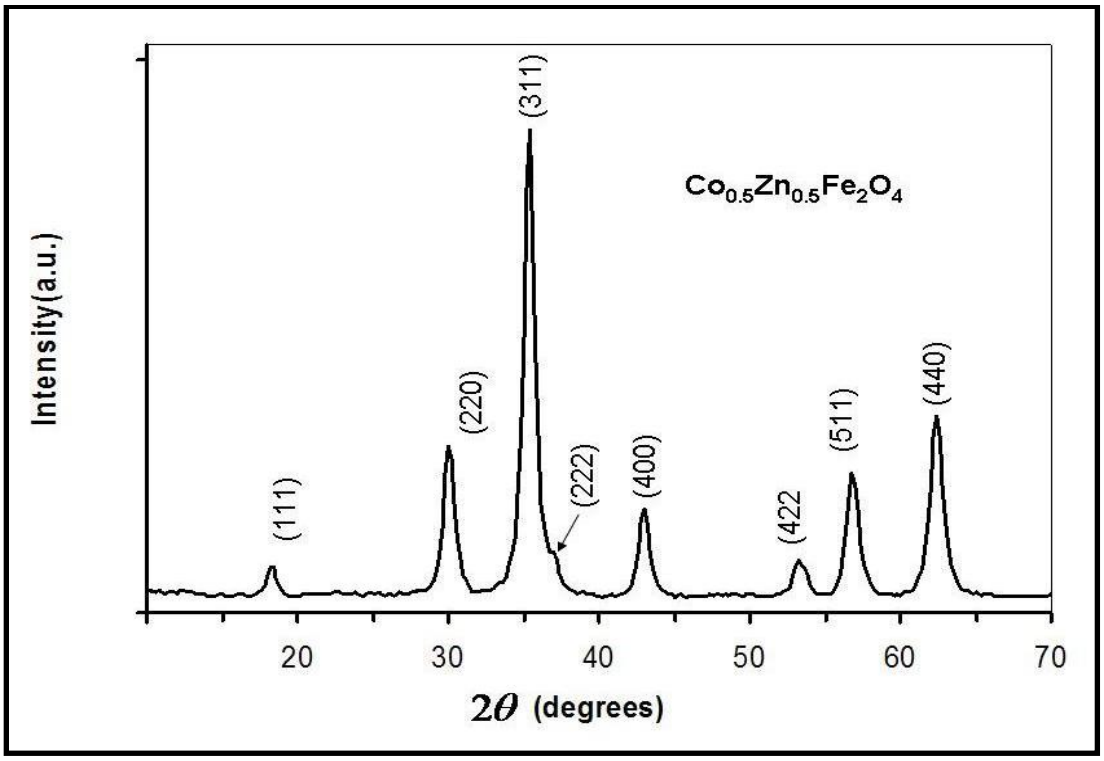

Figure 3.9 X-ray diffraction pattern of $Co_{0.5}Zn_{0.5}Fe_3O_4$ prepared by co-precipitation of sulphates and annealed at 120^0.

3.4.2 TEM Results

The morphology, size and distribution of the MNP and the MNC spheres were investigated using TEM. Figures 3.10 and 3.11 shows images of magnetite nanoparticles and their particle size distribution The magnetite nanoparticles in Figure 3.10 (A) are found to have a mean of 11.03 ±3.5nm and those in Figure 3.10 (B) have a mean of 12.64 ± 4.6 nm with good monodispersity. The particle distribution of the individual TEM images shows a narrow size distribution with fewer outliers. The images in Figure 3.10 were obtained at a lower resolution and show more particles. The images in Figure 3.11 (A) and (B) were obtained at a higher resolution with a mean size of 19.94 ± 7 nm and 12.05 ± 4.1 nm, respectively allowing one to see the crystal lattice of individual grains.

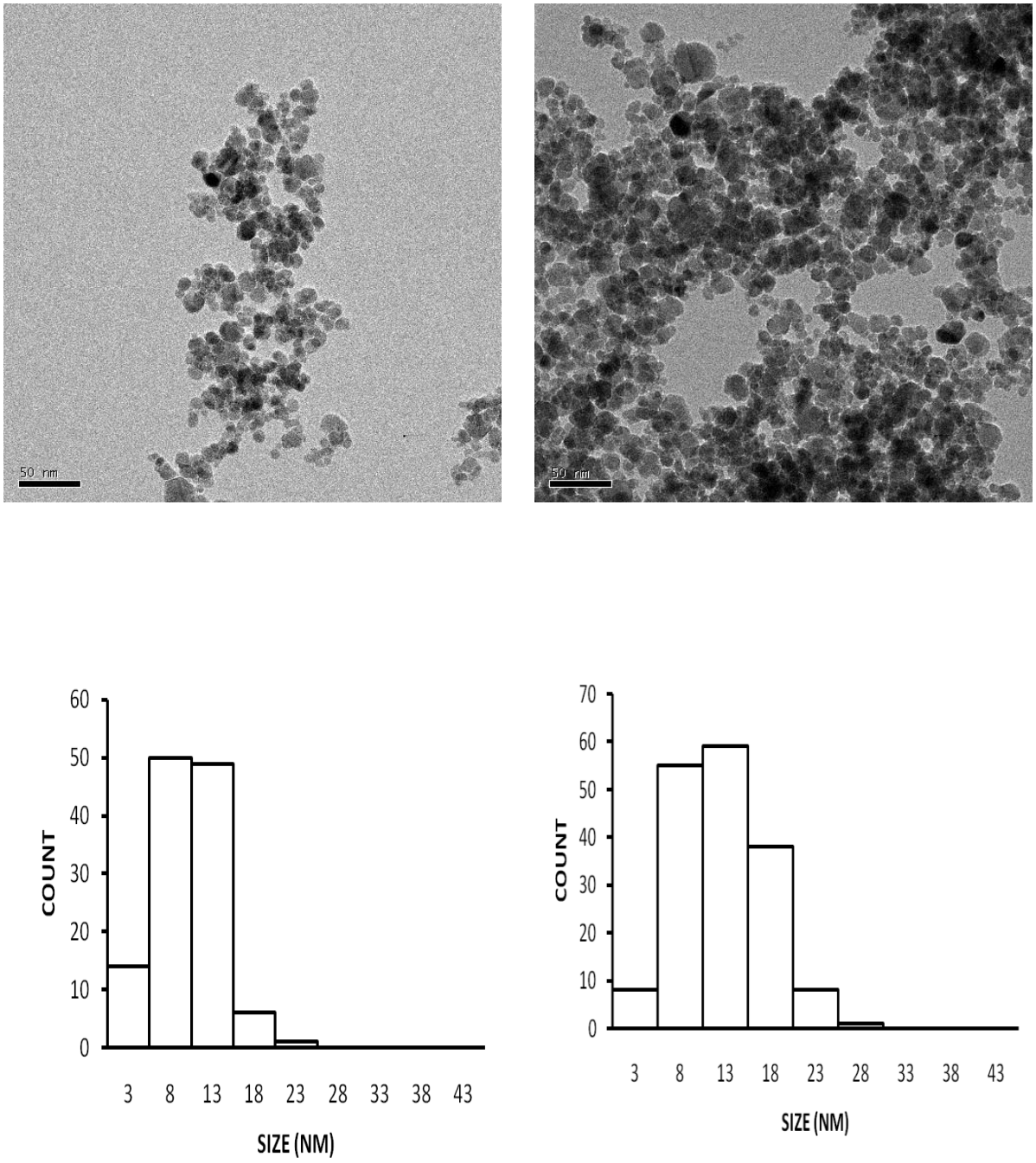

Figure 3.10 SEM images and particles size analysis of individual magnetite grains obtained at a lower resolution.

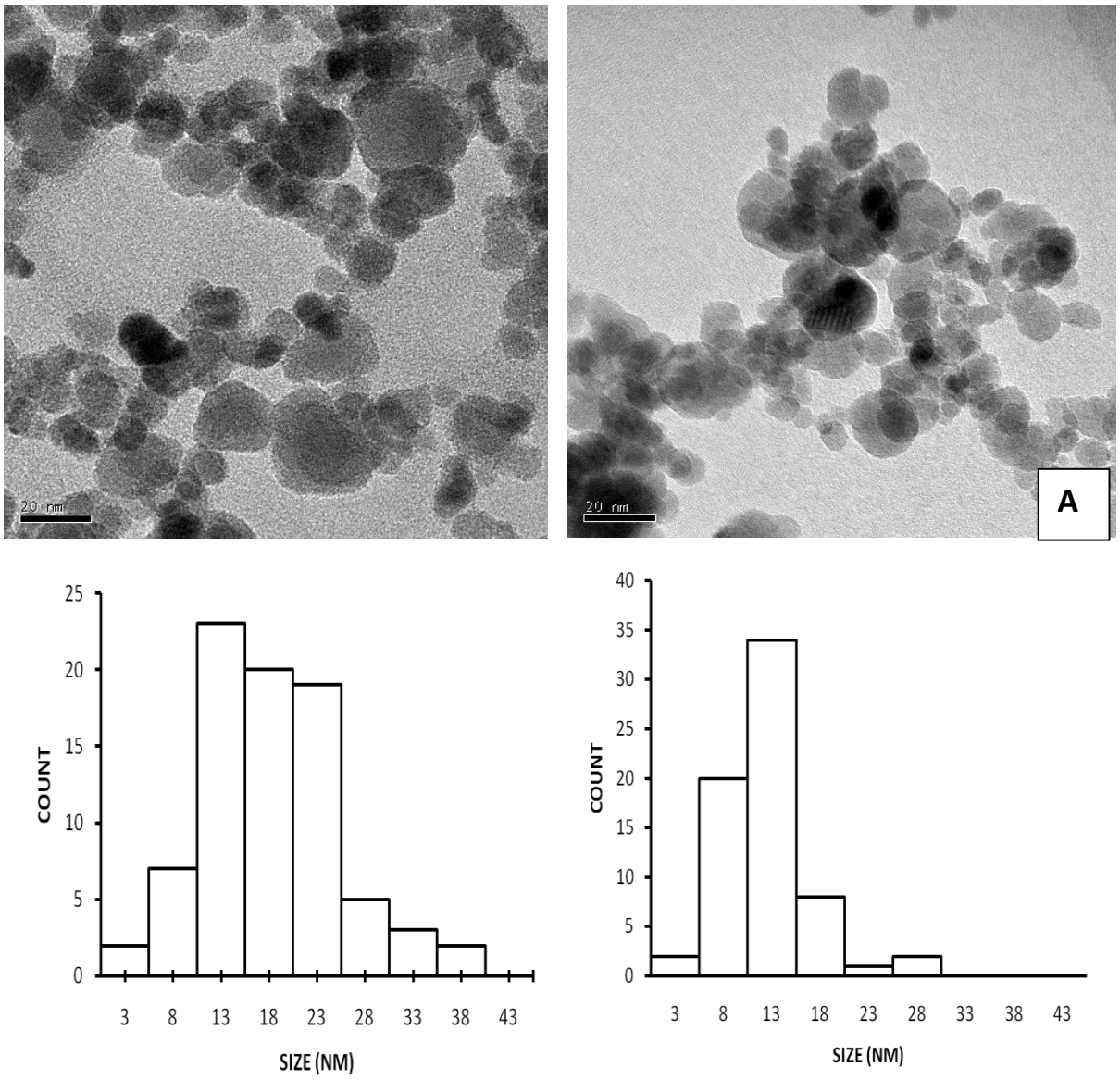

Figure 3.11 SEM images and particles size analysis of individual magnetite grains obtained at a higher resolution.

3.4.3 Mossbauer Results

The samples were prepared for Mossbauer spectroscopy by compressing the MNP in a sample holder. Figure 3.12 shows the Mossbauer spectra of the samples (MGS1 and MGS2) obtained at 4K and showed typical magnetite crystal phase as expected. This spectra showed the presence of superparamagnetic particles that are magnetically ordered. The spectra is well resolved with magnetic splitting of the nuclear enrgy states with the presence of six peaks. The samples were first analyzed to determine the consistency in the sample preparation. The two samples shown in Figure 3.12 show a close fit in the spectrum obtained. This was an indicative of a good control of the process parameters used in the co- precipitation technique.

The Mössbauer spectra obtained for the sample was then compared to a known spectra of nanoparticles that are of similar chemical composition. The characteristic spectra of hematite (Figure 3.13); maghemite (Figure 3.14) and magnetite (Figure 3.15) were used. The magnetite sample (MGS1) prepared in the lab were found to be a close fit with the known spectrum of magnetite. The small particle size might explain the broadening of the line of the spectra of the samples and hence the absence of the sharp peaks in the sextets.

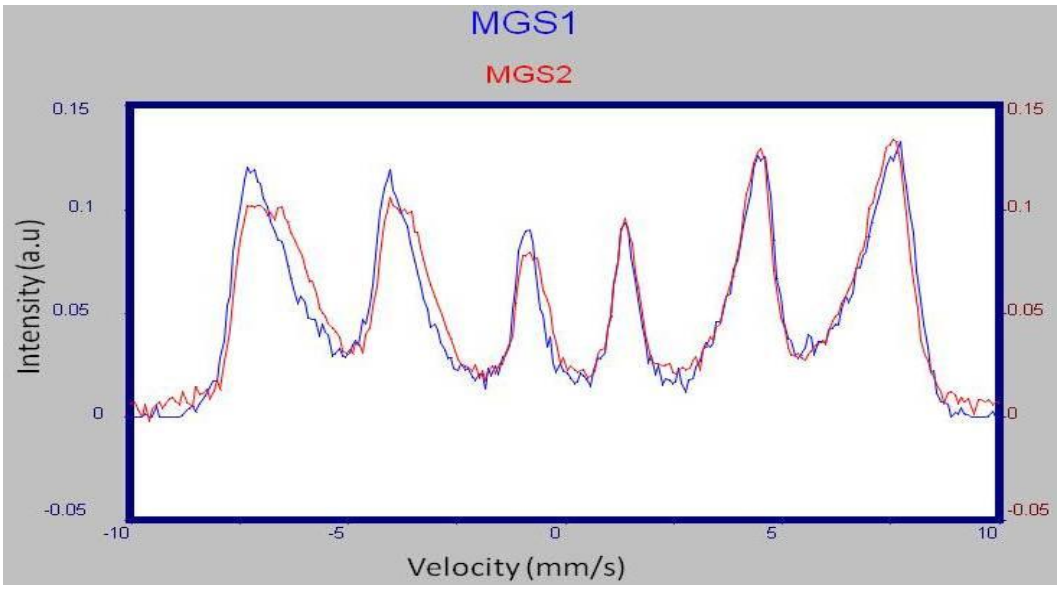

Figure 3.12 A comparison of two samples of magnetite prepared by co-precipitation to confirm consistency in the preparation technique.

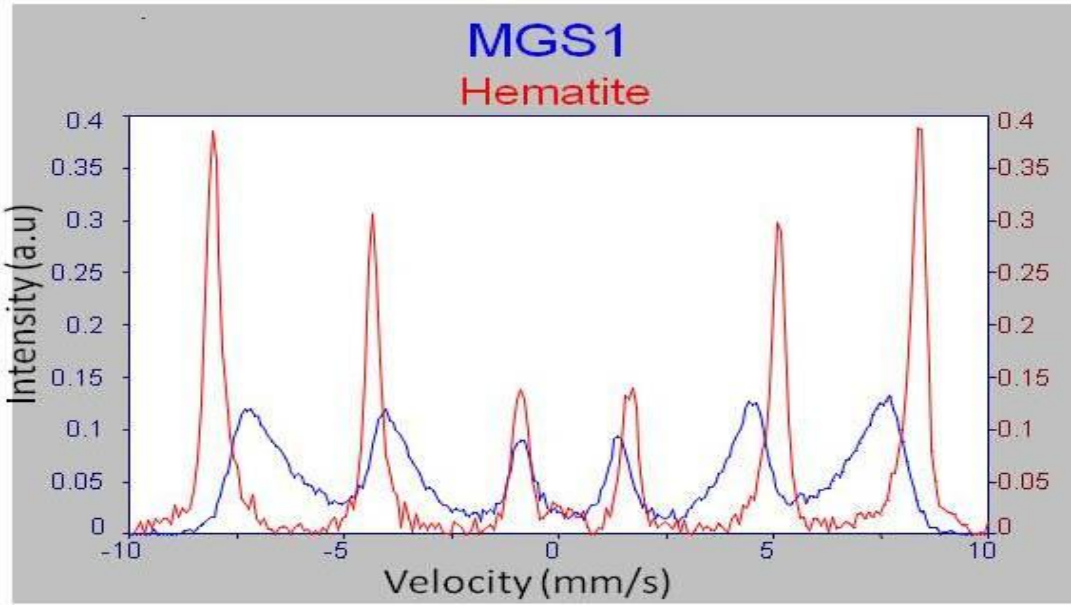

Figure 3.13 A Mossbauer comparison of my sample (MGS1) with characteristic hematite spectra. The two sextets are not a close fit.

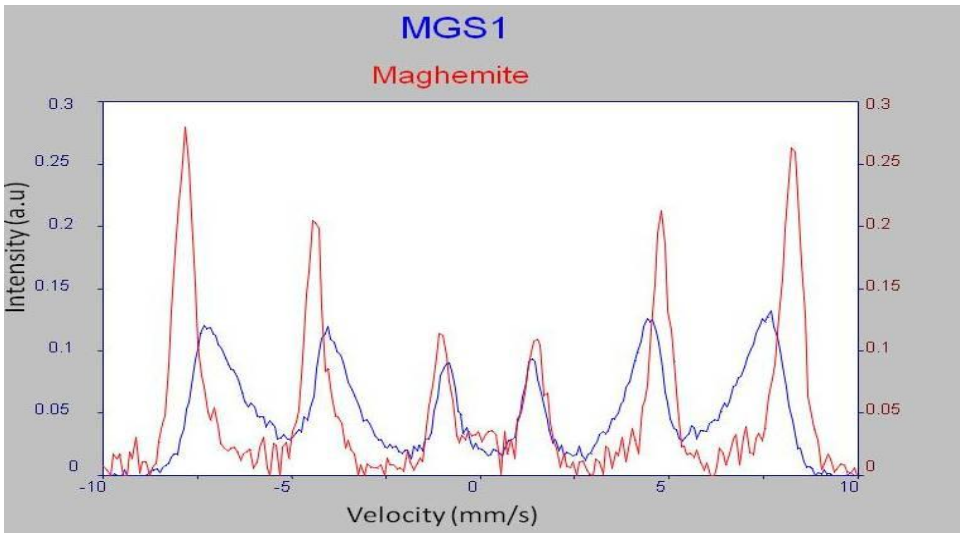

Figure 3.14 Mössbauer spectra of my sample of magnetite (MGS1) with maghemite.

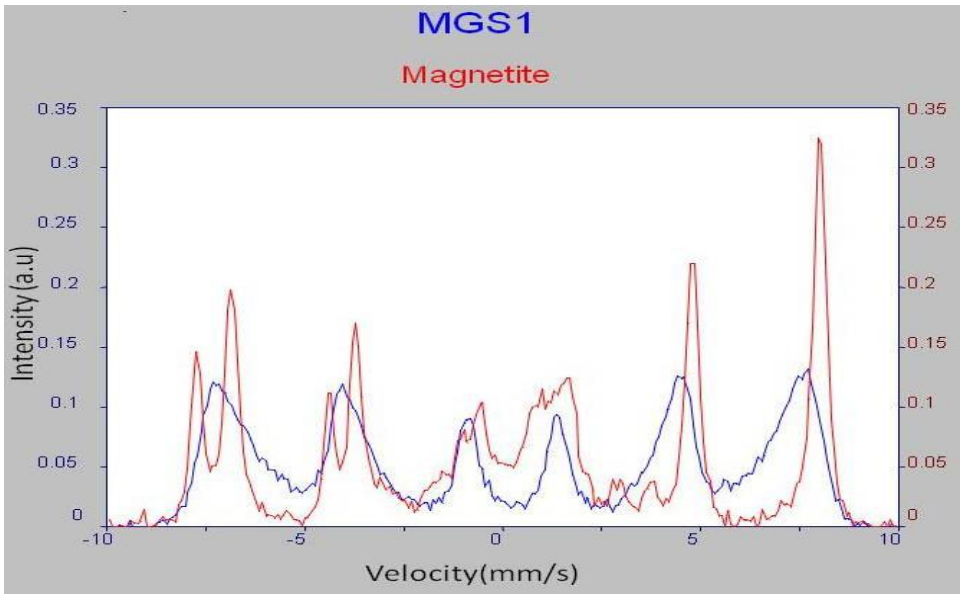

Figure 3.15 Mössbauer spectrum of the magnetite sample compared with a known spectrum of magnetite showing a close fit. The broadening of the spectrum is due to the small size of the particles.

3.5 Conclusion

MNP of cobalt zinc ferrite and magnetite were prepared by co-precipitation method. These particles were characterized by X-ray diffraction, TEM and Mossbauer spectroscopy. Results from x-ray reveal the crystalline nature of the MNP with an average size of 10.13 ± 0.24 nm.TEM results show particle size close to those of x-ray with good monodispersity. Mossbauer results confirm good control of process parameter in sample preparation

CHAPTER 4

METHODOLOGY II: PREPARATION AND CHARACTERIZATION OF DRUG LOADED MAGNETIC NANOCOMPOSITE SPHERES

4.1 Introduction

The use of the synthetic polymers as surface coatings forms an integral component of all MNP platforms for biomedical applications [30]. The efficacy and safety of many new and existing drug therapies may be enhanced through advanced -release systems by using polymer particles [133]. PLGA is one of the many synthetic polymers approved by FDA found to be biocompatible with the body and is capable of degrading to by products that are easily cleared by the body [133].

During the process of degradation the therapeutic agent are released. The rate at which the polymer degrades optimizes the bioavailability of the active drug to the body, thus decreasing harmful side effects of the drug, increasing the effectiveness of the drug and reduction in wastage. The ability of the polymer to serve as an efficient drug-MNP carrier system are affected by the nature of the chemical structure of the polymer (e.g. hydrophobicity/hydrophilicity, biodegradation characteristics, etc.), the length or molecular weight of the polymer, the manner in which the polymer is anchored or attached (e.g., electrostatic or covalent), the conformation of the polymer, and the degree of particle surface coverage [30].

This study aims to prepare magnetic nanocomposite spheres by encapsulating the MNP and an active drug 5-FU into PLGA. There exist several encapsulation techniques. Current

techniques in preparation of drug loaded nanocomposite sphere include: emulsion polymerization processes and emulsion/solvent evaporation techniques. Polymerization methods have been used by various groups to achieve spheres with a particles size distribution ranging from 50nm to 300nm [134,135]. Fessi and co workers [136] used emulsion polymerization to prepare microspheres. They found an increased risk of chemical reaction between the reactive monomers and the drug and also residues from the various surfactants and solvents used in the process.

Of interest in this study is the oil-in-oil emulsion/solvent evaporation method. This process involves the use of a preformed polymer and provides a much higher drug loading of up to 50% (w/w) [137, 138]. The MNC spheres prepared are then characterized by DLLS, TEM and SEM techniques in order to determine the sphere size, shape and morphology. The magnetic properties of these spheres were then analyzed using SQUID magnetometer. The spheres were also used to carry out fluid flow studies in the presence of a magnetic field and cytotoxicity evaluation.

4.2 Experimental

4.2.1 Materials

PLGA 50:50 lactic acid: glycolic acid ratio and molecular weight (mw) of (40,000 - 75,000) was purchased from sigma-Aldrich and used without further purification. Span-80 (a surfactant), carbon tetrachloride, paraffin oil, hexane and acetonitrile were purchased from Fisher Scientific and used as received.

4.2.2 Methods

The nanocomposite spheres were prepared in two consecutive phases shown in Figure 3.2. In the first phase, PLGA was added to 5 ml of the solvent acetonitrile in a conical flask. The solution was stirred using a mixer with a magnetic bar until all the PLGA was completely dissolved. The magnetic nanoparticles and a drug were added to the solution after the magnetic bar was removed. Samples of the 5-FU drug were used in our trials. Magnetite and Co-Zn ferrite MNP were used in these trials at ratios equivalent to 10, 15, and 20% of MNP in each sample. The MNP were dispersed for 10 minutes using a sonicator.

The second phase of preparation began by adding 5ml of a surfactant (Span 80) to 40 ml of viscous paraffin liquid. The thick/viscous solution was then placed under a high speed mixer operating at 7000 rpm to ensure the surfactant and other entities were well dispersed in the paraffin. The product from the first phase was then added drop-wise into the second-phase solution using a burette. The mixer was allowed to run for about 1.5 hrs. This process allowed the solvent acetonitrile to evaporate fully out of the mixture to make dry spheres. The drug carrying nanocomposite spheres were then collected by centrifuge from the paraffin, washed with hexane and carbon tetrachloride, filtered and dried at room temperature.

This process is well illustrated in Figure 4.1 and is available in Appendix 3. The magnetic nanocomposite spheres were then characterized to determine the particle size by SEM. TEM was used to determine the MNP dispersion in PLGA. SQUID technique was used to determine the magnetic properties of the composite sphere.

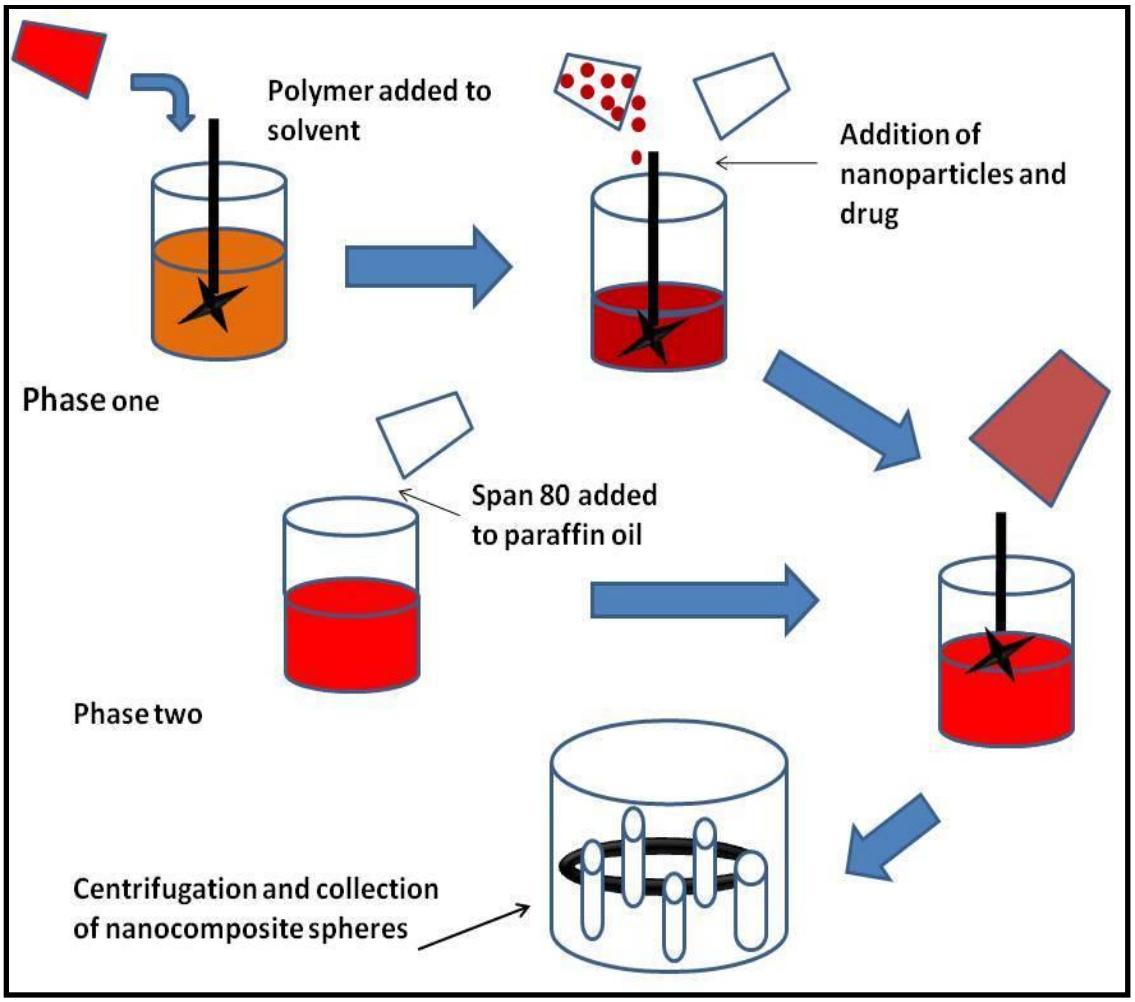

Figure 4.1 Preparation of magnetic nanocomposite spheres by emulsion/solvent evaporation method.

4.3 Nanocomposite Characterization

4.3.1 Dynamic Laser Light Scattering (DLLS)

DLLS is a technique used to measure the size distribution profile of small particles in a suspension or polymers in a solution [159]. The data collected is used to determine the sample distribution of the given sample of MNC spheres. Since these particles are small, they undergo Brownian motion so that the relationship between diffusion and particle size can be determined. An analysis of the time dependence of intensity fluctuations yields the diffusion coefficient of

the particles. Using Stokes Einstein equation, the hydrodynamic diameter (d_p) can be computed as is seen in equation (4.1):

$$d_p = \frac{K_B T}{3\pi\eta D} \tag{4.1}$$

where η is the solvent viscosity, K_B is the Boltzmann's constant and D is the diffusion coefficient.

Dynamic light scattering is a powerful technique in the protein crystallography and nanotechnology area which allows the user to measure hydrodynamic radius, Polydispersity and the presence of aggregates in protein samples and nanoparticle suspensions [160]

4.3.2 Scanning Electron Microscopy (SEM)

The SEM is one of the most versatile instruments available for the examination of the micro structural characteristics of a solid object [106]. With SEM one can obtain high resolution (1nm-5nm) images in three dimensions. The SEM is composed of a lens system, an electron gun, electron collector, visual and recording cathode ray tubes and electronics associated with them [106].

The SEM does not produce a true image of the sample specimen but rather a point by point reconstruction of the sample from a signal emitted the sample when illuminated by a high energy electron beam [107].The ultimate resolution of the SEM is determined by the minimum escape volume of the electrons emitted from the sample surface at that pixel level [108].

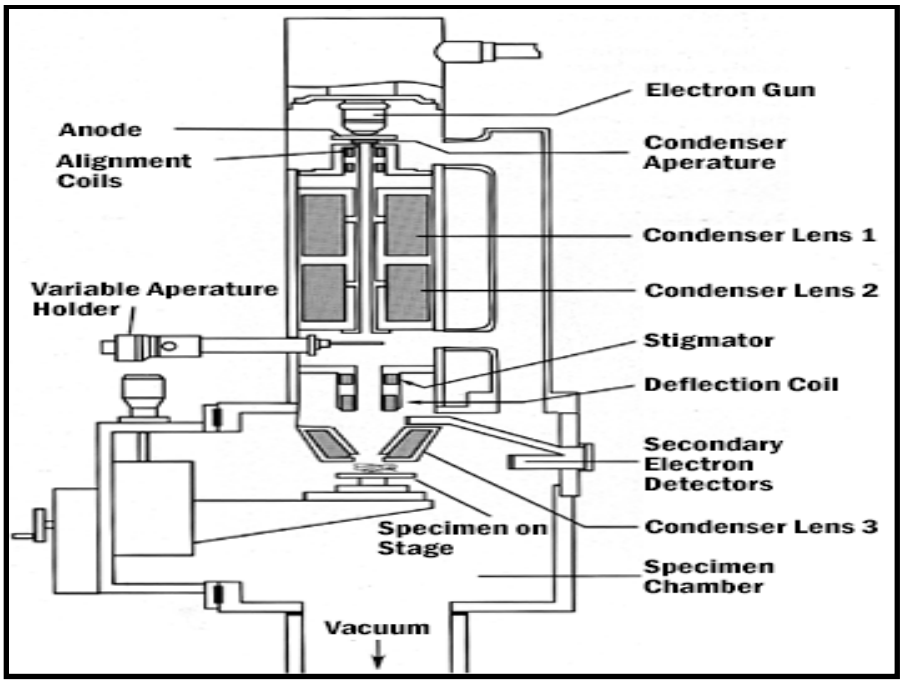

Figure 4.2 Structure of SEM showing the parts [161]

4.3.3 Superconducting Quantum Interference Devices (SQUID)

SQUID is a technique used to measure the temperature dependence of magnetization. With this technique, extremely small magnetic signals can be detected and precisely measured. SQUID uses the properties of electron pair wave coherence and Josephson junctions to detect very small magnetic fields [111]. This technique was first developed by Cooper, Bardeen and Schrieferr [102]. The superconducting materials are cooled first to a temperature way below the superconducting transition temperature. This process will arrange the cooper pairs of the electrons in the material forming a single macroscopic quantum state with two electrons of opposite spin, in zero magnetic fields (zero momentum). The current generated by such a pair creates a magnetic flux which is quantized and given by the equation (4.2).

$$\Phi_0 = \frac{h}{2e} \tag{4.2}$$

where $_0$ represents the quantum fluxes, h the Planck's constant and e is the charge.

In 1962, Brian Josephson predicted that if a thin insulator was placed to separate the two super conductor half rings, the electron cooper pair tunnels between the rings when there is no external magnetic or electric fields (DC) across the junction when an alternating current is applied. This phenomenon (Josephson Effect) leads to coherence between the super conductors

In this experiment a SQUID magnetometer was used to measure the temperature dependence of magnetization at a temperature range 0- 300K and constant external magnetic field of 1000 Oe. The measurements obtained were both for Field cooling (FC) and zero field cooling (ZFC). To obtain the FC measurements, the sample was initially cooled down to 0 K in the presence of a magnetic field and then data collected when the temperature in increased. The ZFC were obtained by cooling the sample in the absence of the magnetic field before collecting the data on moments at 1000 Oe. From this data, transition temperatures were determined. The SQUID magnetometer was also used in the experiment to obtain the magnetization as a function of external field (Magnetic hysteresis) of the sample at 300K. The samples were exposed to magnetic field in the range of 0 to 10000 Oe and data collected on the magnetic moments.

4.4 Results and Discussion

4.4.1 DLLS Results

The size distribution of the nanocomposite spheres were analyzed using DLLS technique. Table 3 shows a summary of the particles sizes of different samples and their Polydispersity. The mean particle size was found to be 921nm with a standard deviation of ± 95.4. The Polydispersity

index of the samples was in the range 0.07 to 0.21. This index is a measure of the distribution of molecular mass in a given polymer sample. The data was then plotted on the graph in Figure 4.3.

The increase in the concentration of MNP is found to be proportional to the increase in the particle size while the particle size distribution remains unchanged. A likely explanation for this observation may be that the increase in the amount of MNP caused an increase in the viscosity of the oily phase with constant stirring by the mixer.

TABLE 3

SIZE DISTRIBUTION OF MNC DETERMINED BY DLLS

Sample number	PLGA concentration (w/v %)	MNP concentration (w/w %)	Size (nm)	Polydispersity
1	1.25	5	849.5	0.085
2	1.25	10	887.2	0.064
3	1.25	20	1009	0.214
4	1.25	30	1037	0.147

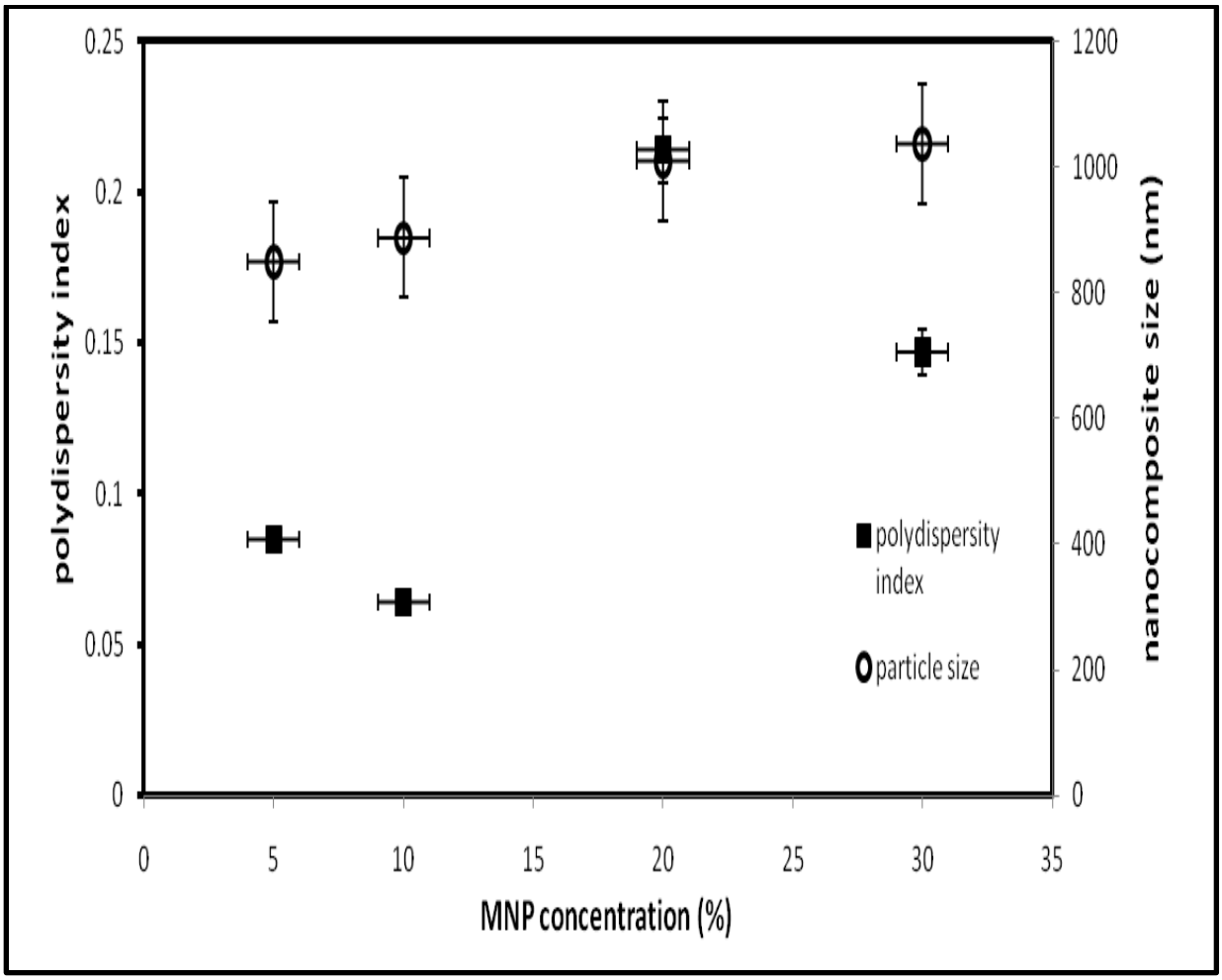

Figure 4.3 Polydispersity index and particle size versus MNP concentration in the MNC sample.

4.4.2 TEM Results

The TEM images given in Figure 4.4 are of nanocomposite spheres showing the embed MNP clearly. They were obtained using a Phillips electron microscope and analyzed using a histogram to determine the particles size distribution. A particle size analysis of the MNP revealed a near uniform particle size distribution within each polymer matrix. This can be seen by the clustering of MNP in specifics regions where nanocomposite spheres are located. Looking

at the MNP closely reveals their crystalline nature. This is also observed in the TEM image where the crystal lattices are clearly visible. Further analysis of the image in Figure 4.5 was done by deriving the particle size distribution in the sample shown in Figure 4.6. The mean size was found to be 12.3 nm.

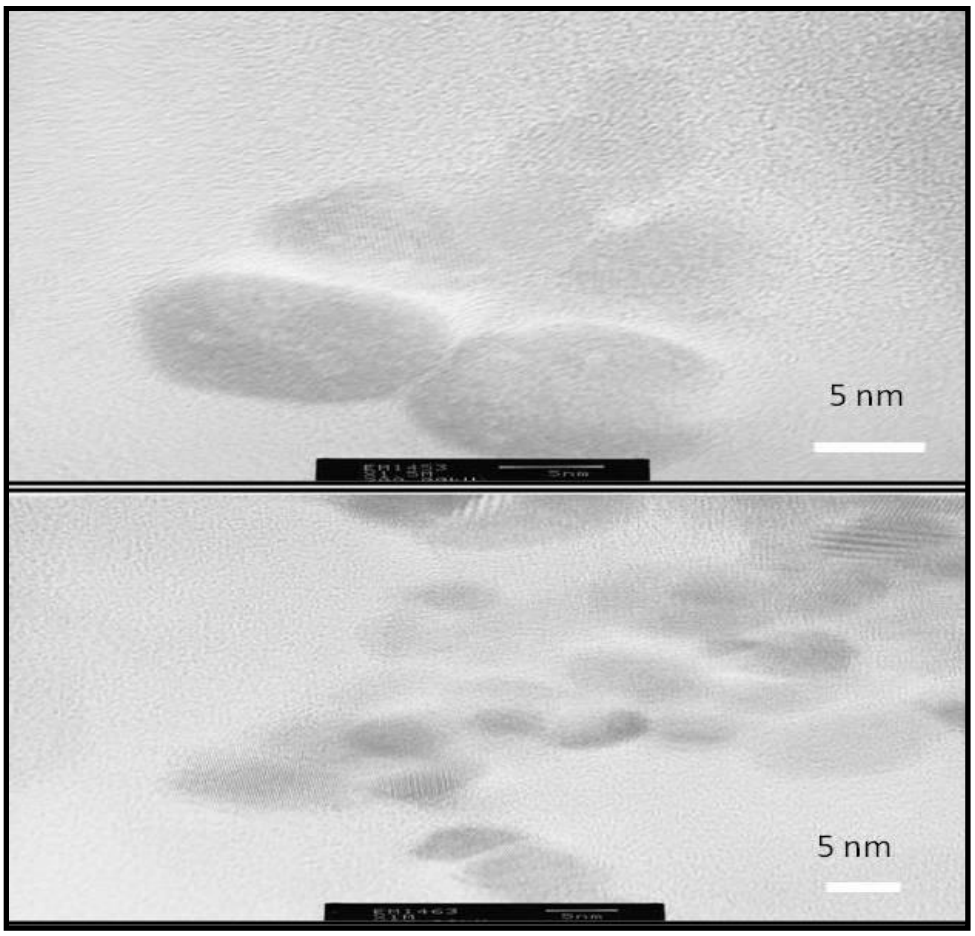

Figure 4.4 TEM micrographs of magnetite MNP. The crystal lattices are visible both TEM images. A close examination of each image shows the near spherical nature of the particles.

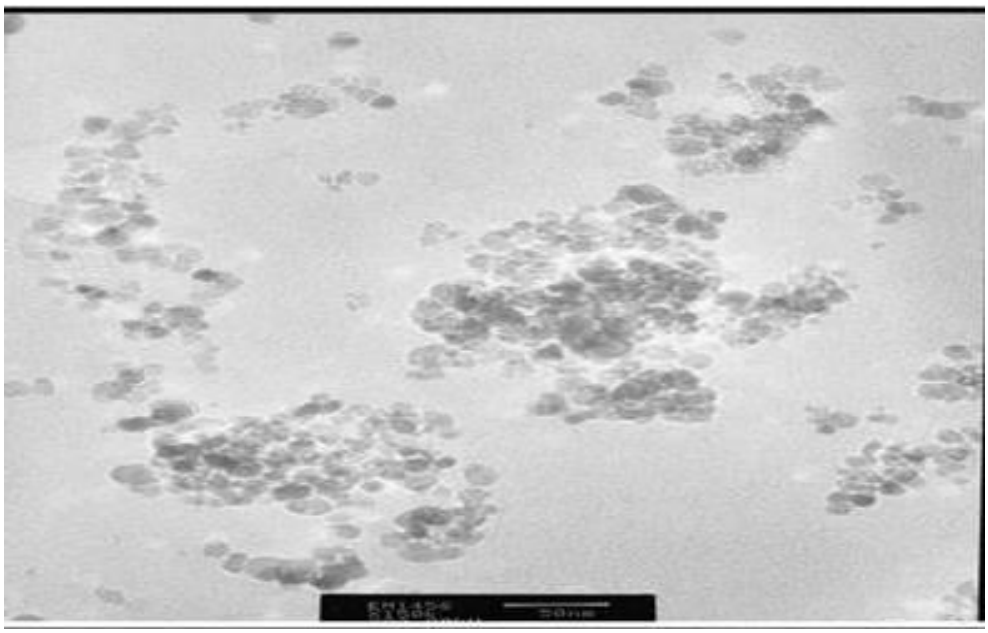

Figure 4.5 TEM images of MNC spheres showing the distribution of the Fe_3O_4 nanoparticles within the polymer matrix (50 nm bar).

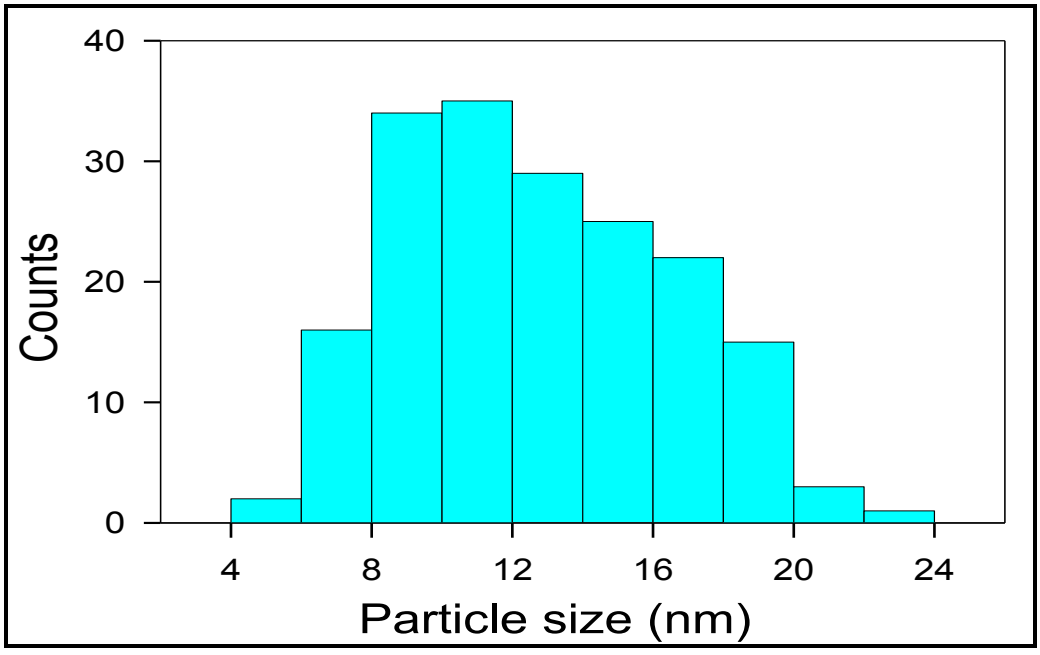

Figure 4.6 Size distribution of Fe_3O_4 MNP obtained from the TEM image. Solid line is the best fit.

4.4.3 SEM Results

When the MNP and the drug 5FU were embedded in the PLGA, they formed a MNC sphere. The SEM images in Figure 4.7 show large magnified MNC spheres that contain magnetite nanoparticles. The increased resolution reveals the spheres with good encapsulation. There are sphere size differences in the SEM of samples shown. A few larger particles are observed in comparison to many smaller particles. The variation of the sphere sizes in a given sample can be minimized by the use of a filter to separate the larger ones from the small spheres.

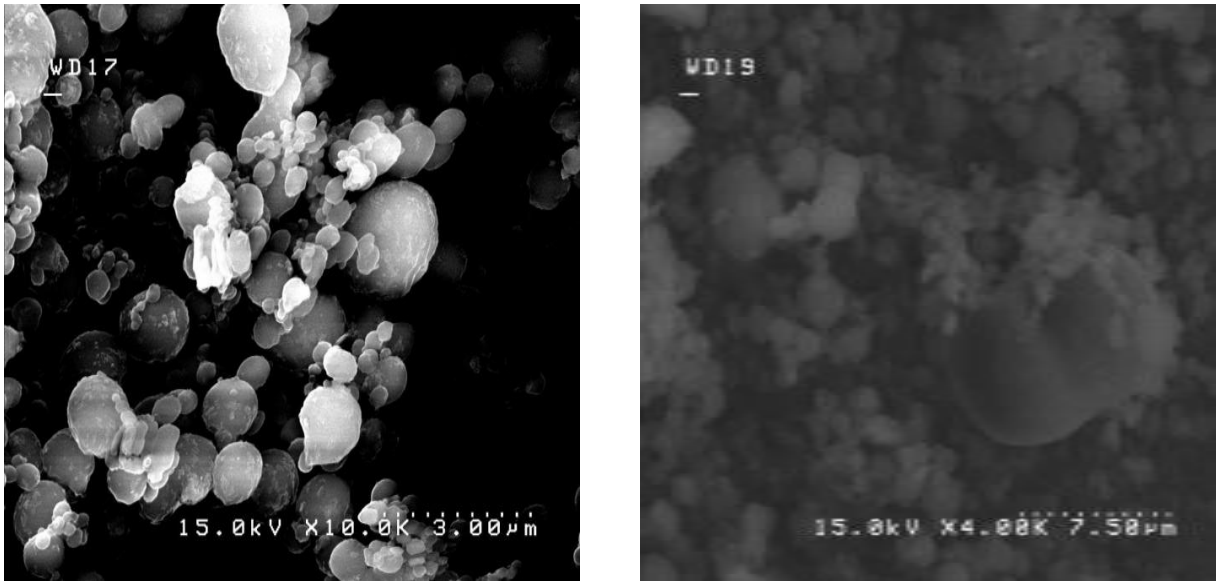

Figure 4.7 The SEM images of the MNC spheres obtained at the same acceleration voltage of 15 KV and a working distance of 19.

4.4.4 SQUID Results

Samples of MNC spheres used for SQUID measurements were prepared with the MNP concentration as a percentage of the PLGA contents. Table 4 shows samples of MNC spheres containing magnetite nanoparticles prepared for magnetic measurements.sample table for Cobalt zinc ferrite is found in Appendix 4. One of the samples labeled S_5 was also encapsulated with a test drug. The magnetic measurements under field cooling (FC) and zero field cooling (ZFC) were obtained at a constant field of 1000 Oe for a temperature range between 4K and 300K.

TABLE 4

MNC SPHERES PREPARED BY OIL IN OIL EMULSION SOLVENT EVAPORATION

SAMPLE	MASS(mg)	% OF MAGNETITE	% OF DRUG
S_2	3.71	10	0
S_3	3.55	20	0
S_4	3.87	25	0
S_5	3.1	20	20

Figures 4.8, 4.9 and 4.10 show the FC and ZFC temperature depended magnetization curves of the samples S_2, S_3, and S_4 containing 10%, 20%, and 25% of magnetite MNP respectively. These curves were obtained at 1000(Oe). The temperature was first reduced to 4K using liquid helium and then increased to 300K. The ZFC magnetization of the magnetic spheres is seen to increase consistently to a peak value of 1.72 emu/g and a blocking temperature of between 40K and 80K as is seen in Figure 4.8 with sample S_2.

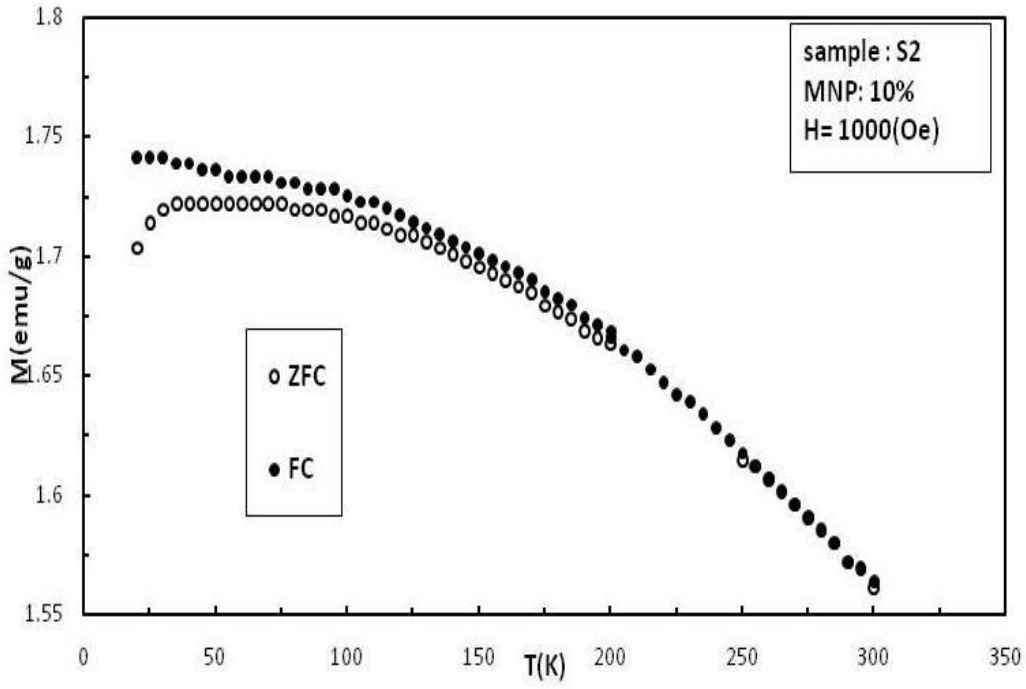

Figure 4.8 The FC and ZFC curves of sample (S2) containing 10%, magnetite concentration in MNC sphere obtained from 4K to 300 K in a constant applied field of 1000 Oe.

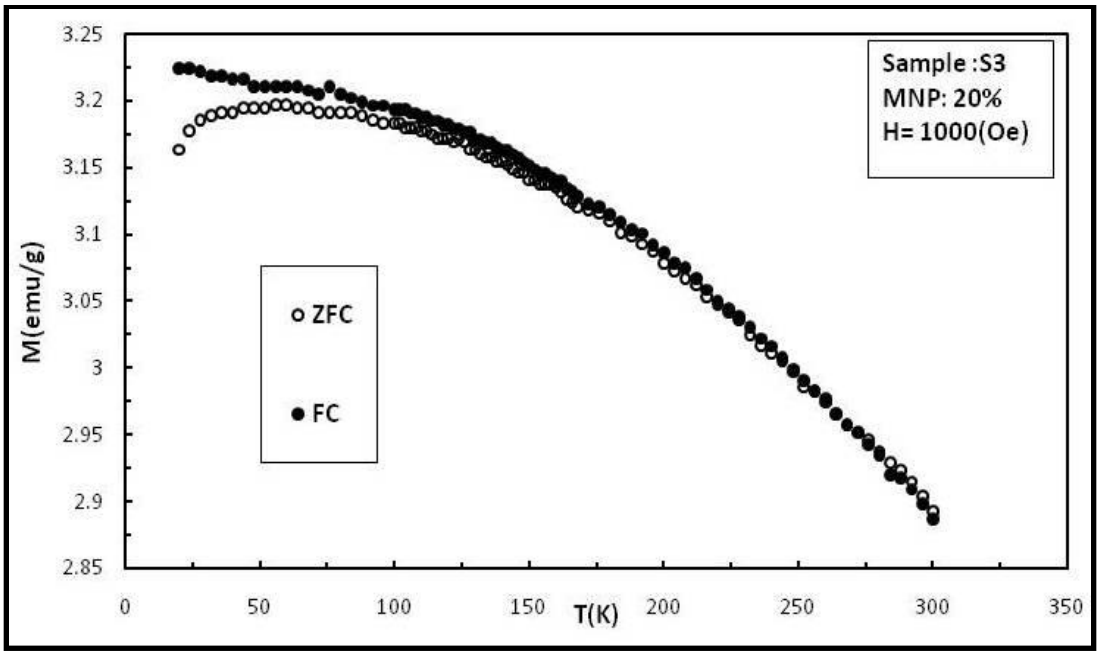

Figure 4.9 FC and ZFC curves of sample (S3) containing 20% magnetite.

This characteristic behavior implies the presence of magnetic order up to 40K which is the blocking temperature (T_B). T_B increases to around 80K for the other two samples in Figures 4.9 and 4.10. Above T_B, the magnetic spheres show superparamagnetic properties, that is consistent with the nanometers. T_B for the sample shown in Figure 4.11 increases to about 80K. This increase could be attributed to the increased separation between the nanoparticles due to the presence of the drug.

The separation between the FC and ZFC curves in the sample with the drug in Figure 4.11 is much greater than that of the other samples with a value of T_B still in the range of 40K to 80 K. Since the ZFC and FC magnetization curves merge at lower temperatures in all the samples, this is indicative of the presence of fewer particles with a larger distribution in the sample.

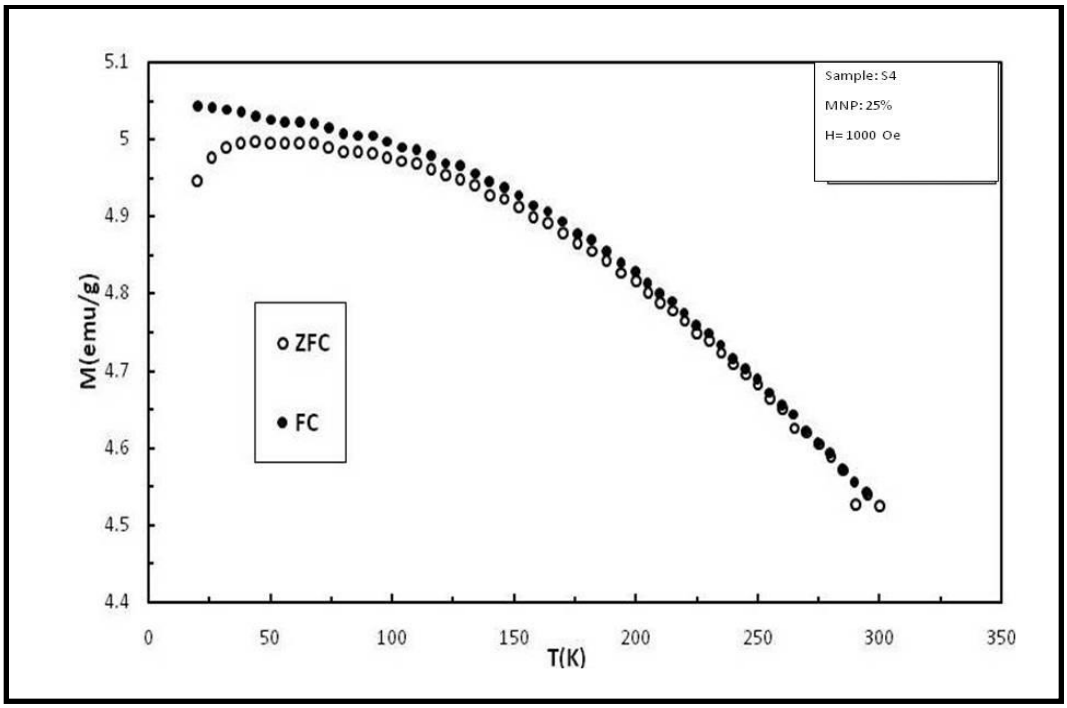

Figure 4.10 The FC and ZFC curves of sample S4 containing 25% magnetite.

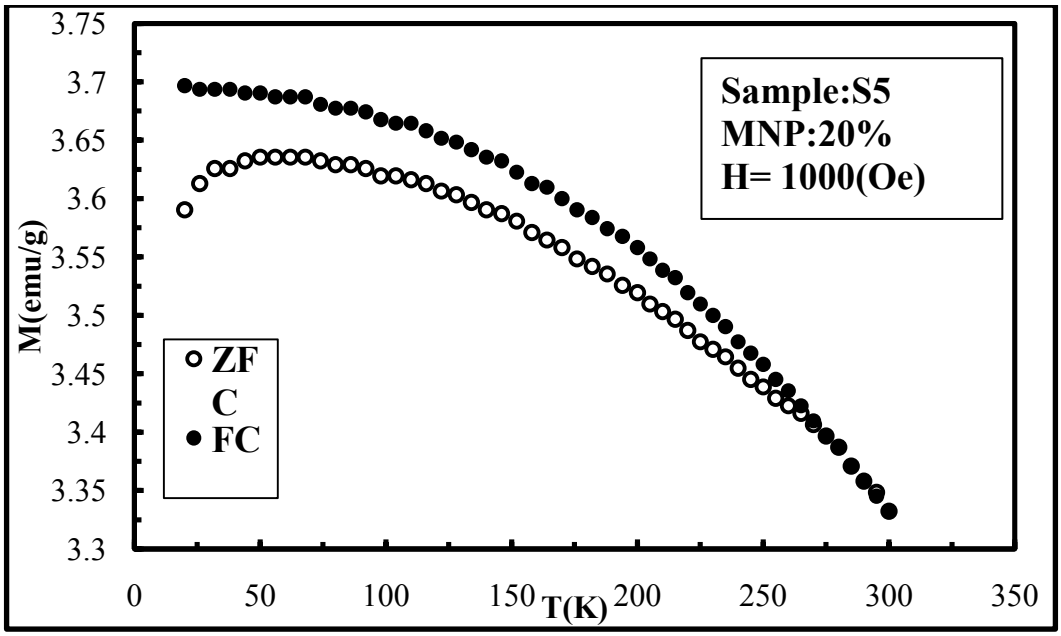

Figure 4.11 The FC and ZFC curves of MNP encapsulated with a sample (S5) of MNP and drug in a polymer PLGA.

Figure 4.12 shows the specific magnetization vs. applied field curves of the MNC spheres containing magnetite obtained at 300K. The applied field used was between -10,000 and 10,000 Oe with a sensitivity of about 0.1emu/g. The magnetization curve shows an increased magnetic saturation from 0 to 4.2 (emu/g) with magnetic loading. This increase was attributed to increased magnetic moments per unit volume.

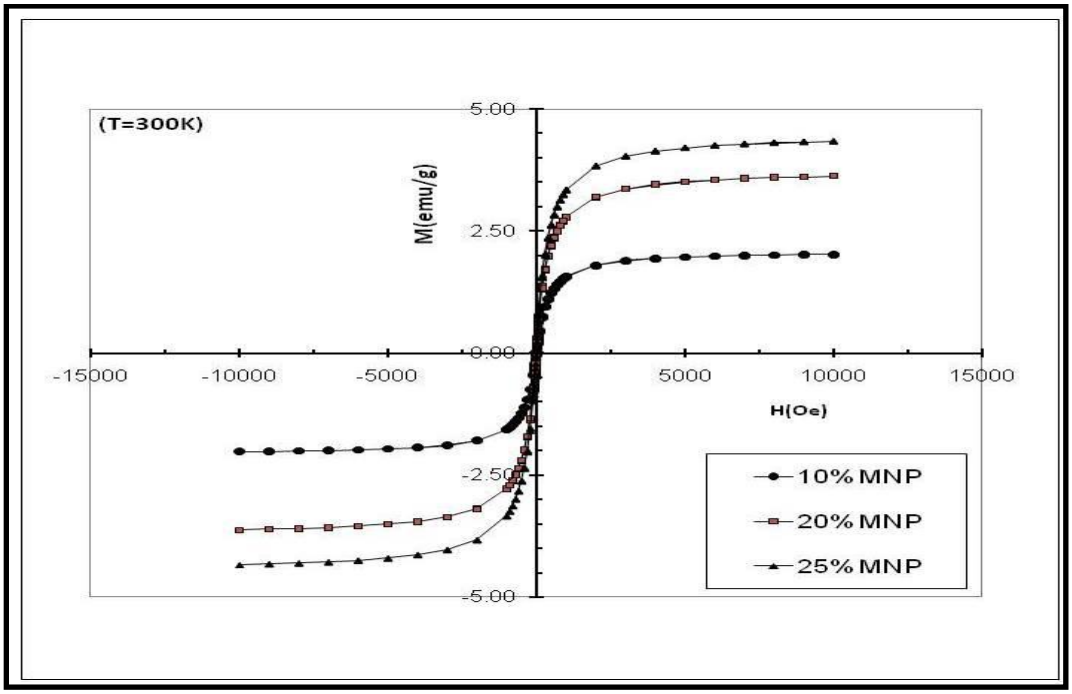

Figure 4.12 SQUID test results showing specific Magnetization vs. Applied field of three samples of Magnetite obtained at 300K. The graph shows zero remanence and coercivity a characteristic of super paramagnetic materials.

In Figure 4.13, the SQUID data is presented in terms of zero-field-cooled (ZFC) magnetization of three samples with 10, 15 and 20% of $Co_{0.5}Zn_{0.5}Fe_2O_4$ nanoparticles in PLGA, respectively,. The peak for each curve represents the maximum magnetization of the samples, so there is a clear increase in the magnetization as the concentration of the MNP increases. The broad peaks may reflect the wide range of particles sizes [87].

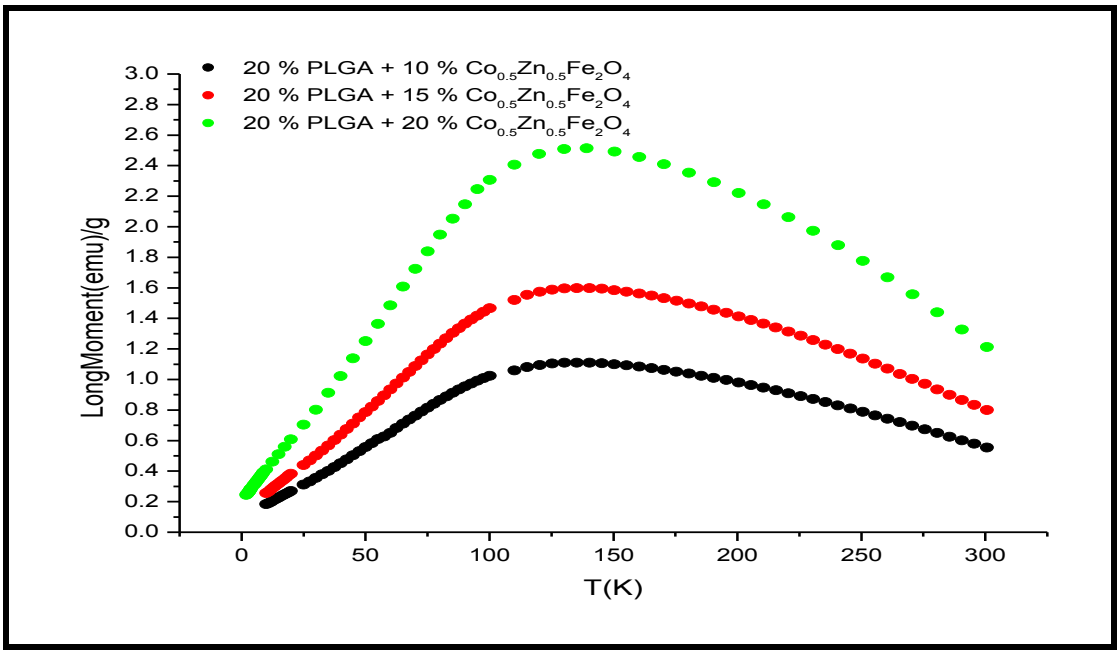

Figure 4.13 Temperature dependence of magnetization of three samples containing 10%, 15% and 20% of MNP of $Co_{0.5}Zn_{0.5}Fe_2O_4$ obtained at an applied field (H) of 1000Oe.

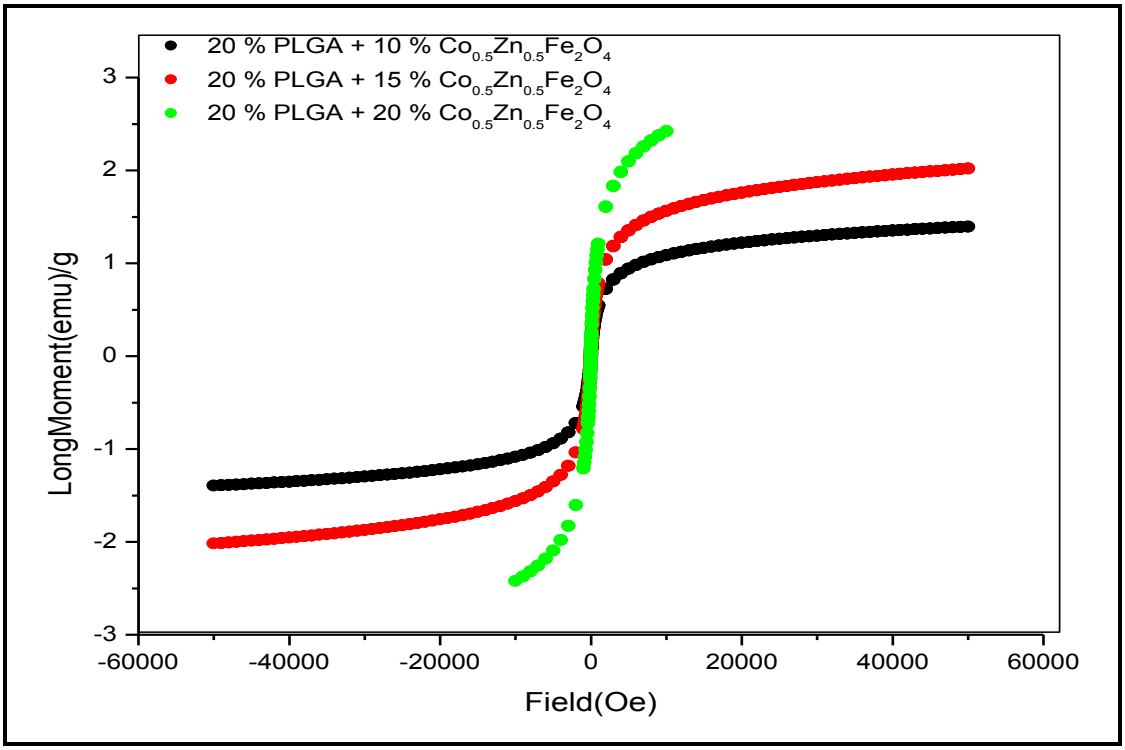

Figure 4.14 Magnetic hysteresis of MNC spheres obtained at 300K.

Figure 4.14 shows magnetic hysteresis in samples of $Co_{0.5}Zn_{0.5}Fe_2O_4$ at 300 K. All three samples yield zero remanence and coercivity. This is a characteristic of superparamagnetic nanoparticles at room temperature [88-91]. The magnetic properties of magnetite and $Co_{0.5}Zn_{0.5}Fe_2O_4$ are summarized in Table 5. From the table, the peak magnetization is observed to be higher in magnetite than in cobalt zinc ferrite.

TABLE 5

A COMPARISON OF MAGNETIC PROPERTITES OF MNP USED

Material	% MNP	T_B	M_S (300K)	M_r
$Co_{0.5}Zn_{0.5}Fe_2O_4$	10%	120-140	1.2	0
$Co_{0.5}Zn_{0.5}Fe_2O_4$	15%	120-140	1.8	0
$Co_{0.5}Zn_{0.5}Fe_2O_4$	20%	120-140	2.6	0
Fe_3O_4	10%	40-80	1.8	0
Fe_3O_4	20%	40-80	3.6	0
Fe_3O_4	25%	40-80	5	0

4.5 Conclusion

MNC spheres were prepared and successfully encapsulated with a drug using emulsion solvent evaporation method. The spheres were then characterized by DLLS, TEM, SEM and SQUID. The mean spheres size was found to be 921±95.4 nm using DLLS with a Polydispersity index in the range 0.07 to 0.21.TEM images obtained revealed the internal structure of the MNC sphere showing the presence of MNP in the sphere. These MNP had a mean size of 12.3 nm. SEM results show surface properties of the MNC spheres revealing their spherical nature with wide size distribution. The magnetization measurements obtained confirmed that the spheres retain the magnetic properties of the encapsulated MNP. The spheres are superparamagnetic at room temperature with high saturation magnetization; properties that are important in any magnetic drug delivery system.

HYDRODYNAMIC BEHAVIOUR OF MAGNETIC NANOMATERIALS UNDER HIGH MAGNETIC FIELDS

5.1 Introduction

The work presented in chapter 3 and 4 on fabrication and characterization of MNP and MNC spheres laid the foundation for this chapter. Previous efforts to study human blood flow systems in the proximity of a cancer tumor have relied on the use of in-vitro fluid flow experiments and CFD modeling (see Apendix 5) that mimic actual blood flow. A magnetic field placed near a tubing of varying geometry can be used to capture. MNC spheres within a fluid at the region of an interest. The percentage of MNC captured by the magnetic field will assist in determining the optimum concentration of MNP within the MNC sphere, magnetic field strength, the flow rate and the vessel diameter needed to provide successful dosing of the therapeutic agent. Once determined, these parameters can then be used in in-vivo trials to increase the efficiency of the delivery system.

5.2 Experimental Methods

Clear vinyl tubing (Sigma-Aldrich) of three different cross-sections were used to represent the typical blood vessels that would be used in in-vitro application. The dimensions of the tubing are shown in Table 6. Using connectors, the tubing were connected to a variable chemical pump (Fisher-Scientific) and calibrated to read flow-rate with a range from 0 to 16 ml/sec. The calibration was based on the slope of the graph illustrated in Figure 5.1.

TABLE 6

DIMENSIONS OF VYNIL TUBING USED IN FLUID FLOW EXPERIMENT.

Tubing label	Material	Inside Diameter(cm)	Outside diameter(cm)
A	clear Vinyl	0.1350	0.400
B	clear Vinyl	0.2300	0.540
C	Clear Vinyl	0.3125	0.625

1000 ml of the host fluid was prepared by mixing 90% by volume distilled water with 10% by volume glycerol. An electro magnet was used to provide a variable magnetic field across the tubing. The electromagnet was attached to a power source and a cooling system. The electromagnet provided a magnetic field between its spherical poles. A wooden holder shown in Figure 5.2 was prepared with holes in it to accommodate the vinyl tubing. The holder was placed between the poles of the electromagnet. This allowed the tubing to be placed in exactly the same spot during the trials. A Tesla meter connected to a probe was used to measure the magnetic field between the poles of the magnet. The host fluid was collected in a source beaker and MNP or MNC spheres added while dispersing by a sonic vibrator. A vinyl tube selected was connected to pass from the source beaker to the chemical pump as shown in Figure 5.3.

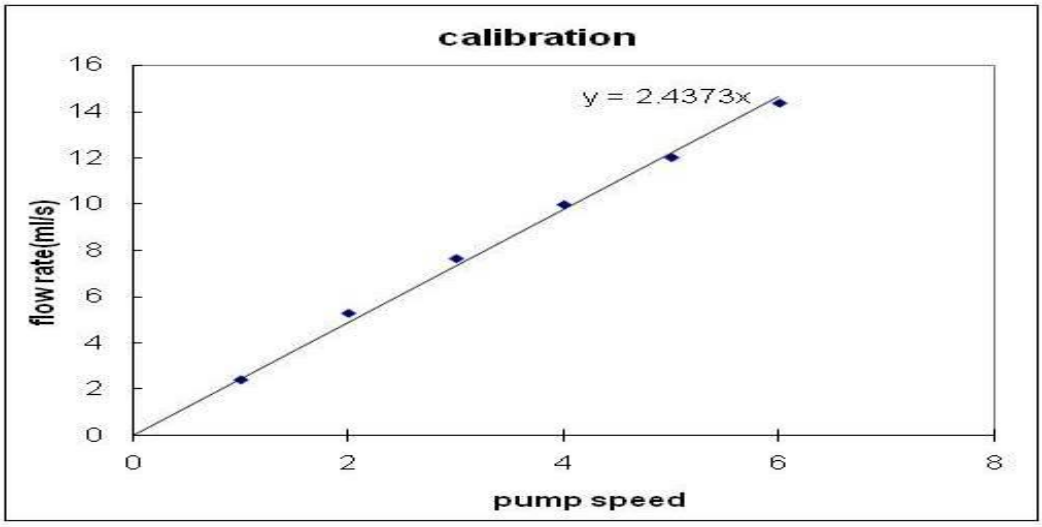

Figure 5.1 The graph above shows the calibration of the chemical pump to determine the flow rate. The range of calibration of the pump is from 0 to 14 ml/s.

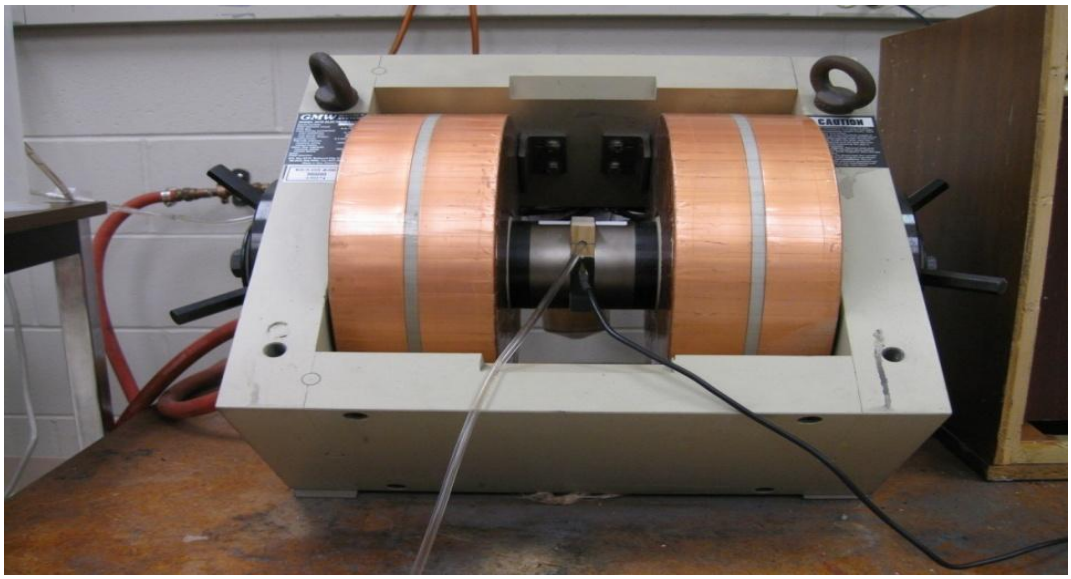

Figure 5.2 Electromagnet with the wooden support wedged between the poles. The vinyl tubing and the probe of the Tesla meter can be seen into the support.

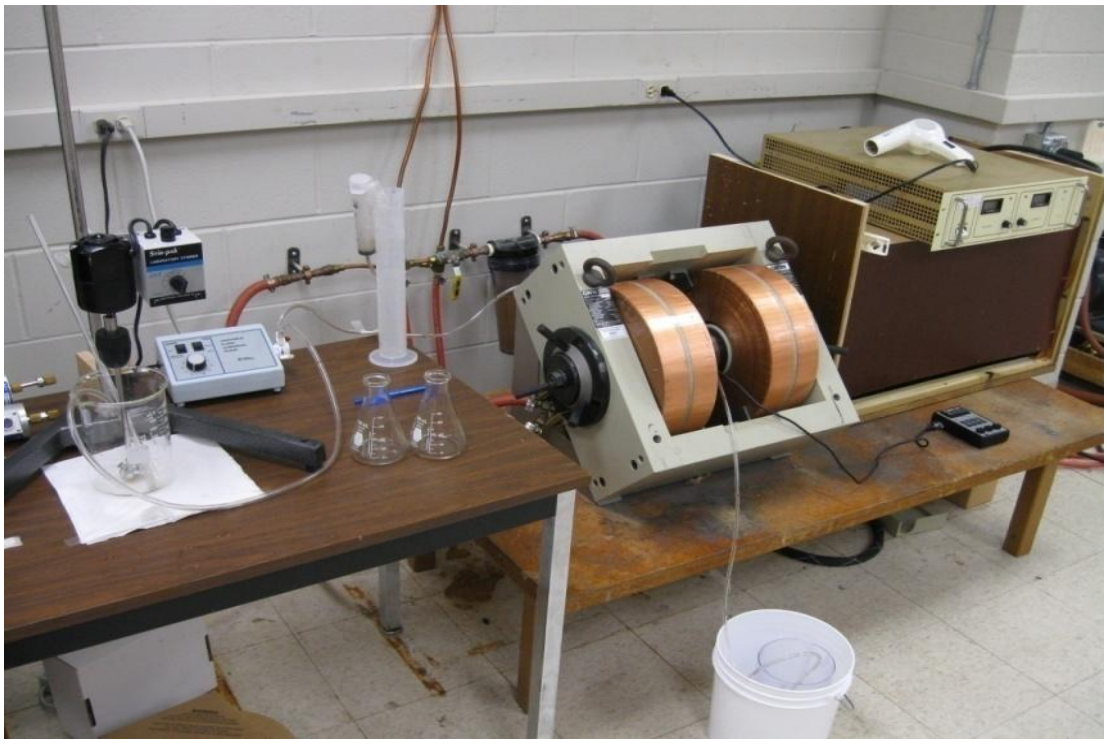

Figure 5.3 The experimental set-up shows the source and collection beakers, the variable chemical pump and tubing leading to the electromagnet. On the right, a Tesla meter is also attached to the electromagnet.

After the chemical pump, the tubing was made to pass inside the wooden support attached between the poles of the electromagnet. The probe of the Tesla meter was also placed in the wooden support and calibrated to read the magnetic field across the tubing. The tubing was then connected to the collection beaker. Keeping the magnetic field constant at 0.37 T, the host fluid was pumped through tube A at a constant flow-rate across the magnetic field. Some MNP were captured as shown in Figure 5.4 while the rest were captured at the collection beaker. The percentage of particles collected was determined. The percentage of MNP or MNC spheres captured was then determined. This experiment was then repeated for different flow rates. The magnetic field was changed to 0.47 T and the process repeated. Data was collected for all the tubing and percentages of MNP or MNC spheres determined for different magnetic fields and flow-rates.

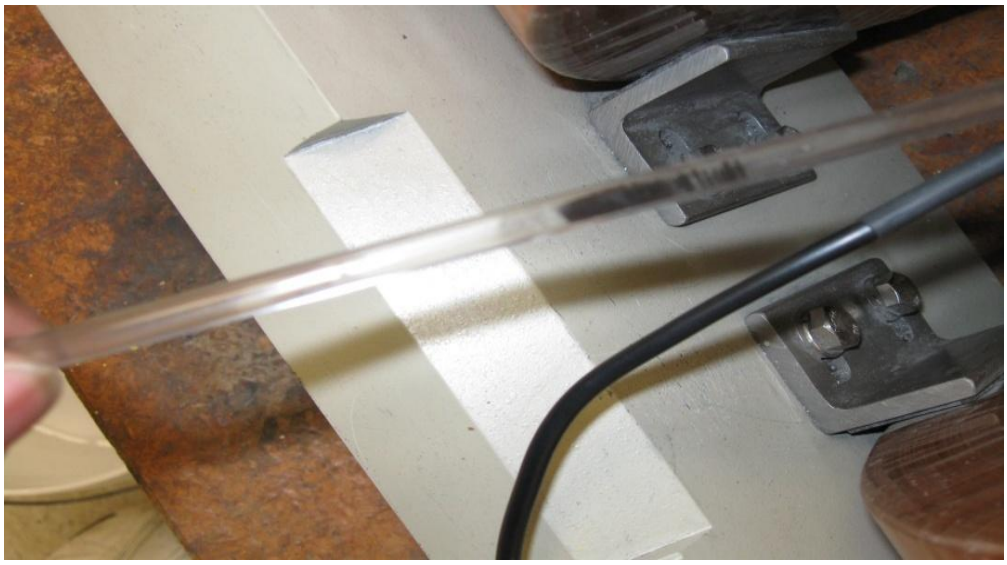

Figure 5.4 The MNP captured are seen when the pump and the electromagnet is turned off and the tubing pulled out of the poles of the magnet.

5.3 Results and Discussion

Figure 5.5 shows the percentage of MNP captured by a magnetic field of 0.37 Tesla. The graphs were obtained for tubing with diameters of 0.135cm, 0.23cm, and 0.3125cm. As the flow rate increases the percentage of MNP captured decreases in all the three cases. This behavior is attributed to an increasing hydrostatic force. At a lower flow rate, a higher percentage of MNP will be captured by the magnetic field with the remaining particles experiencing sedimentation due to the particle agglomeration and adhesive effects from the inside walls just before the magnetic field. Because of the nanosize nature, the MNP experience negligible gravitational effects, but high viscous drag forces from the moving fluid.

An increase in the flow rate leads to an increase in the hydrodynamic forces which overcome the magnetic attraction. More MNP become dislodged and pulled away from the aggregate by the hydrodynamic forces. It is observed that as the vessel cross section decreases,

the effects of this hydrodynamic forces also increases leading to low MNP capture percentage with increasing flow rate. An increase in the magnetic field from 0.37 T to 0.47 T leads to an increased magnetic force acting on the MNP. The resultant effect is an increased MNP capture as shown in Figure 5.6 when compared with Figure 5.5. The percentage of MNP captured is expected to be higher with increasing magnetic field.

The discrepancy in the maximum MNP build up at the capture site can be attributed to a change in fluid flow characteristics. As the vessel is constricted further by particle aggregation, this constricted region will experience a drop in pressure and increased velocity of the fluid. A critical mass is reached where further particle aggregation is impeded by increased hydrodynamic forces due to the change in fluid flow characteristics.

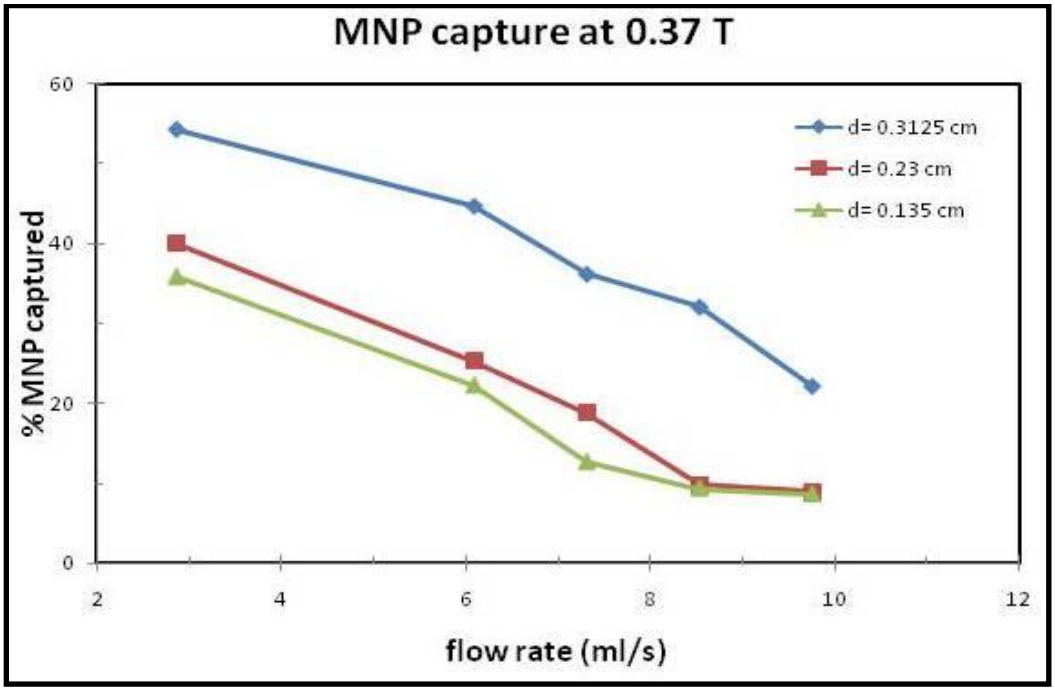

Figure 5.5 Relationship between percentage of MNP captured and fluid flow rate for an applied field of 0.37 Tesla on three vessels of varying diameters.

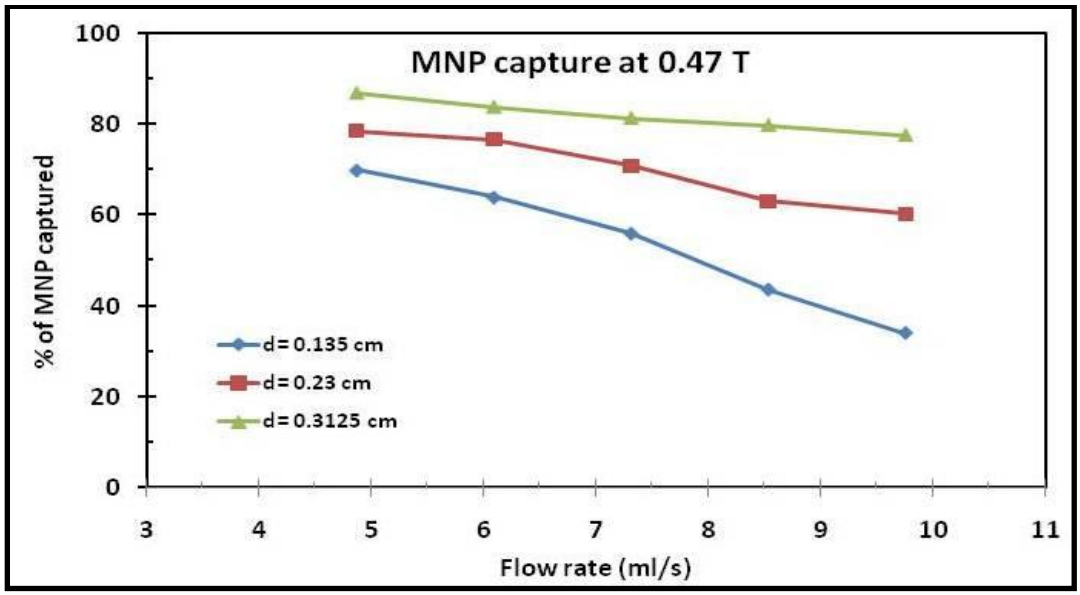

Figure 5.6 Effect of flow rate on the percentage of MNP captured by a magnetic field of 0.47T.

In the next part of the experiment, the MNP were replaced with MNC spheres. The overall capture efficiency of the targeted delivery system decreases. Figures 5.7 and 5.8 show a clear drop in the percentage of MNC captured with decreasing MNP concentration within the spheres. The large deviation in the percentage of capture is explained in the structure of the MNC sphere. The encapsulation of the MNP increases the inter-particle distance between the nanoparticles. The induced magnetic field due to the external magnet will be lower as the magnetic dipole domains separated by the polymer have no way of agglomerating or realigning freely. The net effect is observed as lower MNC capture compared with MNP. The percentage of MNC captured varied in proportion with tube size as shown in Figure 5.7. For instance, at a flow rate of 6ml/s, 39% of MNC were captured by the tube with a diameter 0.4762cm compared to 34% captured by the second tube with diameter 0.3125cm, while the tube with the smallest cross-section had about 20%.

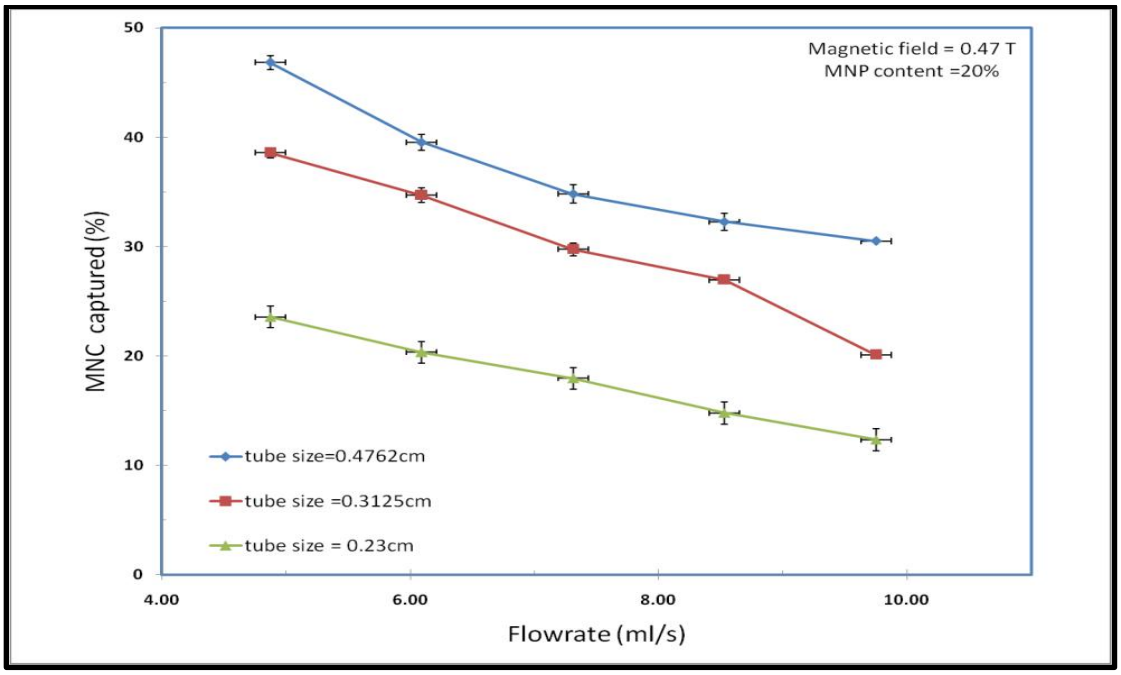

Figure 5.7 Effect of Tube size on the percentage of MNC captured at constant magnetic field and MNP concentration.

Larger vessels facilitate easier fluid flow than smaller vessels at a constant flow rate. When the magnetic field is applied, there is very little room for particle agglomeration inside the tube. Due to the increased fluid flow velocity, the hydrodynamic forces will be dominant. Fewer particles will be captured in the case. To maximize the capturing efficiency, there is a need to consider the concentration of MNP within the MNC spheres.

Figure 5.8 shows the effect of varying the MNP concentrations on the capturing efficiency of the MNC spheres. A MNC sphere with 20% MNP content reveals much higher capture efficiency compared to 15% and 10% MNP. Lesser MNP used in synthesizing the MNC spheres result in a more scattered MNP within the polymer matrix. These decreases the effectiveness of the delivery system observed in Figure 5.8 where a big portion of particles are not captured.

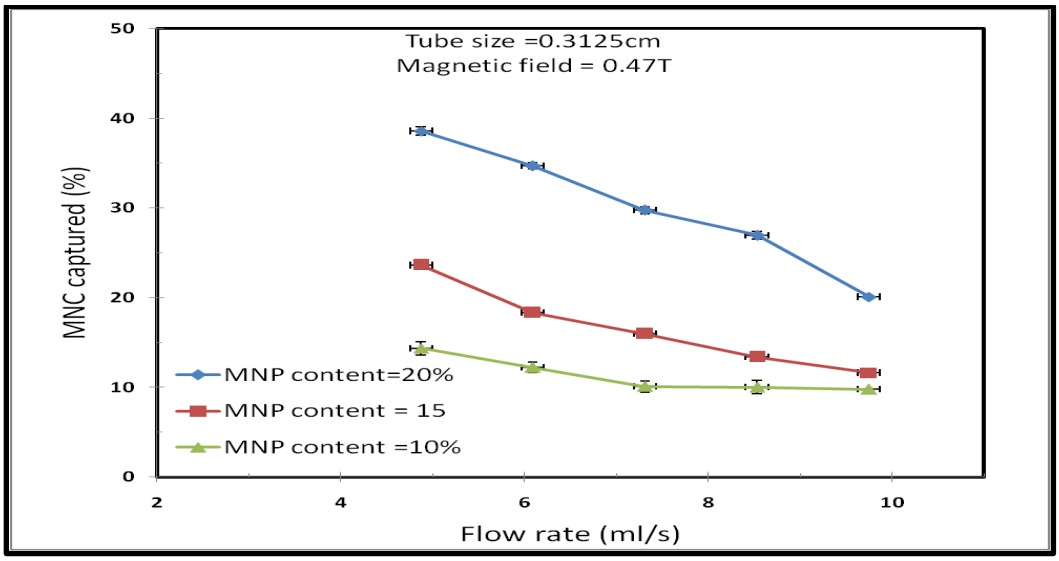

Figure 5.8 Effect of MNP content on the percentage of MNC captured at constant magnetic field and tube size.

5.4 Conclusion

MNP and MNC spheres have been prepared and used to study the efficiency of targeted drug delivery using and external magnetic field. Fluid flow tests were carried out using a magnetic field of 0.37T and 0.47 T. The flow-rate, the vessel diameter and the MNP concentration were varied in the experiments in order to determine the capturing efficiency of the delivery system. The results show that the magnetic field, tube diameter, pump speed and MNP concentrations in the spheres changed the capturing efficiency of the particles and the spheres. These parameters were found to be critical to improve the efficiency of the delivery system. Under similar conditions, the percentage of MNC spheres captured was lower than those of MNP due to polymer particle interactions.

CHAPTER 6

CYTOTOXICITY EVALUATION OF MNC SPHERES

6.1 Introduction

One of the main challenges in selecting a suitable means of drug delivery is that of limiting the systemic toxicity of the drug and carrier material [54, 55]. Drug loaded composite spheres have been developed by many groups for use in-vitro and in-vivo cytotoxicity trials [54-57]. The spheres may be composed of a polymer coating, MNP and a drug of choice. The MNP and polymer materials are selected for their biocompatibility or low toxicity towards the normal cells and organs. The therapeutic agent to be used may have inherent toxicity to both normal and diseased cells.

One of the common drugs used in the treatment of cancer is 5-Fluorouracil (5-FU). 5-FU has high level of toxicity to the normal and diseased cells. Through targeted delivery, this therapeutic agent can be selectively delivered to the diseased organs only by encapsulating it in biodegradable polymer which degrades slowly releasing the drug controlled amounts over a longer period of time [56, 57].

Several studies carried out by in-vitro and animal experiments on the use of encapsulated MNP for targeted drug delivery have been reviewed in Chapter 2. Magnetite has been the MNP of choice in these studies due to its biocompatibility and good magnetic behavior. However, due to major improvements in MNP fabrication mechanisms and encapsulation techniques, new materials that would otherwise not be considered can be used. Magnetic materials such as cobalt,

iron and zinc are known to be essential ingredients for human health. They are recommended by the Food and Nutrition Board at the Institute of Medicine to be part of a normal dietary intake. These materials have good magnetic properties that may be used to improve the process of magnetic targeting.

The purpose of this study is to quantitatively determine the cytotoxicity effects of MNC spheres encapsulated with cobalt zinc ferrite and a drug on cell growth and proliferation. Cobalt zinc ferrite has not been used as a carrier in targeted drug delivery much. In this study, we have therefore selected and fabricated $Co_{0.5}Zn_{0.5}Fe_20_4$ and magnetite by co-precipitation technique. These MNP with a sample drug 5-FU are then encapsulated in PLGA and used for our cytotoxicity trials.

6.2 Experimental

6.2.1 Materials

Magnetic materials

Cobalt zinc ferrite and magnetite nanoparticles were prepared and encapsulated in the biodegradable polymer PLGA. Five types of samples were prepared. Sample A was composed of 20 % by polymer weight of the drug 5-FU and 10% by polymer weight of cobalt zinc ferrite MNP. Sample B was prepared by encapsulating 10% by polymer weight of cobalt zinc ferrite MNP but without 5-FU. Samples C and D were prepared from 5% and 10% magnetite encapsulated in PLGA respectively. As a control, sample E of PLGA alone was also synthesized without the nanoparticles and tested to determine the polymer cytotoxicity. A table of the samples prepared is given in Table 7.

TABLE 7

SAMPLES USED IN CYTOTOXICITY TESTING

Composition of MNC sphere			
Sample name	**Type of MNP**	**% of Drug 5-FU**	**% of PLGA**
A	10% $Co_{0.5}Zn_{0.5}Fe_2O_4$	20%	70%
B	10% $Co_{0.5}Zn_{0.5}Fe_2O_4$	0%	90%
C	5% Fe_3O_4	0%	95%
D	10% Fe_3O_4	0%	90%
E	0%	0%	100%

Reagents

All reagents were obtained from Sigma-Aldrich. This included phosphate buffered saline (PBS), Fasting blood sugar (FBS); Dulbecco's modified Eagle medium (DMEM) and MTT assay.

Drug

5-FU effective in the treatment of cancerous tumors was purchased from Sigma and used without any further modification.

Raw Cells

The raw cells (mouse macrophage) were obtained from ATCC (Cat#TIB-71). Cells were cultured in DMEM medium (ATCC Cat# 30-2002) with 10% FBS (ATCC Cat # 30-2020) at 37^0C in 5% CO_2 in air atmosphere. The cells were grown in a 96 wells plate at 5000

cells/well/100 µl. The plates were then kept in an incubator overnight to let cells adhere to the plate. The next day 100 µl MNP (10mg/ml) was added into the first well and mixed with 100 µl of medium, and then 100 µl of the mixture was transferred into second well, using the 1:2 dilution ratio. The particle amount per well is 500 µg, 250µg, 125µg, etc. in that sequence as shown in Table 7. We also included some wells with the same number of cells, but without any particle for a negative control. The plates were then placed in an incubator at 37^0C to allow the cells to proliferate.

TABLE 8

WELLS CONTAINING DIFFERENT AMOUNTS (µg) OF THE MNP

Sample A	500	250	125	62.5	31.3	15.6	7.8	3.9	2.0	1.0	0.5	0.25
Sample B	500	250	125	62.5	31.3	15.6	7.8	3.9	2.0	1.0	0.5	0.25
Control	500	250	125	62.5	31.3	15.6	7.8	3.9	2.0	1.0	0.5	0.25
medium	0	0	0	0	0	0	0	0	0	0	0	0

6.2.2 Cell Growth

The MTT based cytotoxicity tests were carried out to determine the effect of the drug, MNP and polymer on the prepared cell lines. After 3, 4, 5 and 6 day's culture, the cell lines were removed from the incubator and 20µl of MTT added to each well. The cell plates were then kept for 6 hours before the addition of 10% SDS. The cell lines were then placed in the incubator at

37^0 C and allowed to stay overnight. The mitochondrial activity of the cultured supernatant was then measured to determine the absorbance using a spectrofluorometer at a wavelength of 590 nm.

The cell viability was determined by calculating the fraction of viable cell relative to the control cells. This process was repeated three times to ensure experimental. The absorbance data from each of the cell lines was collected and average values determined. The absorbance (OD 590nm reading) represented as mean ± standard deviation was plotted as a function of the particle amount (μg/well).

6.3 Results and Discussion

Samples of MNC spheres with and without a cancer dug were prepared and used to determine the proliferation of tumor cells in a period of three to six days. A control group of raw cells placed in a medium was also used in the trials to provide a baseline for a comparison. Samples from each group were observed under a microscope and recorded as shown in Appendix 2

6.3.1 Cell Growth in Medium Results

The first test involved placing the raw cell in the medium. The cell count for these cells was obtained on the first, third and fourth day. The amount of viable cells was determined from the microscope images. Figure 6.1 is a microscope image of cells obtained from a well containing 20 μl of medium on day 3. The cells are observed to have a regular shape and size with no noticeable deformation or cell death on day 3. A cell count obtained for the test period was plotted in Figure 6.2. From the graph, high cell viability is observed on day 3 and increases for the two consecutive days in all the wells used.

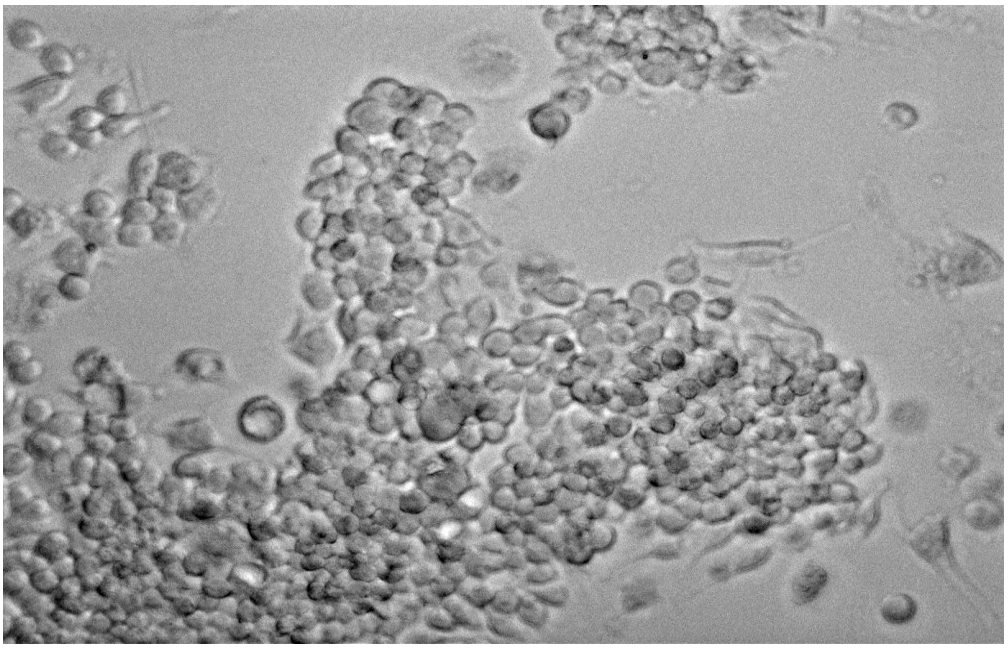

Figure 6.1 Microscope images of raw cells on day 3

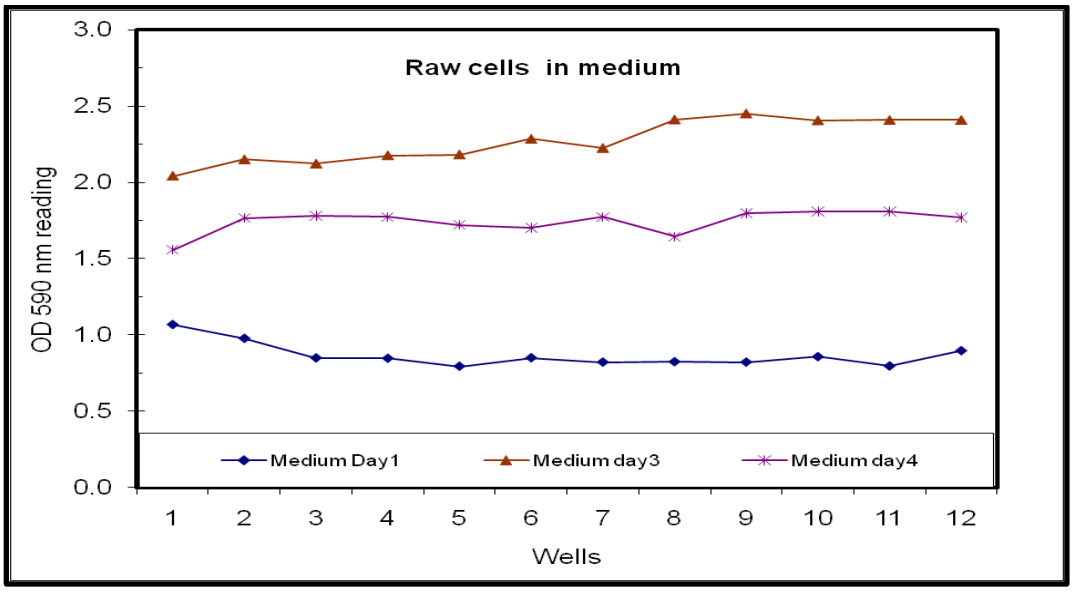

Figure 6.2 Cell viability in a cell line containing the medium during the 1st, 3rd, and 4th day.

These results were useful as they served as a baseline for further testing. From the results the expected cell growth rate was identified and used to compare with other cell lines containing different samples.

6.3.2. Drug Cytotoxicity Results

In the second cytotoxicity testing, different amounts of the drug 5-FU were added to the wells containing equal number of cells in 200µl of the medium. A significant drop in cell viability occurs and is consistent with the 4 day as shown in Figure 6.3. The normal rate of cell proliferation would be similar to the graph of the medium on day 4. The OD reading for 5-FU samples remain below 0.5 while that of the medium is as high as 1.7. There is no significant change in cell viability even when the drug concentration is increased in the sample from 0.24µg to 500 µg. These results indicate that the level of toxicity in 5-Fu is high and causes cell death regardless of the concentration or length of exposure.

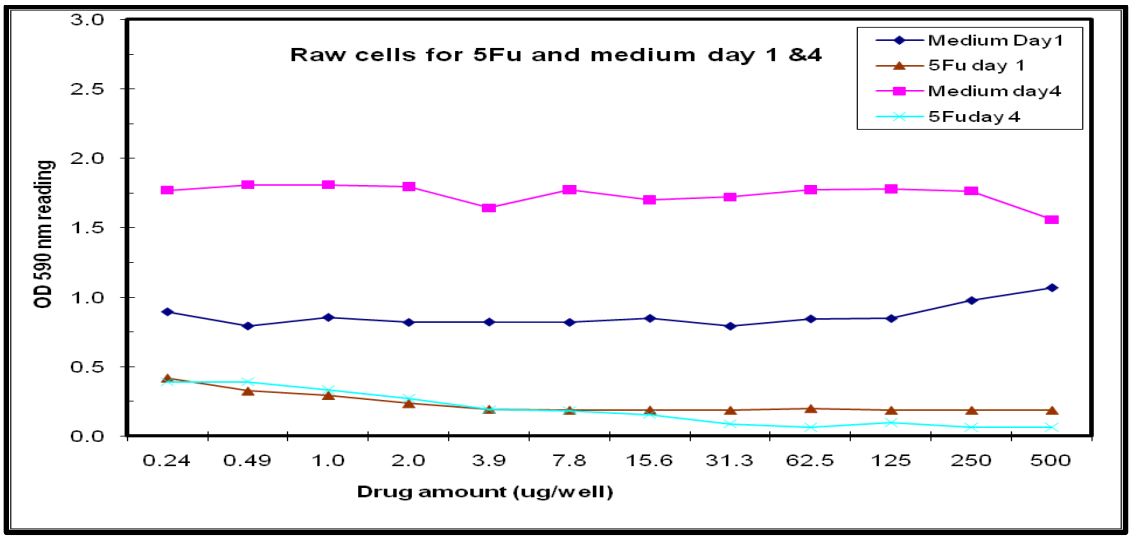

Figure 6.3 Cell proliferations in wells containing different amounts of the drug 5-FU.

6.3.3 Nanocomposite Cytotoxicity Results

In the third experiment, sample A was made by encapsulating both the drug 5-FU and the MNP of cobalt zinc ferrite in PLGA. This sample was added to the raw cells. The Microscope image of sample (A) shown in Figure 6.4 has a very low cell count when compared with the cell count in Figure 6.1 which is the medium. The differences in cell proliferation may be attributed to cell death due to the presence of the drug and MNP in the MNC sphere. This is well illustrated in Figure 6.5 where the cell viability of the samples was compared to those of the medium.

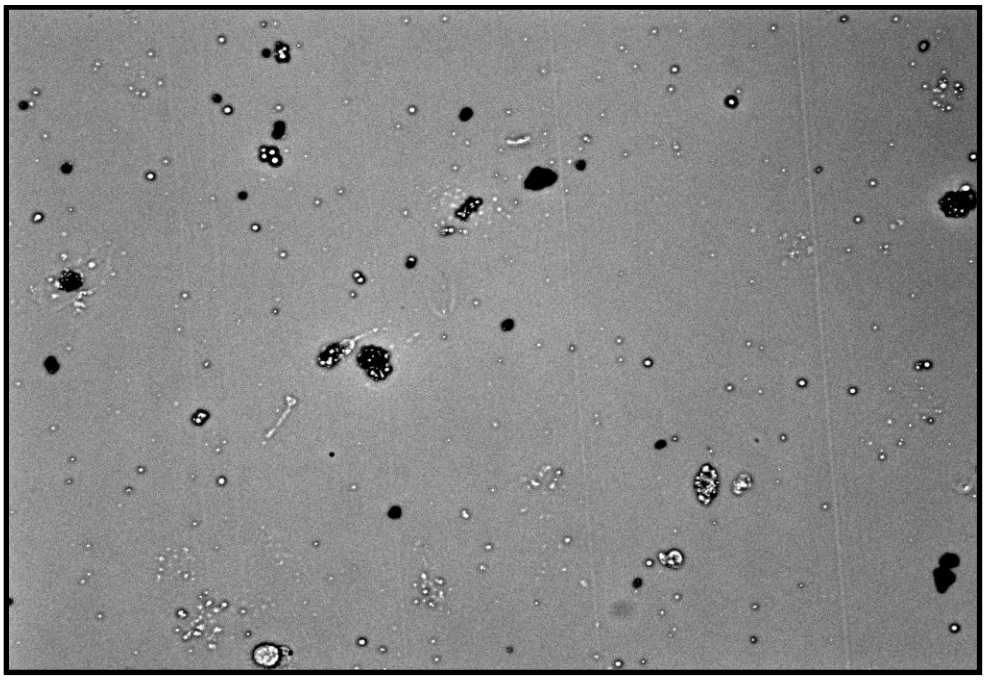

Figure 6.4 Microscope images of raw cells containing sample (A) on day 6.

Graphs of sample (A) and the medium obtained on day 3 and day 6 are shown in Figure 6.5. A comparison of the two graphs reveals a very low cell count on both days for cells exposed to sample (A). The medium in the two samples is used as a control parameter. On day 3 the average number of viable cells in the medium is 0.88 ± 0.1. This value increases on day six to

2.31 ± 0.2. The number of viable cells in the well containing Sample (A) is below 0.25 at low and high concentrations with no noticeable change in cell viability suggesting cell death. The absence of cell viability on 6 days of exposure to sample (A) indicates that this sample is toxic to the raw cells and is responsible for the cell death. Since the spheres in Sample (A) are composed to PLGA, 5-FU and the MNP, any of these ingredients could be responsible for cell death.

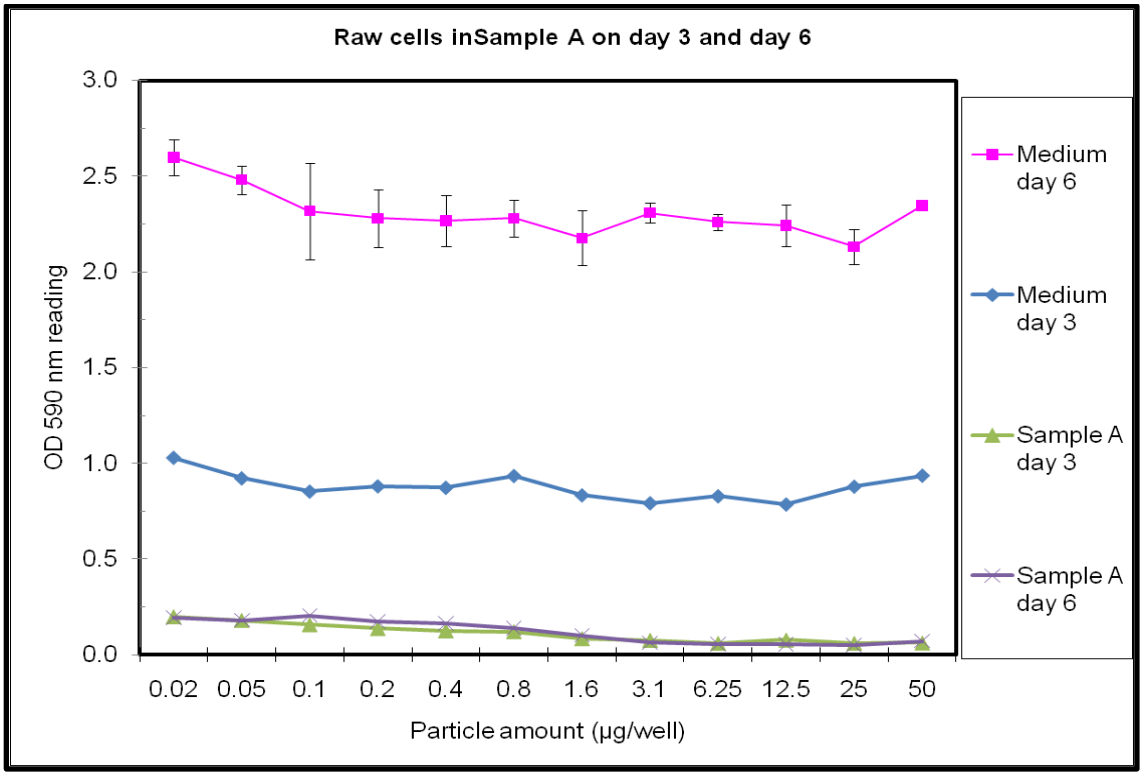

Figure 6.5 Cellular uptakes of drug carrying MNC spheres (sample A) on day 3 and 6.

Earlier investigation with the drug 5-FU shown in Figure 6.3 had shown no cell viability. This suggests the need to investigate whether the PLGA or the MNP are responsible for the current trend. Further investigations on the effects of the MNC spheres alone on cell viability were carried out.

6.3.4 MNC with Cobalt Zinc Ferrite Cytotoxicity Results

In the fourth experiment, sample B was prepared by encapsulating the MNP of cobalt zinc ferrite without the drug into PLGA. The microscope images in Figures 6.6 and 6.7 show cell proliferation in two wells containing 5µl of sample B on day 3 and day 6. Sample B was prepared to act as a carrier for the therapeutic agent.

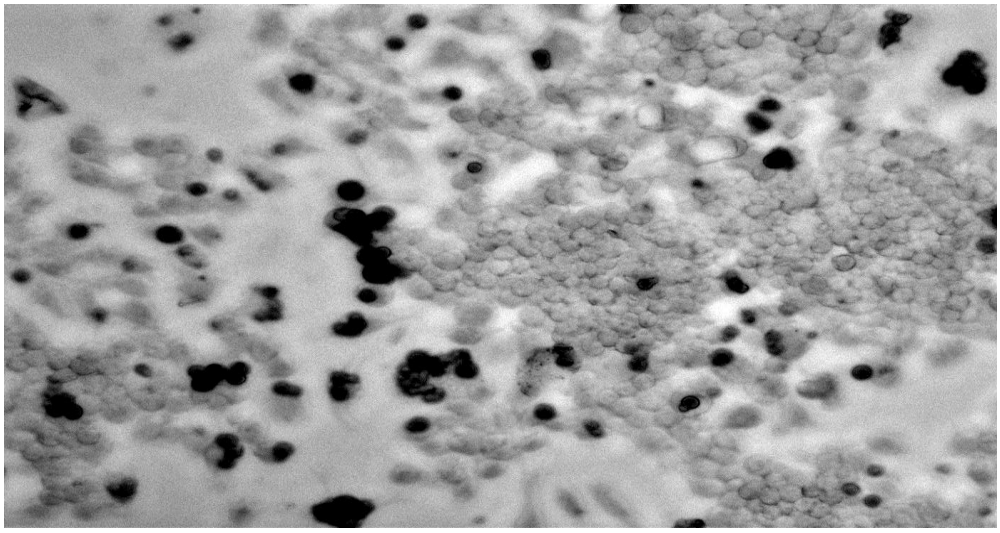

Figure 6.6 Microscope image of cells dispersed in 5 µl of sample (B) on day 3.

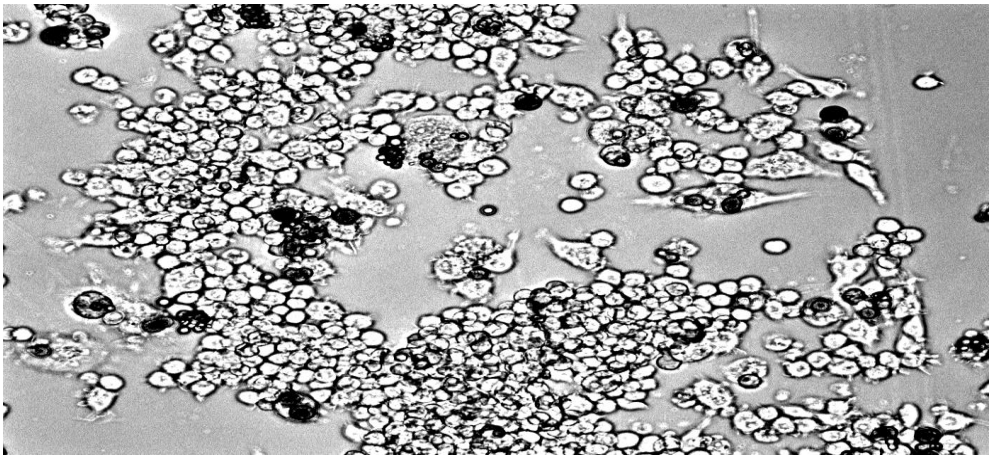

Figure 6.7 Microscope image of cells dispersed in 5 µl of sample (B) on day 6

For this sample to be effective as a carrier, it should have low toxicity towards normal cells. From the images we deduce that after 3 days of exposure to MNC sphere without the drug, the cell viability is still high. On day 6, most of the cells died as shown in the Figure 6.7.

The graphs in Figures 6.8 and 6.9 show cells dispersed in sample B and the medium on day 3 and day 6, respectively. An analysis of Graphs in Figure 6.8 shows very low cell viability at high concentrations of sample B, but when the amount of the sample is decreased to below 60μg/well, the cell viability increases, which is an indicative of a dose dependent cell growth inhibition, suggesting direct cytotoxicity. At lower concentrations, the cell viability for this sample behaves as that of the medium within the margin of an error. These results are significant as they suggest that cobalt zinc ferrite has the potential to be optimized for use as a drug carrier within concentrations that have little impact on cell viability. The change observed in cell viability with particle amounts below 62.5μg/well is indicative of the tolerance level of the cells to the presence of the sample B.

Further tests were carried out to investigate the possible reasons for the low viability at high concentrations. Our hypothesis was that this low viability is partly due to the process parameters in the synthesis of the MNC spheres. There was a possibility of residual particles and solvents within the polymer matrix that led to this cell death. In order to test this, the polymer PLGA was synthesized using the oil-in-oil emulsion solvent method without the MNP and the drug. The results are given in the following section.

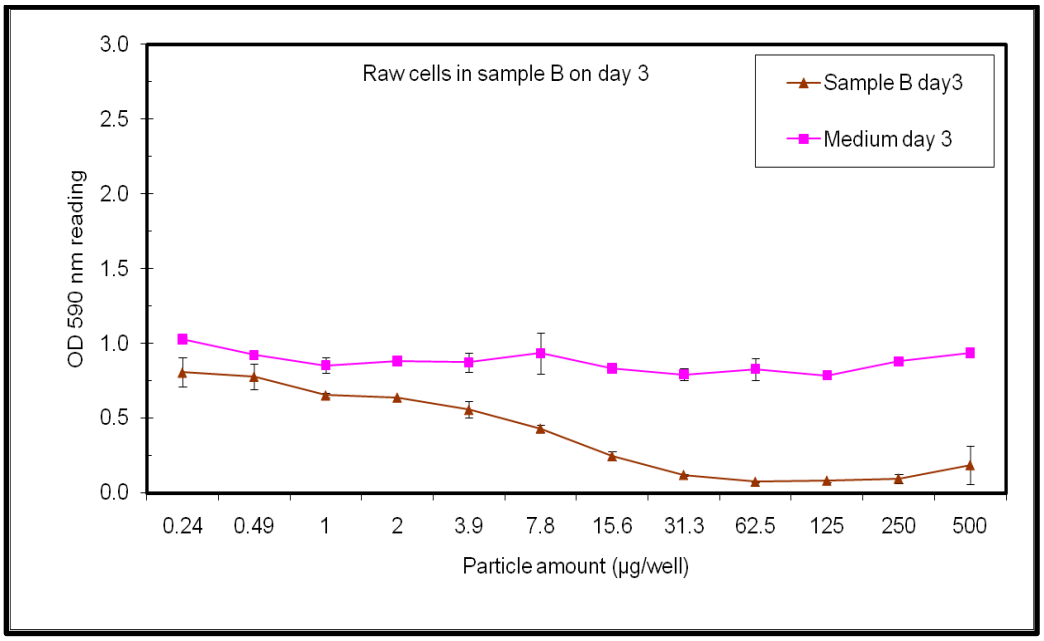

Figure 6.8 The cell viability on Sample B and the medium on day 3

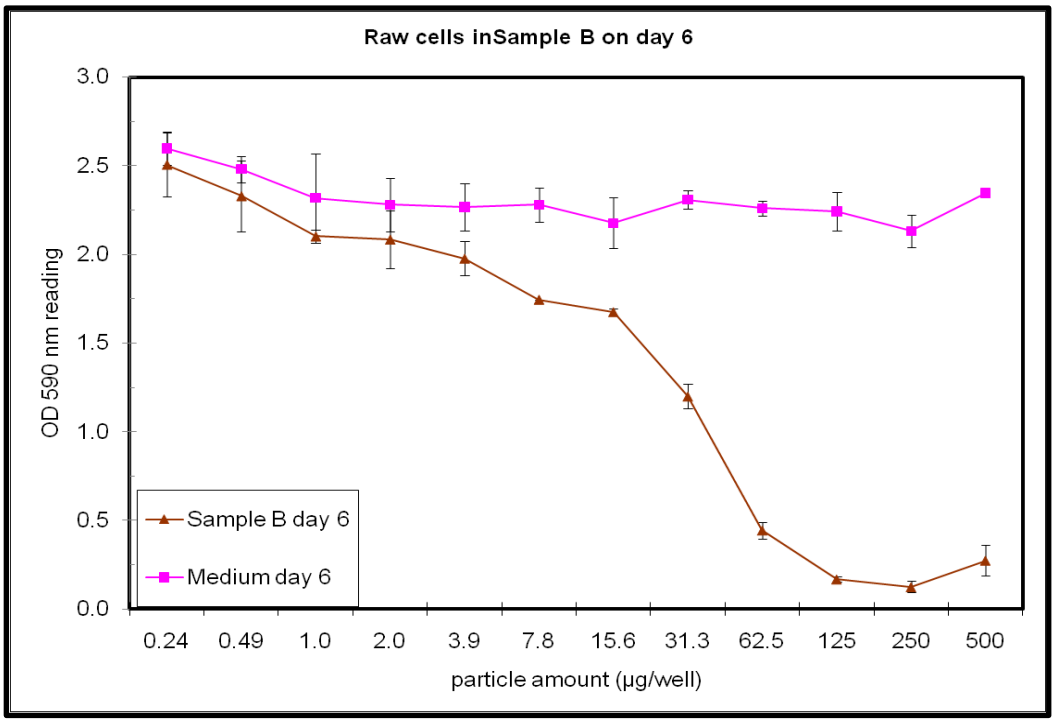

Figure 6.9 Cell viability in Sample B and the medium on day 6

6.35 Polymer Cytotoxicity Results

Sample E was prepared by synthesizing the polymer PLGA alone with co-precipitation. The sample was tested for cytotoxicity. From the data collected, the graphs were obtained and plotted in Figure 6.10. The graphs suggest that a higher amount of PLGA promotes slightly lower cell proliferation in the sample. Cell viability increases from day 3 to day 6 in amounts lower than 15µg/well. This is closer to the medium. The mean OD 590nm reading on all the sample of the medium is 1.76 ± 0.14 compared to a value of 1.2 ± 0.24 for PLGA on day 3 and 1.4 ±0.40 for PLGA on day 6. The difference in mean readings is small, suggesting the presence of impurities which may affect the overall purity of the samples. Possible sources of impurities could be residual solvents in the sample that are held inside the polymer matrix.

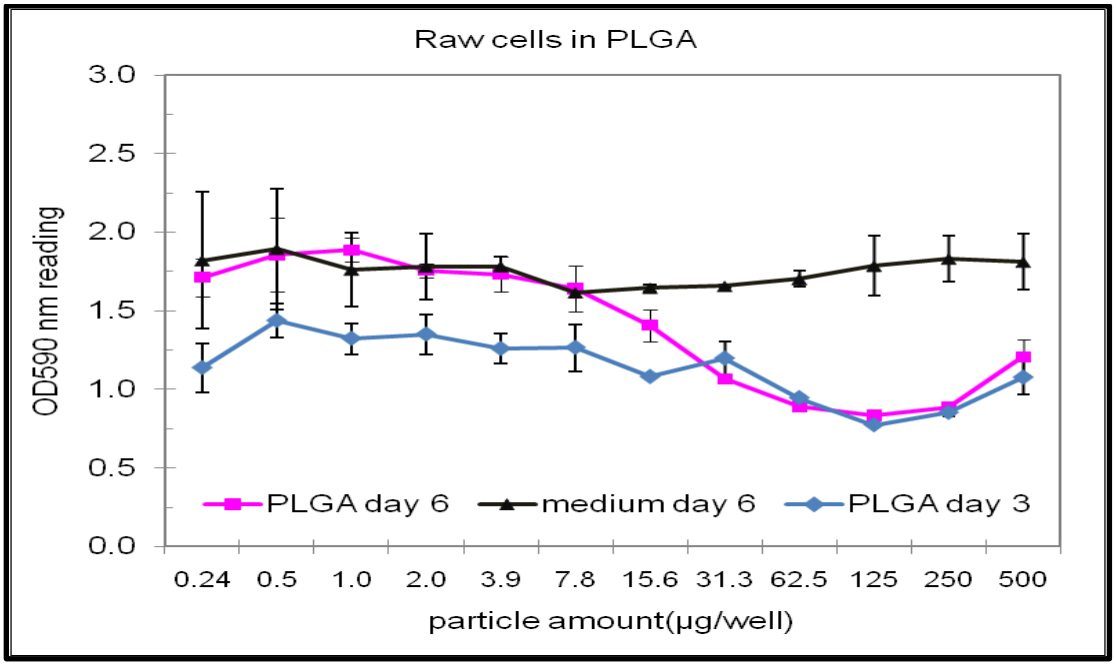

Figure 6.10 Cytotoxicity analysis of PLGA polymer synthesized by emulsion solvent evaporation in the absence of MNP and drug.

6.3.6 MNC with Magnetite Cytotoxicity Results

Further analysis on the effect of MNP on the cell proliferation was carried out using magnetite loaded MNC spheres. Sample C was prepared with a MNP content of 5% while sample D had a MNP content of 10% of the polymer weight. These samples were then dispersed in 200µl of medium containing the raw cells at different concentrations per well.

Figure 6.11 shows the fraction of viable cells in a sample of PLGA loaded with 5% and 10% of magnetite for three days. The average fraction is about 0.46±0.05 in the 5% sample and 0.43±0.03 in the 10% sample. These average fractions are the same within the margin of an error. These values are below the expected cell viability when compared with the medium.

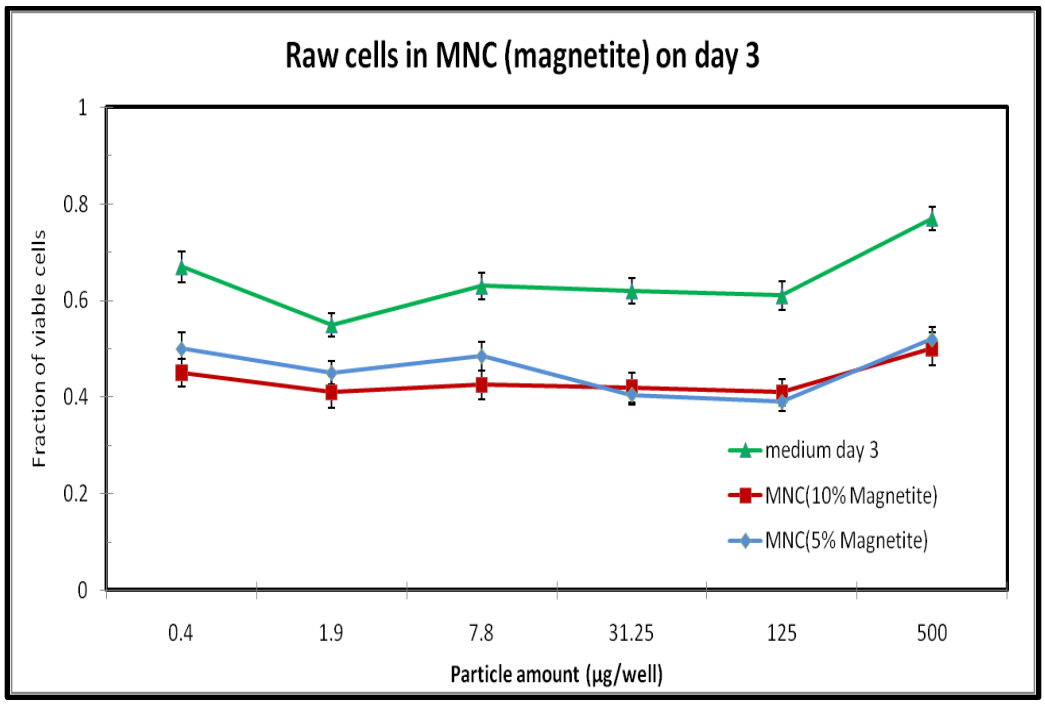

Figure 6.11 Cell viability in magnetite loaded MNC spheres after 3 days.

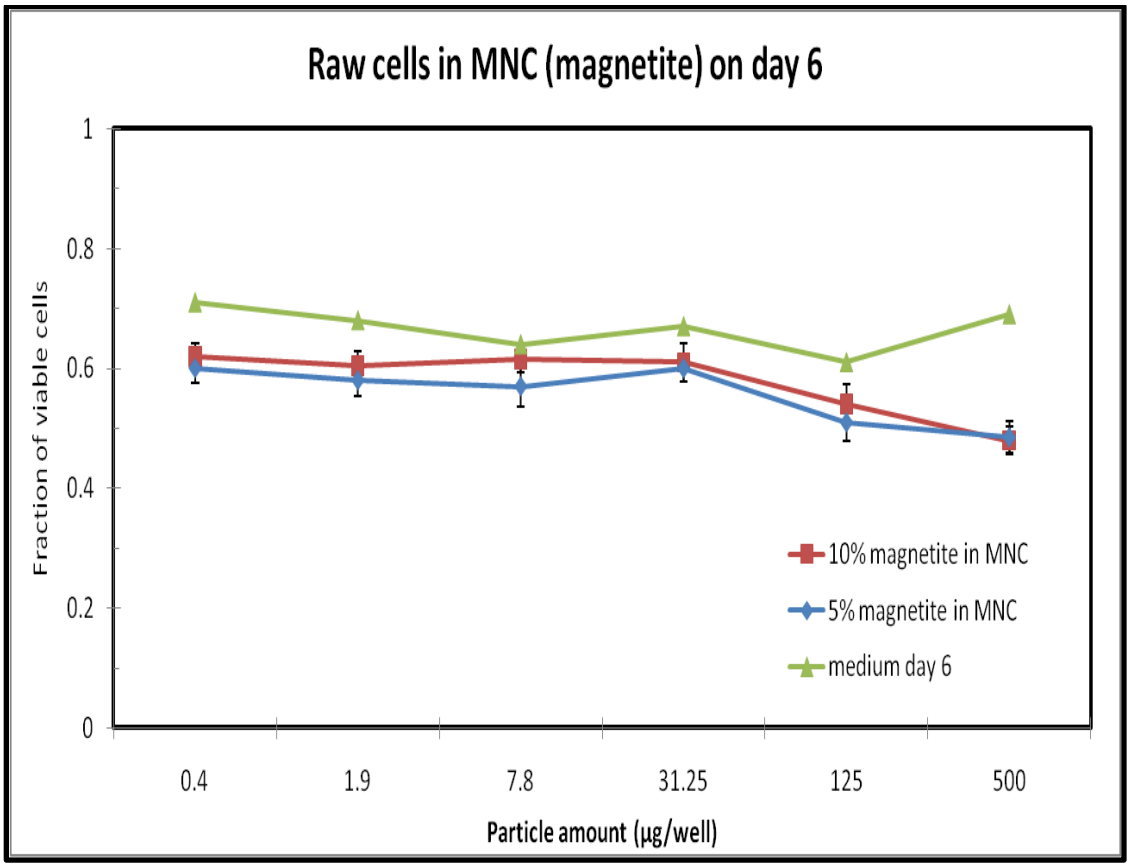

Figure 6.12 Cell viability in magnetite loaded MNC spheres on day 6.

In Figure 6.12, the trend in cell viability is constant with a change in particle amount in the well. The average fraction of viable cells is found to be closer to that of the medium, indicating a less toxicity in the MNC samples containing magnetite regardless of the sample concentration of particle content.

6.4 Conclusion

Cytotoxicity studies were carried out on MNC encapsulated with cobalt zinc ferrite or magnetite, the drug 5-FU and the polymer PLGA. These particles were tested to determine the effect of the sample concentration, percentage of MNP encapsulation and exposure time on the

cell viability. Cytotoxicity tests on MNC spheres prepared reveal a high toxicity in large concentration of cobalt zinc ferrite which reduces as the concentration is decreased.

The results show the constant cell viability in samples of magnetite regardless of the sample concentration or a percentage of the MNP encapsulated. The results also indicate a higher level toxicity present in cobalt zinc ferrite than in magnetite at higher concentrations. Cobalt zinc ferrite has improved cell viability at lower sample concentrations. The test results suggest that at low concentrations, cobalt zinc show promising properties that could be utilized in magnetic targeted delivery. An analysis of polymer cytotoxicity revealed the residual effect of the synthesis process could be contributing to the toxic effect of the samples on cells.

CHAPTER 7

CONCLUSION AND RECOMMENDATIONS

7.1 Conclusion

Magnetic drug targeting is an adaptable drug delivery technique which uses science of nanotechnology to improve the mode of delivery of the therapeutic agents to the body. The main principle behind drug targeting involves the use of MNP and MNC spheres as magnetic carriers of the bioactive agent of the choice to a specific target site. The overall benefits include increased efficiency of the therapeutic agent, minimal loss of bioactive agent and reduced side effects to the body.

Cobalt zinc ferrite in optimized stoichometric ratios was selected and prepared by co-precipitation method. Magnetite was also prepared and used as a standard of comparison. These MNP and the therapeutic agent were encapsulated in a biodegradable polymer PLGA by oil-in-oil emulsion solvent evaporation. The MNP prepared were then characterized by a number of techniques, including SEM, TEM, DLLS, XRD, VSM and SQUID.

To explore the morphology and composition of the MNP, we used SEM and XRD. The MNP were found to have a uniform size distribution and morphology with no agglomeration. Co-precipitation method provided a simple way of synthesis of nanoparticles and provided control over the process of nucleation and growth and therefore the properties of the resulting MNP. Structural characterizations of cobalt zinc ferrite using XRD was found to match with a single phase of cubic spinel cobalt zinc ferrite. The samples showed no evidence of separate

phases or process contamination from XRD pattern the size of the particles was calculated using Scherrer's equation and found to be close to 10nm.

TEM analysis exposed a well crystallized MNP with a wide size distribution diameter. The morphology of the MNC spheres produced by oil-in-oil emulsion/solvent evaporation method was also affected by the concentration of MNP in the sample. The DLLS and SEM analysis proved that the MNC spheres had sizes ranging from 800 nm to 1. μM. The results from DLLS showed that the size of the MNC spheres increased in a good correlation with the MNP content. To test the process parameters used in the preparation of the MNP, we used Mossbauer spectroscopy. The samples we prepared in the lab were compared to the known spectra of pure samples. Our samples of magnetite were found to match the known spectra of magnetite thus confirming the quality of our fabrication process.

In order to understand the effect of MNP concentration on the magnetic properties of the nanocomposite sphere, we prepared MNC spheres with varying MNP concentrations. The MNP content in the sphere matrix was increased in the ratios 10%, 15% and 20% in polymers. The resultant product was analyzed using a SQUID magnetometer. The ZFC and FC magnetization measurements were obtained at a temperature range from 0 K to 300 K under a constant applied field of 1000 Oe. The results of this analysis revealed an increase in magnetization with increasing MNP content which was consistent with expected behavior of MNP. Magnetite was found to have T_B in the range of 40K to 80K while cobalt zinc ferrite had T_B between 120K and 140 K suggesting both materials were superparamagnetic at temperatures near room temperature.

Further analysis of the data from the magnetic hysteresis obtained at 300K revealed an increasing magnetic saturation as a function of loading attributed to increased magnetic moments

per unit volume. This analysis was done for both Fe_3O_4 and $Co_{0.5}Zn_{0.5}Fe_2O_4$ nanoparticles. At 20% MNP loading, magnetite had a saturation magnetization of 4.3 (emu/g), while $Co_{0.5}Zn_{0.5}Fe_2O_4$ had 2.6 (emu/g). This had a direct effect on the strength of the magnetic dipole moments in the applied field both materials in the nanocomposite spheres were found to retain their super paramagnetic properties even after encapsulation and dispersal in the biodegradable polymer.

Fluid flow experiments were carried out to study the effect of encapsulation of MNP on the flow profile within vessels of different cross-sections in the presence of a magnetic field. MNP and MNC spheres were made to flow at different flow rates in tubes of varying diameter under a constant magnetic field. The results showed the tendency of MNP and spheres to settle within the vessels with larger diameter and reducing the percentage of nanoparticles passing through the magnetic field. Drag forces were observed to increase in proportion with the reduction in size of the vessels due to higher fluid nanoparticles speeds. A decrease in the strength of the magnetic field caused a subsequent drop in the percentage of the MNP captured suggesting that appropriate magnetic fields strengths were needed to ensure efficient magnetic capture. Further comparison of capture efficiency using MNP and MNC spheres showed that encapsulating MNP decreased their dipole to dipole interaction due the polymer coating and made it easy for the Hydrodynamic forces to dislodge the captured particles.

Further analysis on the fluid flow process was done using computational fluid dynamics. The aim of this work was to study the fluid flow phenomena at the region of capture. Three cross-sections were selected and magnetic capture characteristics modeled using CFD software (*Fluent*). The effect vessel constriction on fluid flow profile was examined. CFD results (see Appendix) revealed a change in flow properties with increasing constriction that may have an

influence on the hemodynamic flow properties. Due to low pressure and increased velocity at the region of capture the laminar flow profile turns turbulent due to the formation of eddy currents just after the constriction. This behavior may have a direct influence on particle retention at the region of capture. This suggests the possibility of increased hydrodynamic forces which may overcome the magnetic forces leading to particles dislodging at the periphery of the constriction. This study is ongoing and part of the results is available in Appendix 5.

Cytotoxicity results showed that the cell viability in any sample was strongly influenced by the toxicity of the sample. Studies on cell dispersion in the medium showed good cell growth and proliferation and served as our standard for comparison with other samples. 5-FU, the drug of choice in our investigation was found to be very toxic and led to cell death over the entire length of exposure. When the drug was encapsulated in the MNC sphere, similar results were obtained. This was found to be significant since in targeted delivery the diseased cells would be killed when exposed to the drug carrier.

To investigate the MNC sphere cytotoxicity, samples without the drug were tested and showed improved cell viability at lower concentrations for cells kept over a period of three to six days. These samples contained $Co_{0.5}Zn_{0.5}Fe_2O_4$ nanoparticles. A comparison of magnetite and $Co_{0.5}Zn_{0.5}Fe_2O_4$ toxicity provided strong evidence that these MNP could be tailored for use in drug delivery by optimizing their concentration at regions that would allow the normal cells to proliferate. Higher concentrations were found to be toxic as fewer cells were able to thrive. There was a need to review the MNC synthesis process in order to reduce solvent toxicity in the sample.

7.2 Recommendation

The process of encapsulation of MNP in a polymer has the desirable effect of improving magnetic targeting and delivery of therapeutic agent with minimal side effect. This study confirmed that magnetic drug targeting could be achieved by tailoring the MNP to achieve MNC spheres that would serve as carriers of therapeutic agents. This study also revealed that the magnetic properties of the final MNC sphere will be affected by the type of coating used. Testing with a variety of coating needs to be carried out to select suitable coatings that would not provide a dielectric barrier to the magnetic field.

Work has been done by other groups in trying to determine the feasibility of embedding a magnetic field near the tumor or fabricating stents from magnetic materials that can increase the magnetic field around a target region. Further studies will be done on the use of naturally occurring polymers like chitosan and cellulose to compare the encapsulation efficiency of such polymers with PLGA. The magnetic properties of the MNC sphere will be closely reviewed to identify how MNP dispersal within the matrix affects the strength and magnetic properties on various MNC spheres.

The current research was extended to fluid flow modeling using a CFD method. Details of this work are available in Appendix 5. Future work will also involve completion of this part of the research. Preliminary results show the fluid flow profile at the region of capture is influenced by the size of the constriction and flow rate. The changing flow profile and its effect on the magnetic particle capture and retention will be addressed.

REFERENCES

References

[1] Arruebo, M., Pacheco, R. F., Ibarra, M. R., and Santamaria, J., –Magnetic Nanoparticles for Drug Delivery," *Nanotoday*, June 2007, Vol. 2. No. 3, pp. 22-32.

[2] Cancer Facts and figures 2009, URL: http://www.cancer.org/downloads/STT/Global [cited March 2010].

[3] Laura, G., Pedraza, F.," Mechanisms of Oncogenic Cooperation in Cancer Initiations and Metastasis," *Yale J Biol Med.2006*, Vol. 79, issue. 3-4, pp. 95-103

[4] Jain, K. K., –Targeted Drug delivery for Cancer", *Technol in Cancer Res and Treatment*, 2005, Vol. 4, No. 4, pp. 311-313.

[5] Lubbe, A. S., Alexiou, C., and Bergemann, C. –Clinical Application of Magnetic Drug Delivery," *J. Surg. Res.*, Vol 95, 2001, pp. 200-206.

[6] Lubbe, A. S., Bergemann, C., Brock, J., and McClure, D.G. –Physiological Aspects in Magnetic Drug-Targeting," *J. Magn. Magn. Mater.* Vol. 194, 1999, pp. 149-155.

[7] Rudge, S. R., Kurtz, T. L., Vessely, C. R., Catterall, L. G., and Williamson, D. L. –Preparation, Characterization, and Performance of Magnetic Iron-Carbon Composite Microparticles for Chemotherapy," *Biomaterials*, Vol. 21, 2000, pp. 1411-1420.

[8] Leach, J.H. –Magnetic Targeted Drug Delivery," *M.Sc. Thesis, Department of Electrical Engineering*, Virginia Tech, 2002.

[9] Harris, L.A. –Polymer Stabilized Magnetite Nanoparticles and Poly (propylene Oxide) Modified Styrene-Dimethacrylate Networks," *Ph.D. Dissertation, Department of Chemistry*, Virginia Tech, 2002.

[10] Lopera, S.A.G., Plaza, R.C., and Delgado, A.V. –Synthesis and Characterization of Spherical Magnetite/Biodegradable Polymer Composite Particles," *J. Colloid and Interface Sci*., Vol. 240, 2001, pp. 40-47.

[11] Asmatulu, R., Zalich, M.A., Claus, R.O., and Riffle, J. –Synthesis, Characterization and Targeting of Biodegradable Magnetic Nanocomposite Particles by External Magnetic Fields," *J. Mag. and Mag. Mater*., Vol. 292C, 2005, pp. 108-119.

[12] Asmatulu, R. –Biomaterials—*Class Notes*," Wichita State University, fall 2008.

[13] Asmatulu, R., Fakhari, A., Wamocha, H.L, Chu, H.Y., Chen, Y.Y., El-Tabey M.E., Hamdeh, H.H. and Ho, J.C. –Synthesizing Drug-Carrying Magnetic Nanocomposite

Particles for Targeted Drug Delivery." *Journal of Nanotechnology*, Vol. 2009 (2009), Article ID 238536, 6 pages,

[14] O'Brien, C. N., and Guidry, A. J. "Formulation of Poly (D, L-lactide-co-glycolide) Microspheres and Their Ingestion by Bovine Leukocytes," *J. Dairy Sci*. Vol. 79, 1996, pp. 1954-1959.

[15] Lima, K. M., and Rodrigues, J. M. "Poly (D, L-lactide-co-glycolide) Microspheres as a Controlled Release Antigen Delivery System," Braz. *J. Med. and Bio. Res.,* Vol. 32, 1999, pp.171-180.

[16] Lee, S. J., Jeong, J. R., Shin, S. C., Kim, J. C., Chang, Y. H., and Kim, J. D. "Nanoparticles of Magnetic Ferric Oxides Encapsulated with Poly(D,L-lactide-co-glycolide) and Their Applications to Magnetic Resonance Imaging Contrast Agent," *J. Magn. Magn. Mater.* 2004, pp. 2432-2433.

[17] Emami, J., "Particle Size Design of PLGA Microspheres for Potential Pulmonary Drug Delivery Using Response Surface Methodology," *J. Microencapsulation,* Vol. 99999 No.1, 2008, pp. 1-8.

[18] Kim, B. K., Hwang, J., Parks, J. B., Parks, H. J. "Preparation and Characterization of Drug Loaded Polymethacrylate Microspheres by Emulsion Solvent Evaporation Method," *J. Microencapsulation*, Vol. 19, 2002, pp. 811-822.

[19] Asmatulu, R., Fakhari, A., Wamocha, H.L, Hamdeh, H.H. and Ho, J.C. "Fabrication of Magnetic Nanocomposite Spheres for Targeted Drug Delivery," *2008 ASME International Mechanical Engineering Congress and Exposition*, November 2-7, Boston, pp. 1-4.

[20] Santovena, A., Garcia, J.T., Oliva, A., Llabres, M., and Farina, J.B. "A Mathematical Model for Interpreting In- Vivo rhGH Release from Laminar Implants," *Int. J. Pharm.,* Vol. 309, 2006, pp. 38-43.

[21] Santovena, A., Alvarez-Lorenzo, C., Concheiro, A., Llabres, M., and Farina, J.B. "Rheological Properties of PLGA Film-Based Implants: Correlation with Polymer Degradation and SPf66 Antimalaric Synthetic Peptide Release," *Biomaterials* Vol. 25, 2004, pp. 925–931.

[22] Glynn, P.A.R., van der Hoff, B.M.E., and Reilly, P.M. "A General Model for Prediction of Molecular Weight Distributions of Degraded Polymers**,** Development and Comparison with Ultrasonic Degradation Experiments," *J. Macromol. Sci. Chem*., Vol. A, No. 6, 1976, pp. 1653-1664.

[23] Buschow, K. H. J. *Handbook of Magnetic Materials*, vol. 16, Elsevier, 2006.

[24] Hamdeh, H. H., Al-Ghanem, H., Folkerts, T. J., Eltabey, M. M., Ho, J. C., and Willey, R. J. ―Temperature Dependent Lattice Distortion in Aerogel-Produced Fe-Mo Oxides," J. *Appl. Phys. Letters,* Vol. 92, 2008.

[25] Asmatulu, R., Claus, R.O., Riffle, J. S., and Zalich, M. ―Targeting Magnetic Nanoparticles in High Magnetic Fields for Drug Delivery Purposes," *Mat. Res. Soc. Symp. Proc.* Vol. 820, 2004, pp. O3.8.1- O3.8.6.

[26] Gogotsi, Y. ―Nanomaterials Handbook," CRC Press, 2006.

[27] Sun, C.; Lee, J. H. C, and Miqin, Z. ―Magnetic Nanoparticles in MR Imaging and Drug Delivery". *Advanced Drug Delivery Revs,* Vol. 60, 2008, pp. 1252-1265

[28] Rotariu, O, Strachan, N. J. C., ―Modeling Magnetic Carrier Particle Targeting in the Tumor Microvasculature for Cancer Treatment". *J. Magn. Magn. Mater,* Vol. 293, 2005, pp. 639-646

[29] Vlerken, L. E., Amiji, M. M., ―Multifunctional Polymeric Nanoparticles for Tumour-targeted Drug Delivery."*Expert Opin. Drug Deliv*, 2006, Vol. 3, No. 2.

[30] Sun, C., Lee, J.S., and Zhang, M., ―Magnetic Nanoparticles in MR Imaging and Drug Delivery*", Advanced Drug Delivery Reviews*, 2008, vol. 60, No. 11, pp. 1252-1265.

[31] Suzuki, H., Lee, I.Y., Maeda, N., ―Laser Induced Emission from Dye-Doped Nanoparticle Aggregates of Poly(DL-lactide-co- glycolide)"International Journal of Physical Sciences, 2008, Vol. 3, No. 1, pp. 042-044,

[32] Cheng, J., Teply, B. A., Sherifi, I., Sung, J., Luther, G., Gu, F. X., Nissenbaum, E. L., Moreno, A. F. R., Langer, R., Farokhzad, O. C., *"*Formulation of functionalized PLGA-PEG nanoparticles for in vivo targeted drug delivery*"*, *Biomaterials,* Vol. 28, 2007, pp. 869-876.

[33] Li, L., Chen, D., Zhang, Y., Deng, Z., Ren, X., Meng, X., Tang, F., Ren, J., Zhang, L., ―Magnetic and Fluorescent Multifunctional Chitosan Nanoparticles as Smart Drug Delivery System". *Nanotechnology,* Vol.18, 2007, 405102 (6pp)

[34] Petit, G. A., Forrester, D. w., ―Mossbauer study of cobalt ferrites," *Physical Review B*, Vol. 4, No. 11, 1971, pp. 3912-3923.

[35] Persoons, R. M., Grave, E., Bakker, M.A., Vandenberghe, R.E., ―Mossbauer Study of the High Temperature Phase of Co-Substituted Magnetite, $Co_xFe_{3-x}O_4$. II X $\geq$0.1." *Physical Review b APS*, Vol. 47, No. 11, 1993, pp. 5894-5905.

[36] Forbes, Z. G., ―Magnetizable Implants for Targeted Drug Delivery."PhD Dissertation, Drexel university, 2005

[37] Cullity, B.D., Graham, C.D. *Introduction to Magnetic Materials*,2nd ed, IEEE press, Wiley, 2009

[38] Ferrimagnetism.URL: http://Iopscience.iop.org/0034-4885/24/1/306/pdf/0034-4885_24_1_306.pdf [cited 04/10/2010)

[39] Morrish, A. H., *The Physical Principles of Magnetism*, Wiley, New York, 1965

[40] Martin, D. H., *magnetism in solids*, 1967. MIT press, Cambridge Massachusetts.

[41] Rittidech, A, Sinthorn, N., Noisahuan, A., –The Preparation and Investigation of Magnetic Properties of Magnesium Zinc Ferrites." *American Journal of Applied Sci*, Vol. 5, No. 2, 2008, pp.142-145.

[42] Lima, E., Brandl, A. L., Arelaro, A. D., Goya, G. F., –Spin Disorder and Magnetic Anisotropy in Fe_3O_4 Nanoparticles." *Journal of Applied Physics,* 2006, Vol. 99, 13p.

[43] Kassabova-Zhetcheva, V.D., Pavlova, L.P., Samuneva, B.I., Cherkezova-Zheleva, Z.P., Mitov, I.G., Mikhov, M.T. –Characterization of Superparamagnetic MgxZn1-xFe2O4 Powders." *Central European journal of chemistry* vol. 5, pp. 107- 117, 2007

[44] Hamdeh, H. H., McCormick. Willey, R. J, Busca, G., Xia, Z., Foehrweiser, R., –Mossbauer Spectrometry Study of Magnesioferrite Particles." *J. Appl. Phys*. Vol.76, No. 2, 1994

[45] Mazen, S.A., Mansour, S.F., Zaki, H.M., –Some Physical and Magnetic Properties of Mg-Zn ferrite." *Cryst Res Technol,* Vol. 38, No. 6, 2003, pp. 471-478.

[46] Ahn, A., Choi, E. J., Kim, E.H., —Superparamagnetic Relaxation in Cobalt Ferrite Nanoparticles Synthesized from Hydroxide Precursors." *Rev. Adv. Mater. Sci*, Vol.5, 2003, pp. 477-480

[47] Spiers, H., parkin, I.P., Pankhurst, Q.A., Affleck, L., Gren, M., Caruana, D.J., Yao, J., Vaughan, G., Terry, A., Kvick, A., –Self Propagating High Temperature Synthesis of Magnesium Zinc Ferrites: Thermal Imaging and Time Resolved X-ray Diffraction Experiments." *Journal of Mater. Chem*., Vol.14, 2004, pp. 1104- 1111.

[48] Kassabova-Zhetcheva, V.D., Pavlova, L.P., Samuneva, B.I., Cherkezova-Zheleva, Z.P., Mitov, I. G., Mikhov, M.T. –Characterization of Superparamagnetic MgxZn1-xFe2O4 Powders." *Central European journal of chemistry* vol. 5, pp. 107- 117, 2007

[49] Alone, S. T., Jadhav, K. M., –Structural and Magnetic Properties of Zinc and Aluminum –Substituted Cobalt Ferrite Prepared by Co-Precipitation." *Pramana Journal of Phy*, 2008, Vol. 70, No.1, pp. 173-181.

[50] Banerjeee, M., Verma, N., Prasad, R., –Structural Properties of $Zn_{1-x}Cu_xFe_2O_4$ Nanoparticles." *Journal of material sciences*, 2007, Vol. 42, pp.1833-1837.

[51] Rittidech, A., Sithorn, N., Noisasuan, A., –The Preparation and Investigation of Magnetic Properties of Magnesium Zinc Ferrites" *American Journal of Applied Sciences*, Vol. 5, No.2, 2008, pp. 142-145

[52] Capan, Y., Jiang, G., Na, H.K., Deluca, P.P., –Preparation and Characterization of Poly (D, L-lactide-co-glycolide) Microspheres for Controlled Release of Human Growth Hormone." *AAPS Pharm SciTech*, 2003. Vol. 4, No.2.

[53] Elderidge, J. H., Staas, J. K., Meulbroek, J. A., Tice, T. R., Gilley, R. M., –Biodegradable and Biocompatible Poly(DL-Lactide –co- glycolide) Microspheres as an Adjuvant for Staphylococcal Enterotoxin B Toxoid which Enhance the level of Toxin-Neutralizing Antibodies", *Journal of Infection and Immunity*, 1991, Vol. 59, No. 9, pp. 2978-2986

[54] Lima, K.M., Rodrigues, J.M., –Poly-Dl lactide-co glycolide Microspheres as a Controlled Release Antigen Delivery System", *Braz. Journal of Med and Bio Res*, 1999, Vol. 32, pp. 171-180.

[55] Kim, B. K., Hwang, S. J., Parks, J. B., Parks, H. J. –Preparation and Characterization of Drug Loaded Polymethacrylate Microspheres by an Emulsion Solvent Evaporation Method." *Journal of Microencapsulation*, 2002, vol.19, No. 6, pp. 811-822.

[56] Gangopadhay, P., Gallet, S., Franz, E., Persoons, A., Verbiest, T., –Novel Superparamagnetic Core (Shell) Nanoparticles for Magnetic Targeted Drug Delivery and Hypothermia Treatment," *IEEE Tran on Magn*, 2005, vol. 41, No. 10, pp. 4194-4196.

[57] Forbes, Z., Yellen, B.B., Barbee, K.A., Friedman, G., –An Approach to Targeted Drug Delivery based on Uniform Magnetic Fields." *IEEE Trans on Magn,* 2003, Vol. 39, No.5, pp. 3372-3377.

[58] De, S., Robinson, D.H., –Particle Size and Temperature Effects on the Physical Stability of PLGA Nanospheres and Microspheres containing Bodipy." *AAPS Pharm Tech* 2004, Vol. 5, No. 4.

[59] Porjazoska, A., Goraconova, K., Mladenovka, K., Glavas, M., Janjevic, E.I., Cvetkovska, M., –Poly (lactide-co-glycolide) Microspheres as Systems for Controlled Release of Proteins-Preparation and Characterization" *Acta Pharm*, Vol. 54, 2004, pp. 215-229.

[60] Kopecky, f., Kopecka, B., Misikova, E., –Sorption of Copper (II) Chitosan from Solutions of Copper Sulphate, Copper Perchlorate and Copper Nitrate." *Acta Facultatis Pharmaciticae*, 2005.

[61] Liu, H., Wang, S., –Hydrodynamic Modeling of Ferrofluid Flow in Magnetic Targeting Drug Delivery.” *Appl .Math. Mech. Eng. Ed*, 2008, Vol. 29, No. 10, pp. 1341-1349.

[62] Alexiou, c, Jurgons, R., schimdt, R., erhardt, W., Parak, F., Bergemann, C., Iro, H., —Magnetic Drug Targeting-a New Approach in loco-Regional Tumor Therapy with Chemotherapeutic Agents, Experimental Animal Studies.” *HNO*, 2005, Vol.53, No. 7, pp.618-622.

[63] Plontke, S.K., Salt, A.N., –Simulation of Application Strategies for Local Drug Delivery to the Inner Ear.” *ORL J Otorhinolaryngol Relat Spec*. 2006, Vol. 68, No. 6, pp. 386–392.

[64] Sun, C., Lee, J.H., Zhang, M., –Magnetic Nanoparticles in MR Imaging and Drug Delivery.”*Adv. Drug Delivery Rev*. Vol. 60, 2008, pp. 1252-1265.

[65] Yuill,W, seeney, C., klostergaard, J., –Modeling Mass Transfer Processes for Targeting Drugs with Magnetically Responsive Nanoparticles” *Abstract in 6th Annual International Conference on Magnetic Carriers, Krems*, Austria, May 2006.

[66] Mcbain, S. C., Yiu, H. H., Dobson, J., –Magnetic Nanoparticles for Gene and Drug Delivery.” *Int. J. Nanomedicine*. 2008, Vol. 3, No. 2, pp. 169–180.

[67] Albertson, Maurice L., James R Burton., Daryl B. Simons., *Fluid Mechanics for Engineers*. Englewood Cliffs, NJ: Prentice Hall, 1960.

[68] Kuenstle, M. Michael., A Comparative Study of a Simple Building Type Situated in Three Varying Conditions Within a Single Exposure Category.URL: http:// cham.co.uk/PUC.[cited March 2010].

[69] Mabotuwana, T.D., Cheng, L.K., Pullan, A.J., –A Model of Blood Flow in the Mesenteric Arterial System.” *Biomedical Engineering*, 2007.Vol 6, No. 17.

[70] Rotariu, O., Stratchan, N. J. c., –Modeling Magnetic Carrier Particle Targeting in the Tumor Microvasculature for Cancer Treatment,” *Journal of Magnetic Materials*” Vol. 293, 2005, pp. 639-646

[71] Liu, H., Wang, S., Xu, W., Ke, Z., –Hydrodynamic modeling of Ferrofluid Flow in Magnetic Targeting Drug Delivery.” *Journal of Applied Mathematics and Mechanics*, 2005, Vol. 29, No. 10, pp. 1341-1349.

[72] Asmatulu, R, Zalich, M. A., Claus, R.O., Riffle, J. S., –Synthesis, Characterization and Targeting of Biodegradable Magnetic Nanocomposite Particles by External Magnetic Fields, *Journal of Magnetism and Magnetic Materials*.” 2005, Vol. 292, pp. 108- 119.

[73] Teixeira, A. M. R., Ogasawara, T., Nóbrega, M. C., ―Investigation of Sintered Cobalt-Zinc Ferrite Synthesized by Co-Precipitation at Different Temperatures: a Relation between Microstructure and Hysteresis Curves."*J. Mat. Res*, 2006, vol.9, No. 3.

[74] Willard, M.A, Kurihara, L. K., Carpenter, E. E., Calvin, S and Harris, V.G., ―Chemically Prepared Magnetic Nanoparticles*" International Materials Reviews*, 2004, Vol. 49, No. 3, pp. 125.

[75] Sun, C., Jerry S., Lee, H., and Zhang, M., ―Magnetic Nanoparticles in MR Imaging and Drug Delivery" *Adv Drug Deliv Rev*, 2008, Vol. 60, No.11, pp. 1252–1265.

[76] Wim H De Jong, Paul JA Borm, ―Drug Delivery and Nanoparticles: Applications and Hazards" *International Journal of Nanomedicine*" 2008, Vol. 3, No. 2.

[77] Duong, G.V., Hanh, N., Linh, D.V., Groessinger, R., Weinberger, P., Schafler, E., Zehetbauer, M., ―Monodispersed Nanocrystalline $Co_{1-x}Zn_xFe_2O_4$ Particles by Forced Hydrolysis" *J. Magn. Magn. Mater*, 2007, Vol. 311, pp. 46-50.

[78] Sershen, S., and West, J. ―Implantable, Polymeric Systems for Modulated Drug Delivery," *Adv. Drug Deliv. Rev.*, 2002, Vol. 54, pp. 1225-1235.

[79] Arruebo, M., Pacheco, F., Ibarra, M. R, Santamaria, J., ―Magnetic Nanoparticles for Drug Delivery", *Review Nanotoday*, 2007, Vol. 2, No.3.

[80] Parekh, K., Upadhyay, R. V., Belova, L., Rao, K. V.," Ternary Monodispersed $Mn_{0.5}Zn_{0.5}Fe_2O_4$ Ferrite Nanoparticles: Preparation and Magnetic Characterization." *Nanotechnology,* 2006, 17, 5970- 5975.

[81] Kotwal V. B, Saifee, M., Inamdar, N., Bhise, K., ―Biodegradable polymers: Which, when and why*?" Indian J Pharm Sci* 2007; Vol. 69, pp. 616-625.

[82] Porjazoska, A., Goraconova, K., Mladenovka, K., Glavas, M., Janjevic, E. I., Cvetkovska, M., ―Poly (lactide-co-glycolide) Microspheres as Systems for Controlled Release of Proteins-Preparation and Characterization" *Acta Pharm*, 2004, Vol. 54, 215-229.

[83] Santovena, A., Garcia, J.T., Oliva, A., Llabres, M., and Farina, J.B., ―A Mathematical Model for Interpreting In-Vivo rhGH Release from Laminar Implants," *Int. J. Pharm.*, , Vol. 309,2006, pp. 38-43.

[84] Santovena, A., Alvarez-Lorenzo, C., Concheiro, A., Llabres, M., and Farina, J.B. ―Rheological Properties of PLGA Film-Based Implants: Correlation with Polymer Degradation and SPf66 Antimalaric Synthetic Peptide Release," *Biomaterials,* Vol. 25, 2004, pp.925–931.

[85] Glynn, P.A.R., van der Hoff, B.M.E., and Reilly, P.M. *"*A General Model for Prediction of Molecular Weight Distributions of Degraded Polymers, Development and Comparison with Ultrasonic Degradation Experiments," *J. Macromol. Sci. Chem.,* Vol. A, No. 6, 1976, pp. 1653-1664.

[86] Muthu, M. S. and Singh, S. ―Targeted Nanomedicines, Treatment for Cancer, AIDS and Brain Disorders: Different Targeted Nanomedicines," *Nanomedicine*, Vol. 4, No. 1, 2009, pp. 105-118.

[87] Komarek, A. C.; Streltsov, S. V.; Isobe, M.; Möller, T.; Hoelzel, M.; Senyshyn, A.; Trots, D.; Fernández-Díaz, M. T.; Hansen, T.; Gotou, H.; Yagi, T.; Ueda, Y.; Anisimov, V. I.; Grüninger, M.; Khomskii, D. I.; Braden, M. CaCrO3: ―An Anomalous Antiferromagnetic Metallic Oxide," *Physical Review Letters*, vol. 101, Issue 16.

[88] Naiden, Z. T., ―Structure and Magnetic Properties of Mechanically Alloyed Ferrite Nanopowders." *Russian Physics Journal*, 2006, pp. 946-951.

[89] Parekh, U. B. ―Ternary Monodispersed Manganese Zinc Ferrite Nanoparticles: Preparation and Magnetic Characterization." *Nanotechnology*, 2006, pp. 5970-5975.

[90] Emami, J., ―Particle Size Design of PLGA Microspheres for Potential Pulmonary Drug Delivery Using Response Surface Methodology*," J. Microencapsulation*, Vol.99999, No.1, 2008.

[91] Gogotsi, Y. ―*Nanomaterials Handbook*," CRC Press, 2006.

[92] Hysteresis loop- ABC of electronics,
URL: www. abcofelectronics.com/ hysteresis.htm. [Cited, May 3, 2010].

[93] K.J. Whittlesey, L.D. Shea, ―Experimental Neurology", 2004, Vol.190, pp. 1-16.

[94] Conroy Sun, Jerry S.H. Lee, and Zhang, M., ―Magnetic Nanoparticles in MR Imaging and Drug Delivery" *Adv Drug Deliv Rev*. 2008, Vol. 60, No. 1, pp. 1252–1265.

[95] Parekh, K., Upadhyay, R. V., Belova, L., ―Ternary Monodispersed Mn-Zn Ferrite Nanoparticles: Preparation and Magnetic Characterization*, Nanotechnology*.' 2006, Vol. 17, pp. 5970-5975.

[96] Zilberman, M., Grinberg, O., ―HRP-Loaded Bioresorbable Microspheres; Effect of Copolymer Composition and Molecular Weight on Microstructure and Release Profile." *Journal of Biomaterials Application*, 2008, Vol. 22.

[97] Wang, L., Yang, Z., Gao, J., Xu, K., Gu, H., Zhang, B., Zhang, X., Xu, B., ―A biocompatible Method of Decorporation: Bisphosphonate-Modified Magnetite Nanoparticles to Remove Uranyl Ions from Blood." *J. A.M Chem. Soc*. 2006, Vol. 128, pp. 13358-13359.

[98] Jain, T.K., Reddy, M.K., Morales, M.A., Pelecky, L., Diandra, L., Labhasetwar, V., ―Biodistribution, clearance, and Biocompatibility of Iron Oxide Magnetic Nanoparticles in Rats." *Molecular Pharmaceutics*, Vol. 5, No. 2, pp. 316-327.

[99] Wu, P.C., Su, C.H., Cheng, F.Y., Weng, J.C, Chen, J.H., Tsai, T.L., Yeh, C.S., Hwu, J.R., Tzeng, Y., Shieh, D.B., ―Modularly Assembled Magnetite Nanoparticles enhance In-vivo Targeting for Magnetic Resonance Cancer Imaging." *Bioconjugate. Chem*. 2008, Vol. 19, pp. 1972-1979.

[100] Berry, C. C., Curtis, A. S. G., –Functionalization of Magnetic Nanoparticles for Applications in Biomedicine." *J. Phys. D: Appl Phys*. 2003, Vol. 36, R198-R206.

[101] Clarke, A.I. Braginski, *SQUID Handbook*, Weinheim: Wiley-VCH, 2003-2004.

[102] Transmission Electron Microscope.URL: http://www.tech-faq.com/transmission-electron-microscope.shtml[cited 4th April 2010]

[103] Transmission Electron Microscope.URL: http://www.unl.edu/CMRAcfem/temoptic.htm. [Cited, 4th April 2010]

[104] URL:http://nobelprize.org/educational_games/physics/microscopes/tem/index.html. [cited 4th April 2010]

[105] Cullity, B.D., Stock, S. R., *Elements of X-Ray Diffraction*. Prentice Hall, 2001

[106] Schwarzenbach, D., *Crystallography*, John Wiley& sons, 1996.

[107] Hammond, C., The basics of Crystallography and Diffraction, Oxford University Press, 2001

[108] Tilley, R., Crystals and Crystal Structures, Wiley, 2006.

[109] Giacovazzo, C., Monaco, H. L.,Viterbo, D., Scordari, F., Gilli, G., Zanotti, G,. Catti, M., *Fundamentals of Crystallography*, Oxford University press, 1992.

[110] Goldstein, J. I., Newbury, D. E., Joy, D., Lyman, C., Echlin, P., Lifshin, E., Sawyer, L., Michael, J., *Scanning Electron Microscopy and X-ray Microanalysis*, Plenum press, 1992.

[111] Lee, R. E., Scanning Electron Microscopy and X-ray Microanalysis, prentice hall, 1993.

[112] Thornton, P. R., *Scanning Electron Microscopy*, Chapman and Hall, 1968.

[113] Mossbauer.URL:http://www.chemwiki.ucdavis.edu/Physical_Chemistry/Spectroscopy/M%3Fssbauer%3A_Theory, [cited June 23, 2010]

[114] URL: http://en.wikipedia.org/wiki/transmission_electron_microscopy[cited June 23, 2010]

[115] Dannon, J., *Lectures on the Mössbauer Effect.* Notes taken by E. de Alba, X. da Silva [and] M.A. Weber, New York, Gordon and Breach, 1968.

[116] Gol'danski, V.I, Herber, E.R. *Chemical applications of Mössbauer spectroscopy*, 1968, New York academic press.

[117] Al-Ghanem, Hussain. *A Mossbauer Spectroscopy Study of Iron Catalyst*. 2002, thesis. Wichita State university

[118] Lima, E.Jr, Brandl, A. L., Arelaro, A. D., Goya, G. F., "Spin Disorder and Magnetic Anisotropy in Fe_2O_4 Nanoparticles" *Condensed Material Science Journal*," 2005, Vol.1, No.0505682.

[119] Cranshaw, T. E., Dale, B. W., Longworth, C. O. and Johnson, C. E. *Mössbauer Spectroscopy and its Applications,* 1985, Cambridge Univ. Press.

[120] Hamdeh, H. H., Hikal, W. M., Taher, S. M., Ho, J. C., "Mossbauer Evaluation of Cobalt Ferrite Nanoparticles Synthesized by Forced Hydrolysis," *Journal of Applied Physics,* 2005, Vol. 97, No. 064310.

[121] Kassabova-Zhetcheva, V. D., Pavlova, L. P., Samuneva, B. I., Cherkezova-Zheleva, Z. P., Mitov, I. G., Mikhov, M. T., "Characterization of Superparamagnetic $Mg_xZn_{1-x}Fe_2O_4$ Powders." *Central European Journal of Chemistry*, 2007, Vol. 5, No.1, pp.107-117.

[122] Hamdeh, H. H., Ho, J. C., Oliver, S. A., Willey, R. J., Oliveri, G., Busca, G., Magnetic Properties of Partially-Inverted Zinc Ferrite Aerogel Powders" *Journal of Applied Physics*, 1997,Vol. 81, No. 4.

[123] Hamdeh, H. H., Xia, Z., Foehrweiser, R., McCormick, B, J., Willey, R. J., Busca, G., "Mossbauer Spectroscopy Study of Magnesioferrite Particles." *Journal of Applied Physics*, 1994, Vol.76, No.2.

[124] Kumar, R, Majeti, N.V. "Nano and Microparticles as Controlled Drug Delivery Devices." *Journal of Pharm. Pharm*, 2000, Vol. 3, No. 2, pp. 234-258.

[125] Heller, J., "Controlled Release of Biologically Active Compounds from Bioerodible Polymers." *Biomaterials*, 1980, vol. 1, issue 1, pp. 51-57

[126] Wan, J., Cai, W., Meng, X., Liu, E., "Monodisperse Water Soluble Magnetic Nanoparticles Prepared by Polyol Process for High Performance Magnetic Resonance Imaging" *Chem Commun*, 2007, Vol. 4, issue. 47, pp. 5004-5006

[127] Cao, G., Nanostructures and nanomaterials: Synthesis, properties and applications., imperial College press,2004

[128] Bharadvaj, B. K., Mabon, R. F., and Giddens, D. P., "Steady Flow in a Model of a Human Carotid Bifurcation," *Journal of Biomechanics*, Vol. 15, 1982, pp.363-378

[129] Ku, D. N., and Giddens, D. P., "Pulsatile Flow in a Model Carotid Bifurcation" *Arteriosclerosis*, Vol. 3, 1983, pp.31-39.

[130] Kim, M. C., Kim, D. K., lee, S. H., Amin, M. S., park, H., Kim, C. J., Zahn, M., "Dynamic Characteristics of Superparamagnetic oxide Nanoparticles in a Viscous Fluid under an External Magnetic Field" *IEEE Trans. on Magnetics*, vol. 4, 2006, pp. 979-982.

[131] Furlani, E. P., Ng, K. C., "Analytical Model of Magnetic Nanoparticles Transport and Capture in the Microvasculature," *APS Phys.Rev. E*, 2006, Vol. 73, issue. 6.

[132] Darton, N. J., Hallmark, B., James, T., Agrawal, P., Mackley, M. R., Slater, N. K. H., Magnetic Capture of Superparamagnetic Nanoparticles in a Constant Pressure Micro-capillary Flow" *Journal of Magnetism and Magnetic Mat*. Vol. 321,2009, pp. 1571-1574

[133] Perktold, K., and Hilbert, D., Numerical Simulation of Pulsatile Flow in a Carotid Bifurcation Model, "*Journal of Biomechanical Engineering*, Vol. 8, 1986, pp. 193-119.

[134] Emmami. J., Hamishehkar, H., Najafabadi, A. R., Gilani, K., Minaiyan, M., Mirzadeh, H., Fakhari, A and Nokhodchi, A., "Particle Design of PLGA Microspheres for Potential Pulmonary Drug Delivery using Response Surface Methodology, *Journal of Microencapsulation*,2008,1-8

[135] Kreuter, J., "Physicochemical Characterization of Polyacrylic Nanoparticles," *International Journal of Pharmaceutics*, 1983, vol. 14, pp.43-58.

[136] Berrenbach, G., Speuser, P. P., "Polymerized Micelles and their Use as Adjuvants in Immunology" *Journal of Pharmaceutical Science*, 1976, Vol. 65, pp. 1763-1766.

[137] Fessi, H., Puisieux, F, devissaquet, J. P. Ammoury,N., and Benita,S., "Nanocapsule Formation by Interfacial Polymer Deposition Following Solvent Displacement, *International Journal of Pharmaceutics*, 1989, vol. 55, pp. r1-r4

[138] Bodmeier, R., and Chen, H., "Idomethacin Polymeric Nanosuspensions Prepared by Microfluidization" *Journal of Controlled Release*, 1990, Vol.12, pp. 223-233

[139] Kraise, H. J., Scharz, A., Rohdewald, P. "Polylactic Acid Nanoparticles, a Colloidal Delivery System for Lipophillic Drugs," *International Journal of Pharm,* 1985, vol. 27, pp. 145-155

[140] Matsumoto, A., Matsukawa. Y., Horikiri, Y., and Suzuki, T., "Rupture and Drug Release Characteristics of Multi-Reservoir Type Microspheres with Poly (dl-lactide-co-glycolide) and Poly (Dl-lactide), *International Journal of Pharmaceutics*, 2006, vol. 327(1-2), pp. 110-116.

[141] Heese, F., Robson, P., Hall, L., "Magnetic Resonance Imaging Velocimetry of Fluid Flow in a Clinical Blood Filter." *AIChE Journal*, 2005, Vol. 51, No. 9, pp. 2396-2401

[142] Sabir, M. I., Xu, X., "A Review on Biodegradable Polymeric Materials for Bone Tissue Engineering Applications." *Journal of Material Science*, 2009, vol. 44, pp. 5713-5724.

[143] Drug dictionary, *National Cancer Institute*, URL: www.cancer.gov. [Cited, June 17, 2010].

[144] Zhu, L., Ma, J., Jia, N., Zhao, Y., Shen, H., "Chitosan Coated Magnetic Nanoparticles as Carriers of 5-Fluorouracil: Preparation, Characterization and Cytotoxicity Studies." *Colloids and Surfaces B: Biointerfaces*, 2009, Vol. 68, Issue. 1, pp. 1-6.

[145] Longley, D. B., Harkin, D. P., Johnston, P. G., ―5-Fluorouracil Mechanism of Action and Clinical Strategies,' *Nat. Rev Cancer*, 2003, Vol. 3, No. 5, pp. 330-338.

[146] Luccioni, H. L. R., ―Studies on Ferrite Based Magnetic Nanoparticle Uptake and Magnetocytolysis Effects on Model Cell Cultures, *PhD dissertation*, 2009

[147] Zefeng, X., Wang, G, Kaixiong, T., Jianxing, l., Yuan, T., ―Preparation and Acute Toxicology of Nano-Magnetic Ferrofluids." Journal of Huazhong university of Scie. Tech.vol. 2, No. 1, pp. 59-61.

[148] Kirchner, C., Liedl, T., Kudera, S., Pellegrino, T., Javier, A. M., Gaub, H., Stolzle, S., fertig, N., Parak, W. J., ―Cytotoxicity of Colloidal CdSe and CdSe/ZnS Nanoparticles, *Nanoletters,* 2005 Vol. 5, No. 2, pp. 331-338.

[149] AshaRani, P. V., Mun, G. L. K., Hande, M. P., and Valiyaveettil, S., ―Cytotoxicity and Genotoxicity of Silver Nanoparticles in Humans." *American Chemical Society*, 2009, Vol. 3, No. 2, pp. 279-290

[150] Sinha, A., ―Characterizing Magnetic Particle Transport for Microfluidic Applications." *PhD dissertation*, 2008, Virginia Polytechnique Institute.

[151] Darton, N. J., Hallmark, B., james, T., Agrawal, P., Ho, V. H. B., Slater, N. K. H.,(2009a), ―On the Magnetic Field Architecture Required to Capture Superparamagnetic Nanoparticles in a Micro-Capillary Flow." *J. Nanopart. Res*. Doi:10.1007/s11051-009-9615-0

[152] Darton, N. J., Hallmark, B., james, T., Agrawal, P., Mackley, M. R., Slater, N. K. H., (2009b), ―Magnetic Capture of Superparamagnetic Nanoparticles in a Microcapillary flow." *J Magn. Magn. Mater* Vol. 321, 2009, pp. 1571-1574.

[153] Liu J, Flores, G. A., Sheng, R. S., ―In-vitro Investigation of Blood Embolization in Cancer Treatment using Magneto-Rheological Fluids." *J. Magn. Magn. Mater,* 2001, vol. 225(1-2), pp. 209-217.

[154] Sheng, R., Flores, G. A., Liu, J., ―in-vitro Investigation of a Novel Cancer Therapeutic Method Using Embolizing Properties of Magnetorheological Fluids." *J Magn. Magn. Mater*, 1999, vol. 194(1-3), pp. 167- 175.

[155] Kikura, H., Matsushita, J., kakuta, N.,Aritomi, M., Kobayashi, Y., ―Cluster Formation of Ferromagnetic Nanoparticles in Micro-Capillary Flow." *J. Mater Process Technol*, 2007, vol. 181(1-3), pp. 93-98

[156] Hallmark, B., darton, N. J., James, T., Agrawal, P., Slater, N. K. H., ―Magnetic Strength Requirements to Capture Superparamagnetic Nanoparticles within Capillary Flow." *J. Nanopart Res*, 2010, DOI 10. 1007/s1051-010-9885-6

[157] Aviles, M.O., Ebner, A. D., Chen, H., Rosengart, A. J., Kaminski, M. D., ritter, J. A., ― Theoretical Analysis of a Transdermal Ferromagnetic Implation for Retention of Magnetic Drug Carrier Particles*." J. Magn. Magn. Mater"*, 2005, vol. 293, pp. 605-615.

[158] Mahmoudi, M., Shokrgozar, M. A., Simchi, A., Imani, M., Milani, A. S., stroave, P., Vali, H., Hafeli, U. O., Bonakr, S., ―Multiphysics Flow Modeling and In-vitro Toxicity of

Iron Oxide Nanoparticles Coated with Poly (vinyl alcohol)."*J Phys Chem C*, 2009, vol. 113, pp. 2322-2331.

[159] Dynamic Light Scattering. URL: http://en.wikipedia.org/wiki/dynamic light scattering. [cited 23 June 2010]

[160] Dynamic Light Scattering. URL: http://www.chemie.de/articles/e/61632. [Cited June 20, 2010]

[161] SEM : www.uiowa.edu/~cemrf/methodology/sem/sem1.gif.[Cited June 23, 2010]

APPENDICES

Appendix 1: Raw X-ray Data for Cobalt Zinc Ferrite MNP

Two samples of cobalt zinc ferrite prepared for x-ray diffraction by co precipitation

Tuesday, September 02, 2008.

Sample name	composition	quantity
Sample 1	$Co_{0.5}Zn_{0.5}Fe_2O_4$	1
Sample 2	$Co_{0.5}Zn_{0.5}Fe_2O_4$	1

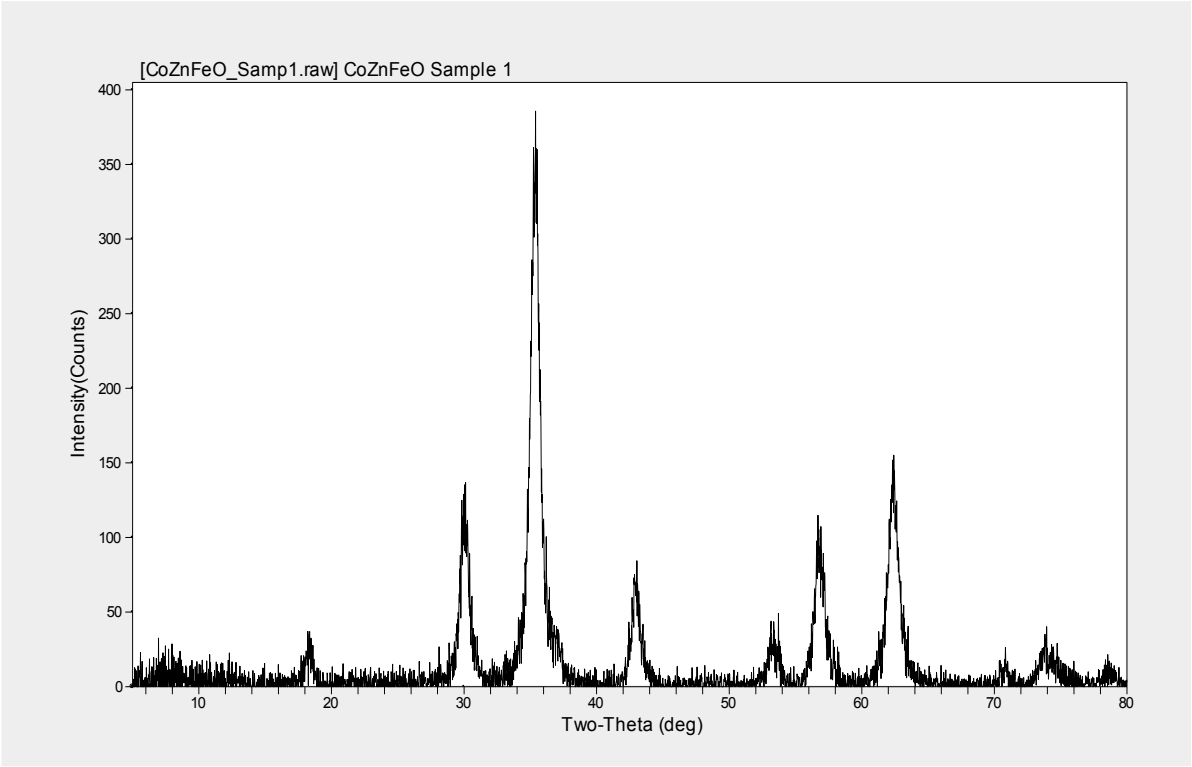

Peak ID Extended Report (7 Peaks, Max P/N = 8.8)

[CoZnFeO_Samp1.raw] CoZnFeO Sample 1

PEAK: 39(pts)/Parabolic Filter, Threshold=3.0, Cutoff=0.1%, BG=3/1.0, Peak-Top=Summit

2-Theta	d(Å)	Height	Height%	Phase ID	d(Å)	I%	(h k l)	2-Theta	Delta
30.061	2.9703	122	35.3	Chromite	2.9702	32.4	(2 2 0)	30.062	0.001
35.4	2.5336	344	100	Chromite	2.5319	100	(3 1 1)	35.424	0.024
36.982	2.4288	33	9.7	Franklinite	2.4296	6	(2 2 2)	36.968	-0.014
43.041	2.0999	77	22.3	Chromite	2.0985	21.1	(4 0 0)	43.07	0.029
56.701	1.6221	103	29.9	Franklinite	1.6217	35	(5 1 1)	56.718	0.017
62.421	1.4865	136	39.6	Magnetite	1.4857	42.8	(4 4 0)	62.462	0.041
70.842	1.3291	23	6.8	Magnetite	1.3286	3.5	(6 2 0)	70.867	0.026

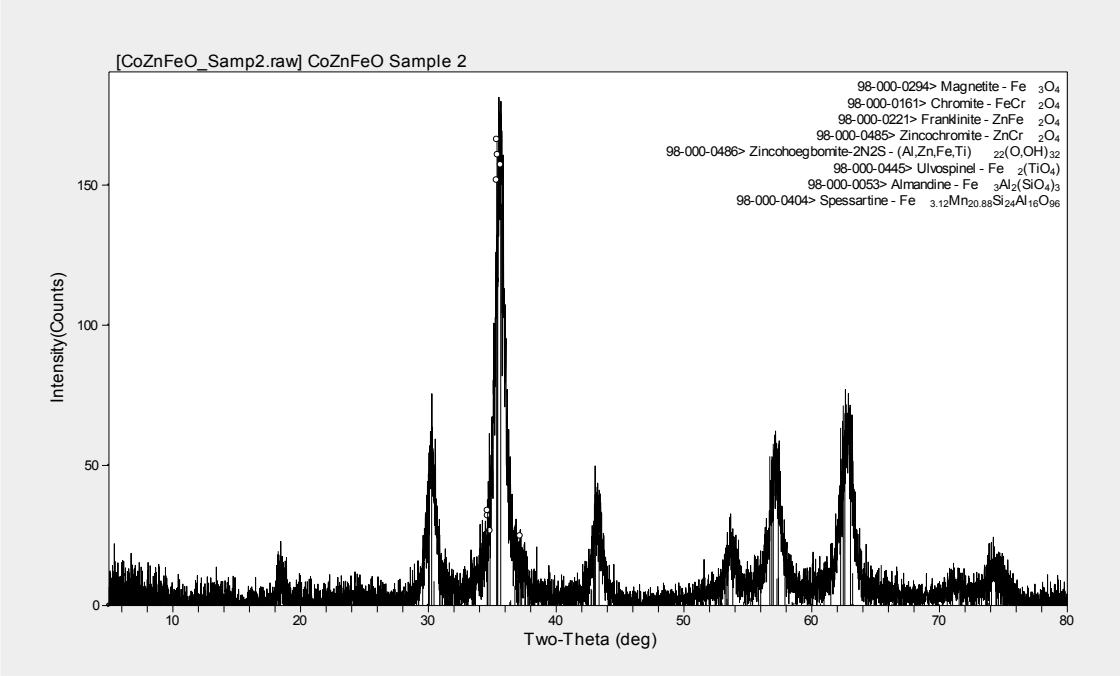

Peak ID Extended Report (17 Peaks, Max P/N = 5.8)

[CoZnFeO_Samp2.raw] CoZnFeO Sample 2

PEAK: 47(pts)/Parabolic Filter, Threshold=3.0, Cutoff=0.1%, BG=3/1.0, Peak-Top=Summit

2-Theta	d(Å)	Height	Height%	Phase ID	d(Å)	I%	(h k l)	2-Theta	Delta
30.28	2.9493	67	43.6	Zincochromite	2.9517	38.8	(2 2 0)	30.255	-0.025

30.632	2.9164	26	17	Zincohoegbomite-2N2S	2.934	34.1	(1 0 5)	30.442	-0.188
35.272	2.5425	94	61.1	Franklinite	2.5373	100	(3 1 1)	35.347	0.075
35.539	2.524	153	100	Zincochromite	2.5162	100	(3 1 1)	35.653	0.114
43.067	2.0986	34	22.1	Chromite	2.0985	21.1	(4 0 0)	43.07	0.003
43.248	2.0903	34	22.5	Chromite	2.0985	21.1	(4 0 0)	43.07	-0.179
43.382	2.0842	34	22.3	Zincochromite	2.0854	14.5	(4 0 0)	43.354	-0.027
53.279	1.718	14	9.4	Franklinite	1.7198	12.2	(4 2 2)	53.217	-0.062
53.333	1.7164	15	10	Magnetite	1.7158	9.8	(4 2 2)	53.352	0.019
56.799	1.6196	37	23.8	Zincohoegbomite-2N2S	1.6192	1	(3 0 2)	56.814	0.016
57.118	1.6113	49	32	Chromite	1.6147	35.7	(5 1 1)	56.988	-0.13
57.462	1.6024	48	31.2	Almandine	1.6041	30.6	(6 4 0)	57.397	-0.065
61.876	1.4983	25	16.5	Zincohoegbomite-2N2S	1.5008	0.5	(3 0 5)	61.763	-0.113
62.209	1.4911	30	19.7	Franklinite	1.4899	41.6	(4 4 0)	62.262	0.053
62.642	1.4818	62	40.6	Chromite	1.4829	42.5	(4 4 0)	62.589	-0.053
63.001	1.4742	63	41.4	Zincochromite	1.4737	42.1	(4 4 0)	63.026	0.024
63.208	1.4699	42	27.5	Zincohoegbomite-2N2S	1.4701	45.5	(2,0,10)	63.197	-0.011

Appendix 2: Raw data for cytotoxicity studies

PROCEDURE

11/15/2008

1 grow cells in 96 well plate
5000 cells/well/100 ul

37oC o/n

Cell count:after1:10dilute 35
?/ml 3500000
Need 50000/ml, total 10ml 0.14 Ml

2 Add particles
100ul of 5-Fu (10mg/ml) in first well, mix, then take 100 ul from first well to second well……
add 100ul medium to each well

day1	Medium												
	5-Fu	50	25	13	6.3	3.1	1.6	0.8	0.4	0.2	0.1	0.05	0.02
day3	Medium												
	5-Fu	50	25	13	6.3	3.1	1.6	0.8	0.4	0.2	0.1	0.05	0.02
day4	Medium												
	5-Fu	50	25	13	6.3	3.1	1.6	0.8	0.4	0.2	0.1	0.05	0.02
day5	Medium												
	5-Fu	50	25	13	6.3	3.1	1.6	0.8	0.4	0.2	0.1	0.05	0.02

	37oC for 1--7 days												
3	add 20 ul of MTT(5mg/ml) 37oC 6 hours												
4	change to 200 ul of 10% SDS 37oC o/n												
5	Transfer 150 ul to a new plate, read plate at OD 590												
6	result												
		OD 590											
day1	Medium	1.07	0.98	0.85	0.85	0.79	0.85	0.82	0.82	0.82	0.86	0.80	0.90
	5-Fu	0.19	0.19	0.19	0.20	0.19	0.19	0.19	0.20	0.24	0.29	0.33	0.42
day3	Medium	2.04	2.15	2.12	2.18	2.18	2.29	2.23	2.41	2.45	2.41	2.41	2.41
	5-Fu	0.07	0.07	0.08	0.07	0.12	0.17	0.17	0.21	0.29	0.35	0.45	0.53
day4	Medium	1.56	1.77	1.78	1.77	1.72	1.70	1.77	1.64	1.80	1.81	1.81	1.77
	5-Fu	0.07	0.07	0.10	0.07	0.09	0.16	0.18	0.19	0.27	0.33	0.39	0.39
day5	Medium	1.80	1.85	2.17	2.21	2.23	2.41	2.41	1.43	1.26	1.34	1.43	1.43
	5-Fu	0.07	0.07	0.07	0.06	0.07	0.14	0.17	0.19	0.23	0.26	0.29	0.35

12/11/2008													
1	grow cells in 2 of 96 well plate												
	5000 cells/well/100 ul												
	Cell count:after1:10dilute	18											
	?/ml	1800000											
	Need 50000/ml, total 10ml	0.28	ml										
	37oC o/n												
2	Add particles												
	A. Polymer + 5 Fu: 10% CoZnFe3O4, 20% 5Fu,												
	B. Polymer + 10% CoZnF3O4												
	100ul of 5-Fu (10mg/ml) in first well, mix, then take 100 ul from first well to second well……												
	add 100ul medium to each well												
	Polymer + 5Fu	50	25	13	6.3	3.1	1.6	0.8	0.4	0.2	0.1	0.05	0.02
	Polymer + 5Fu	50	25	13	6.3	3.1	1.6	0.8	0.4	0.2	0.1	0.05	0.02
	Polymer	50	25	13	6.3	3.1	1.6	0.8	0.4	0.2	0.1	0.05	0.02
	Polymer	50	25	13	6.3	3.1	1.6	0.8	0.4	0.2	0.1	0.05	0.02
	Dry	50	25	13	6.3	3.1	1.6	0.8	0.4	0.2	0.1	0.05	0.02
	Dry	50	25	13	6.3	3.1	1.6	0.8	0.4	0.2	0.1	0.05	0.02
	Medium												
	Medium												

	37oC for 3 or 6 days												
3	add 20 ul of MTT(5mg/ml) 37oC 6 hours												
4	change to 200 ul of 10% SDS 37oC o/n												
5	Transfer 150 ul to a new plate, read plate at OD 590												
6	result												
		OD 590											
	Concentration	50	25	12.5	6.25	3.1	1.6	0.8	0.4	0.2	0.1	0.05	0.02
day3	Polymer + 5Fu	0.06	0.05	0.06	0.06	0.07	0.09	0.12	0.11	0.13	0.15	0.18	0.23
	Polymer + 5Fu	0.07	0.07	0.10	0.06	0.08	0.08	0.13	0.14	0.14	0.16	0.18	0.17
	Polymer	0.28	0.12	0.09	0.07	0.12	0.23	0.41	0.52	0.64	0.64	0.84	0.88
	Polymer	0.10	0.07	0.08	0.08	0.12	0.27	0.45	0.60	0.64	0.66	0.72	0.74
	Dry	0.09	0.11	0.16	0.23	0.28	0.31	0.37	0.41	0.42	0.44	0.47	0.52
	Dry	0.10	0.12	0.15	0.21	0.23	0.27	0.37	0.41	0.44	0.39	0.45	0.58
	Medium	0.94	0.88	0.79	0.88	0.82	0.82	0.84	0.83	0.86	0.82	0.91	1.04
	Medium	0.94	0.88	0.78	0.78	0.76	0.85	1.03	0.92	0.90	0.89	0.94	1.02
	Polymer + 5Fu	0.06	0.06	0.08	0.06	0.08	0.09	0.12	0.13	0.14	0.16	0.18	0.20
	Polymer	0.19	0.10	0.08	0.07	0.12	0.25	0.43	0.56	0.64	0.65	0.78	0.81
	Dry	0.09	0.12	0.16	0.22	0.26	0.29	0.37	0.41	0.43	0.41	0.46	0.55
	Medium	0.94	0.88	0.79	0.83	0.79	0.83	0.93	0.87	0.88	0.85	0.92	1.03

	Concentration	50	25	12.5	6.25	3.1	1.6	0.8	0.4	0.2	0.1	0.05	0.02
day 6	Polymer + 5Fu	0.05	0.04	0.05	0.05	0.04	0.10	0.13	0.15	0.16	0.21	0.19	0.18
	Polymer + 5Fu	0.10	0.06	0.06	0.06	0.08	0.10	0.15	0.18	0.18	0.20	0.17	0.21
	Polymer	0.21	0.15	0.18	0.48	1.25	1.66	1.75	1.91	1.97	2.13	2.47	2.63
	Polymer	0.34	0.10	0.16	0.41	1.15	1.69	1.75	2.05	2.20	2.08	2.19	2.38
	Dry	0.70	0.65	0.84	1.00	1.12	1.23	1.43	1.75	1.62	1.96	1.96	2.24
	Dry	0.61	0.69	0.78	0.90	1.15	1.47	1.45	1.52	1.83	2.06	2.35	2.24
	Medium	2.35	2.20	2.17	2.29	2.27	2.28	2.35	2.17	2.17	2.14	2.43	2.67
	Medium	2.34	2.07	2.32	2.23	2.34	2.08	2.21	2.36	2.39	2.50	2.53	2.53
	Polymer + 5Fu	0.07	0.05	0.06	0.06	0.06	0.10	0.14	0.16	0.17	0.21	0.18	0.20
	Polymer	0.27	0.13	0.17	0.44	1.20	1.68	1.75	1.98	2.08	2.10	2.33	2.51
	Dry	0.66	0.67	0.81	0.95	1.13	1.35	1.44	1.64	1.73	2.01	2.16	2.24
	Medium	2.35	2.13	2.24	2.26	2.31	2.18	2.28	2.27	2.28	2.32	2.48	2.60

12/11/2008

1 grow cells in 2 Chanber slide

10000 cells/well/200 ul

37oC O/N

2 Add 20 or 10 or 5 ul of polymer or polymer+ 5 Fu into wells

polymer + 5Fu	20	10	5	0
polymer	20	10	5	0

37oC 3 or 6 days

3 grow blood cells in a chanber slide

200ul/weel

polymer	20	10	5	0
polymer	20	10	5	0

37oC 3 days

APPENDIX 3:

Nanocomposite Fabrication procedure

Take a polymer PLGA (Poly (DL-lactide-Co-glycolide) 50:50 m (wt 40,000-75000) and grind in a Petri dish. Measure 0.0625g of PLGA and add to 5ml of a solvent (Acetonitrile) in a small cylinder with a stopper. Insert a small magnet in the cylinder. Place the cylinder with the stopper on to a mixer at 7000rpm for 30 minutes. While phase one is running, pipette 40ml of paraffin into a tall beaker and add 2ml (5% of PLGA) of Span 80(surfactant). Place the beaker under a blade mixer. Set up the burette to allow for addition of phase 1 into the beaker. Run the blade mixer at 7000 rpm.

Remove phase 1 from the mixer and remove the magnet. Add 0.00625 g (10% of PLGA) of magnetite nanoparticles and place the beaker in a sonicator to disperse the mixture for 10minutes. Using the pipette add 3ml of phase 1 through the burette drop wise into phase 2. Allow the mixer to run for 1hr and 30min. Collect the sample in a centrifuge tube and top up with paraffin. Fill another tube with paraffin (same viscosity) to balance in the centrifuge. Centrifuge the sample at 17000rpm for 20 minutes at 10 deg Celsius. Drain the paraffin and repeat 3 times for 15 minute with100 ml hexane with 5ml (5%) petroleum mix to remove the surfactant. Add 5% carbon tetrachloride and 50ml hexane and sonicate for 5-10 minutes (CCL) The sample is then filtered, dried and stored in the refrigerator.

APPENDIX 4

Raw Data for Magnetization analysis

SAMPLE	% OF Cobalt Zinc Ferrite	% OF DRUG
T_1	10	0
T_2	15	0
T_3	20	0
T_4	25	20

APPENDIX 5:

MODELING MAGNETIC CAPTURE

Theoretical background

Recent developments in magnetic drug targeting have largely focused on how to improve the efficiency of MNP encapsulated in polymeric or inorganic coatings [60]. MNP can be introduced into the blood stream intravenously and be guided to the target site by use of a magnetic field. Results from one study estimate that up to 26 times higher drug concentrations can be achieved with magnetic targeting compared to usual systemic methods of drug delivery [61]. The ability of the therapeutic agents to access the target site effectively depends on physicochemical properties of the drug loaded MNP, field strength and geometry, depth of the target tissue, rate of blood flow and vascular supply [62, 63].

Computational fluid dynamics (CFD) approaches can help us understand the fluid flow mechanism of MNP introduced in the blood vessel in the presence of a magnetic field, compare the CFD simulations with the experimental data and to investigate the effect of magnetic capture on the flow characteristics of the blood. CFD techniques offer insight into the mechanism of time varying fluid flow in human arteries. This knowledge can be harnessed to improve magnetic capture and drug delivery. In this chapter, we focus on studying how the size of the blood vessels, the strength of the magnetic field and the velocity of the fluid within the vessels affect the delivery of the therapeutic agents.

Various fluid flow CFD simulations have been carried out by different groups to study the fluid flow behavior. We also have various numerical techniques available in the research

field including finite element (FEM), finite volume (FVM) and finite difference methods (FDM) used to solve fluid dynamic equations. The earliest group to focus on fluid flow in blood vessels was by Bharadvaj et al. [128] who created a model with glass to study the geometry of carotid bifurcation. Using hydrogen bubbles and a dye Bharadvaj's group modeled steady flow with visible streak lines. Subsequent work using the same model was conducted by Ku et al. [129] with emphasis on pulstile flow mechanism.

A fast solving technique combined with finite element method has been used by Kim et al. [130] in 2006 to analyze the dynamic characteristics of SPION in a viscous fluid under a magnetic field. Furlani et al. [131] have developed an analytical model for predicting the transport and capture of therapeutic magnetic nanoparticles in the human microvasculature. Experimental work on in-flow magnetic capture has been carried out by Darton et al. [132] to study the capture behavior within transparent plastic micro capillary arrays. Forbes et al. [65] have analyzed particle trajectories and aggregate stability (including particle interactions) attracted to anchors of equivalent physical characteristics as the injected MNP.

The CFD modeling of blood flow in a vascular system constricted by accumulation of therapeutic molecules is investigated in this work. Previous work on one dimensional modeling of blood flow has fallen short of coming up with a single model which can fully capture all aspects of the hemodynamic of the human vascular system [66, 68]. This has been due to the non linear nature of blood flow, a complex vascular system that can regulate it and the anomalous nature of the blood itself compared to a typical fluid [68]. Literature is sparse on the effects of magnetic capture on the flow characteristics of the blood.

When MNP- drug carriers are injected into the blood stream, they are carried by the blood towards the target region of interest. A magnetic field is used to capture the drug encapsulated magnetic spheres in the target region of the blood vessel. The MNP will accumulate within the vessel at this point causing a constriction in the size of the blood vessel. The regular speed and pressure in this region will be affected by the accumulation of the magnetic nanocomposite` spheres.

In this model, the blood was assumed to be an incompressible, homogenous Newtonian fluid with a laminar flow and having a constant viscosity. This assumption was made because experimental work on magnetic drug targeting was carried out in such a fluid and the need to reduce the number of variables in our CFD analysis. This Newtonian flow was first numerically simulated by Perktold et al. [133] in 1986. They considered both two and three dimensional carotid bifurcations for a Reynolds number of 100 and higher. Their investigation showed minor differences between Newtonian and non-Newtonian flow patterns.

The blood vessels in the human body have wide differences in size and shape and are assumed to have a cylindrical shape with a diameter in the capillaries and arteries having a luminal diameter in the range of d=12μm to 39 μm [69]. The velocity of the blood in the arteries is pulsatile and varies depending on the location within the body. This velocity was assumed to be within the normal actual velocity of blood in arteriole and capillaries, i.e. 1.0mm/s $\leq V_0 \leq$ 10 mm/s [69]. In this study, we considered three dimensions of the blood vessels. Their diameters were; 0.3125cm, 0.23cm and 0.135 cm

The magnetic particles considered in this model were composed of $Co_{0.5}Zn_{0.5}Fe_2O_4$ and magnetite (Fe_3O_4) the diameter of the MNP was found to be around 10 nm with a saturation

magnetization of around 78 (emu/g) for magnetite [6]. The magnetic field applied to the MNP at the target region was in the range of 0.3Tesla to 1.2 Tesla. This field is applied perpendicular to the direction of blood flow in order to maximize the magnetic capture.

Introduction

The use of magnetic fields to guide and capture MNP and MNC spheres in targeted drug delivery system has been under investigation for over three decades [156]. Experimental and clinical trials have been carried out to determine the suitability of this method in drug delivery [6]. Current research methods have increased the understanding and knowledge of the fluid flow phenomena in human vasculature through various numerical and computational modeling techniques.

The nature of the fluid flow model depends on the basic assumptions of the type of flow and the complexity of the vasculature. Studies carried out by Furlani et al [131], Liu et al. [153], Aviles et al [157], Mahmoudi et al. [158] and many others have varying assumptions on the path and nature of the flow. This research assumes a simple model of fluid flow within a straight cylindrical vessel of specified diameters subject to the effects of a magnetic field. Of interest in this study is the effect of vessel constriction on the pressure and velocity profile at the region of constriction and its implication on the fraction of the magnetic materials captured.

Governing Equations

A particle flowing in a fluid confined to vessel of varying cross-section and length experiences a change in velocity, direction and pressure. The change affects the kinetic, gravitational and mechanical potential energy of the particle. By the principle of conservation of energy (E) we can express changes in an equation as;

$$\frac{E}{m} = \frac{PV}{m} + \frac{1}{2}v^2 + gZ = constant \quad (1)$$

where V represents the average velocity, ν is the velocity of the particle and m the mass of the particle.

Assuming an incompressible fluid flowing from one point of the vessel to the other end say point 1 to point 2, then we can rewrite Equation (6.1) to form the Bernoulli's equation given by,

$$\frac{E}{V} = -p_{1+\frac{1}{2}}\rho v_1^2 + \gamma_1 = p_2 + \frac{1}{2}\rho_{\frac{2}{2}} + \gamma_2 \quad (6.2)$$

In this equation, P represents the static pressure, $P + \rho\frac{v^2}{2}$ is the dynamic pressure and γ is the hydrostatic pressure. To account for a differential change in displacement the Bernoulli's equation can be written in the form;

$$\frac{d}{dx}\left(p + {}^1\!/_2\,\rho v^2 + \gamma\right) = 0 \quad (6.3)$$

by differentiation, Equation (6.3) takes the form;

$$\rho a_x = -\frac{\partial P}{\partial x} - \gamma\frac{\partial Z}{\partial x} \quad (6.4)$$

The forces acting on the fluid along the flow direction equals to the sum of the gradient of both the static and hydrostatic pressures in the same direction. This is represented by the Equation (6.5).

$$\frac{F_x}{V} = \frac{\partial P}{\partial x} - \gamma\sin\theta \quad (6.5)$$

Bernoulli's principle when extended to 2 or 3 dimensional domains could be used to solve the time averaged Navier-Stokes equations. For an incompressible laminar flow of a Newtonian fluid, the Navier –Stokes equation can be written as:

$$\frac{\partial}{\partial t}u + u \cdot \nabla u = -\nabla P + v\Delta u + f \tag{6.6}$$

where u, P, v and f are the fluid velocity, pressure, dynamic viscosity and body forces, respectively.

Model Geometry and Boundary Conditions

The fluid flow model considers the acceleration of a fluid of viscosity ρ carrying the MNP through a constriction in a cylindrical vessel of diameter D_1. Before the constriction, the fluid has a pressure P_1 and flow with a velocity V_1. When a magnetic field is applied, the MNP will accumulate at the region of capture causing a constriction in the vessel diameter. The degree of constriction will depend on the mass flow rate of the fluid and the strength of the magnetic field. At the constriction, the fluid will have a velocity V_2 and pressure P_2 as shown in Figure 6.1.

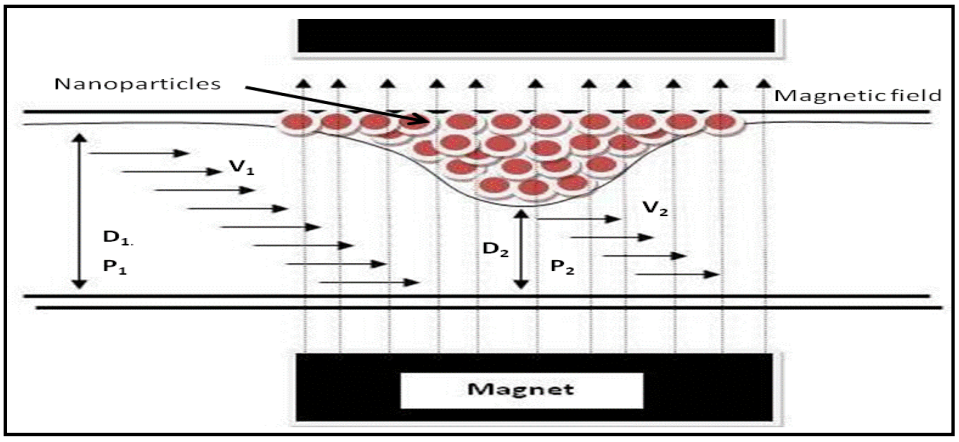

Figure 6.1 Schematic shows internal flow through a constriction due to the presence of a magnetic field gradient.

Three different models of magnetic capture were examined under continuous flow conditions. In case 1, the diameter of the vessel was 0.23 cm with a notch at the center due to magnetic capture of nanoparticles reducing the cross-section by ½ the total cross-section. The diameter in case 2 was 0.135 cm with cross section decreased by ¼ while the diameter in case 3 was 0.3125 cm with the diameter decreased by ½. The vessels had a constant length of 4 times the diameter before the notch and 16 times the diameter after the notch. The vessels were assumed to be inelastic or rigid with the diameter at the inlet equal to the diameter at the outlet. This geometry is illustrated in figure 6.2.

The fluid flow rate within the three vessels was kept 10ml/s. This fluid was considered incompressible and with a density of about 1125 kg/ m^3. In these simulations, the velocity was constrained in the axial direction. The notch used in the three models had a fixed diameter of 2.56 cm.

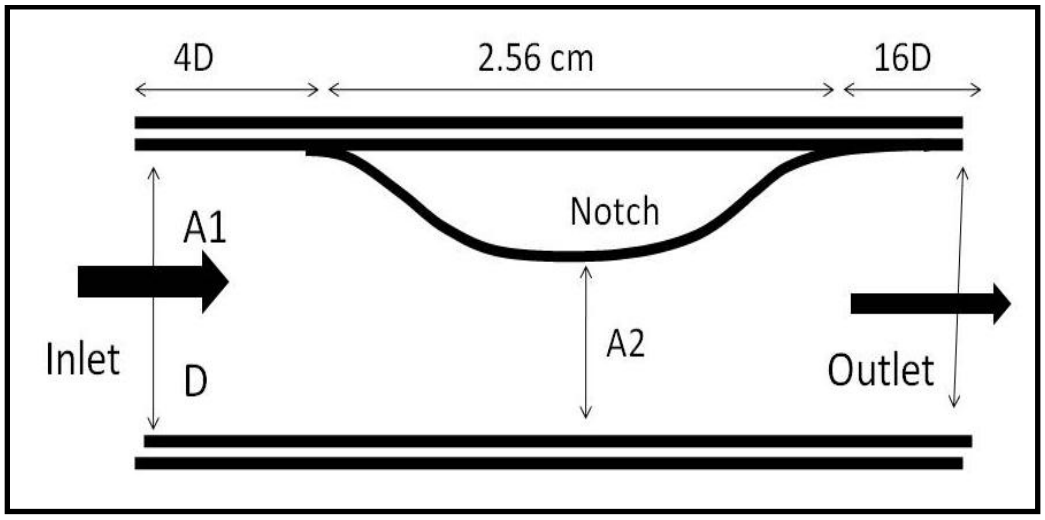

Figure 6.2 Schematic of the blood vessel used in the meshing of the geometry

The CFD simulation was carried out using the CFD solver Fluent. Using GAMBIT, a computer aided design (CAD) package, the model was prepared by building a mesh to divide the domain into discrete cells. By applying a numerical algorithm, the Navier-Stokes partial differential equations are solved iteratively. From the numerical data obtained a graphic representation of the three schemes used was obtained.

Results and Discussion

From the model results, the axial velocity profiles were obtained. Figure 6.3 shows the axial velocity profile of the vessel of diameter 0.23cm and constricted by ½ at the notch. The profile depicts a more flattened peak suggesting that the flow has some turbulence. The head of the flow profile has an average velocity of 9m/s suggesting larger section of the fluid is travelling at this velocity. The velocity decreases on both sides in contact with the wall due to no slip condition. The lower centerline velocity compared to the entrance velocity could be due to pressure build up just before the notch due to the constriction causing a decrease in velocity.

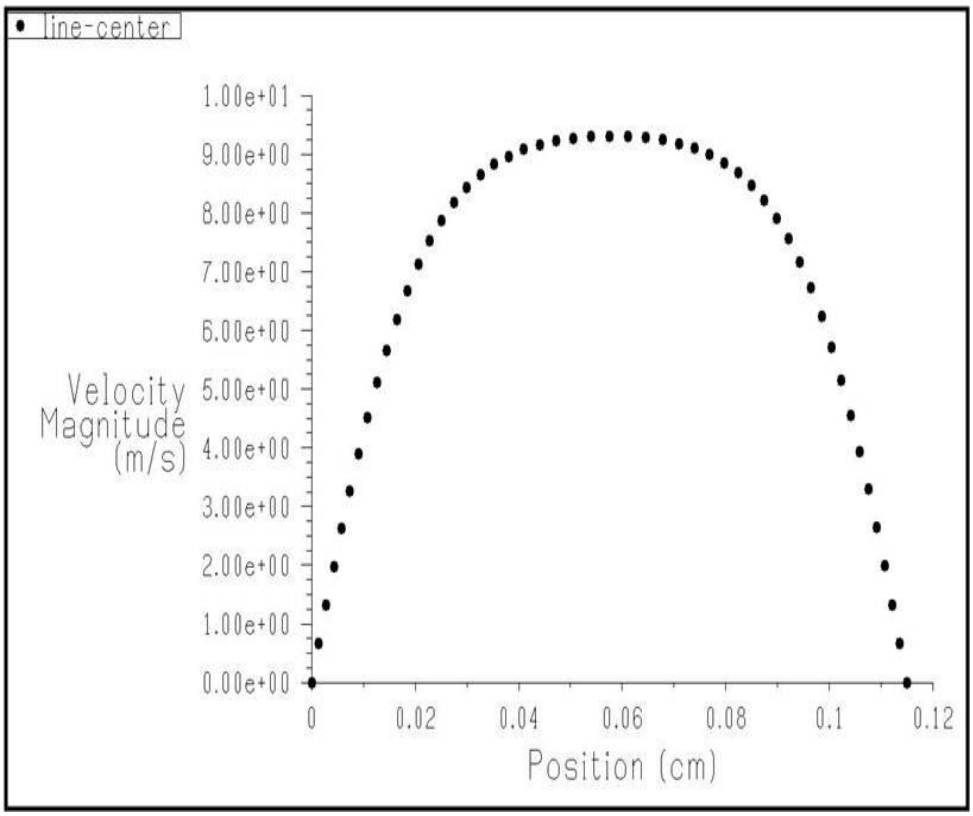

Figure 6.3 Axial velocity profiles at the centre for the vessel in case 1 with diameter constricted by 1/2.

In Figure 6.4, the vessel of diameter 0.135cm at the entrance is constricted by ¼ giving a diameter of 0.09cm at the notch. What is observed is a fully developed velocity profile with a centerline velocity at 12m/s. This velocity is higher than the entrance velocity and is due to the vessel constriction and the fluid compensates by accelerating. The shear force exerted by the walls causes a reduction in the speed on both sides of the wall forming a parabolic profile. The increased velocity at the centerline is compensated thus by a decreased velocity towards the wall.

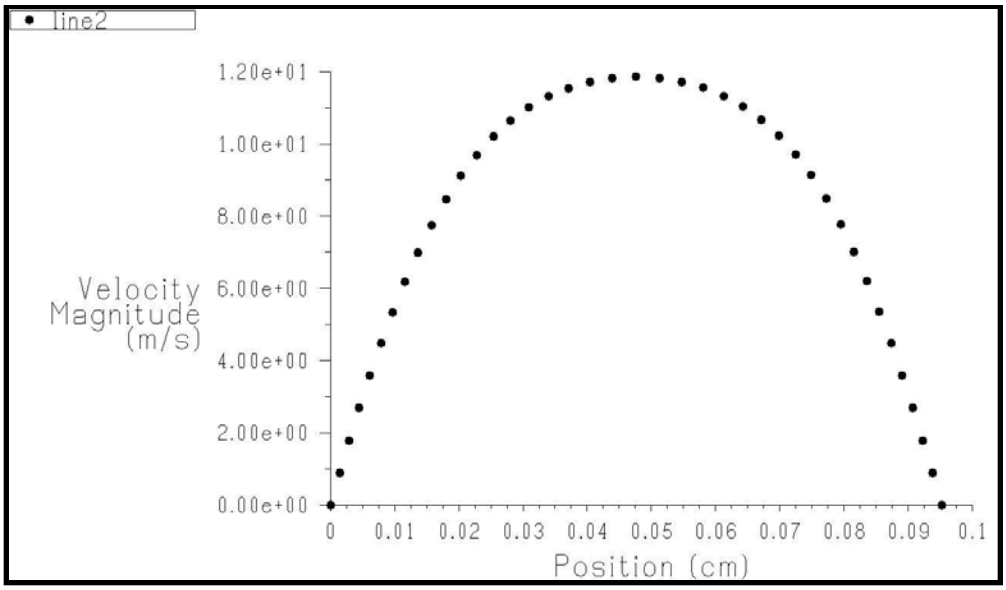

Figure 6.4 Axial velocity profile at the centre for case 2 where the diameter is constricted by ¼.

A comparison of the two profiles suggests that increasing the constriction on the flow profile has an effect on the flow characteristics. In our case, a larger constriction changed the flow from a laminar to turbulent, the center line velocity increases and the profile changed from flattened to parabolic shape. The following analysis was done to compare the effects of the notch on the fluid flow behavior at the exit. Figure 6.5 shows the velocity profile of a vessel of cross section diameter 0.23 cm while Figure 6.6 shows a vessel with cross-section diameter 0.135cm. These two profiles were obtained from the section near the exit after the notch. Figure 6.5 shows a fully developed laminar flow profile with a centerline velocity of 5.6m/s. The profile is observed to have a sharper peak indicative of the effects of shear force on the flow. The drop in velocity is attributed to the increased cross-section at the exit. For a smaller cross-section shown in Figure 6.6, the profile is more rounded suggesting increased turbulence due to a higher speed of about 8.5m/s at the centerline.

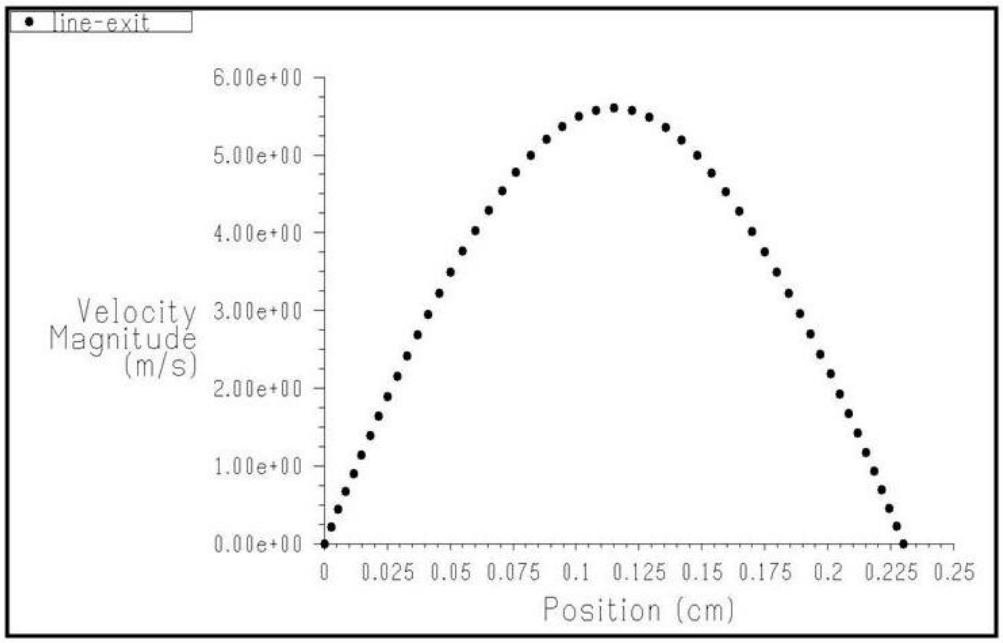

Figure 6.5 Axial velocity profiles near the exit for case 1 with a cross-section diameter of 0.23 cm.

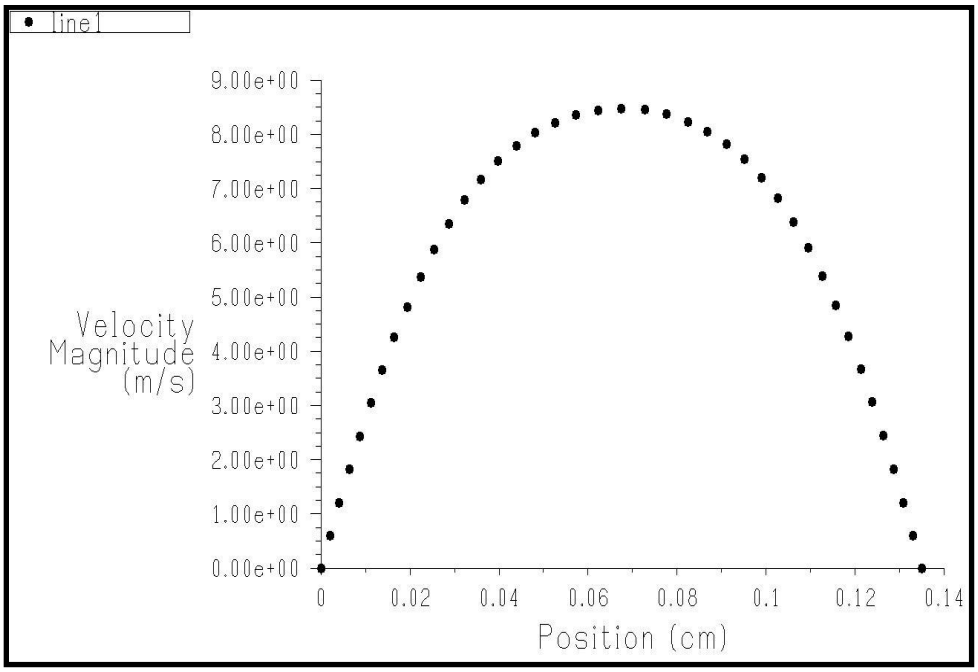

Figure 6.6 Axial velocity profiles near exit for case 2 with a cross-section diameter of 0.135 cm.

Figures 6.7 and 6.8 show the pressure and velocity contours of the vessel of diameter 0.23 cm in case 1 having its central region constricted by 1/2. An analysis of the profile reveals that the pressure was highest at the inlet and lowest at the center while the velocity was highest at the center. This trend is also observed in pressure and velocity contours in Figure 6.9, Figure 6.10 for case 2, and Figure 6.11, Figure 6.12 for case 3.

Figure 6.5 shows the velocity contours for a vessel whose cross-section diameter is decreased by ½. The image show a higher pressure at the entrance which decreases as you approach the constriction. The lowest pressure is observed at the notch. What is observed is that the pressure increases slightly after the notch towards the exit. This lower pressure is due to the increase in cross section after the notch. This pressure changes affects the velocity profile observed in Figure 6.8.

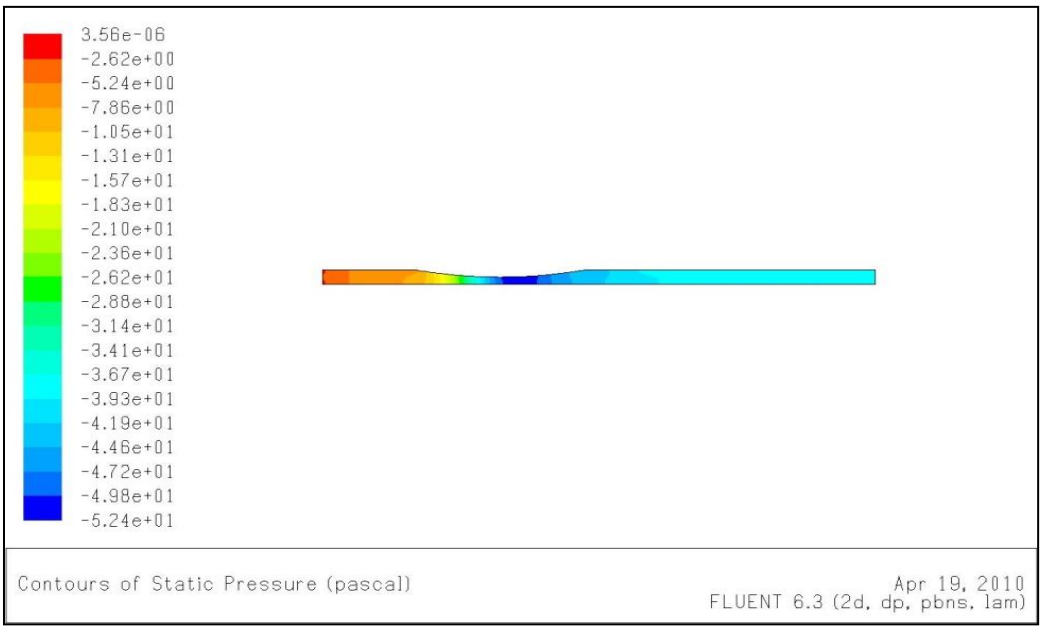

Figure 6.7 Contours of static pressure for the vessel in case 1 with diameter 0.23 cm with diameter reduced by 1/2 at the center.

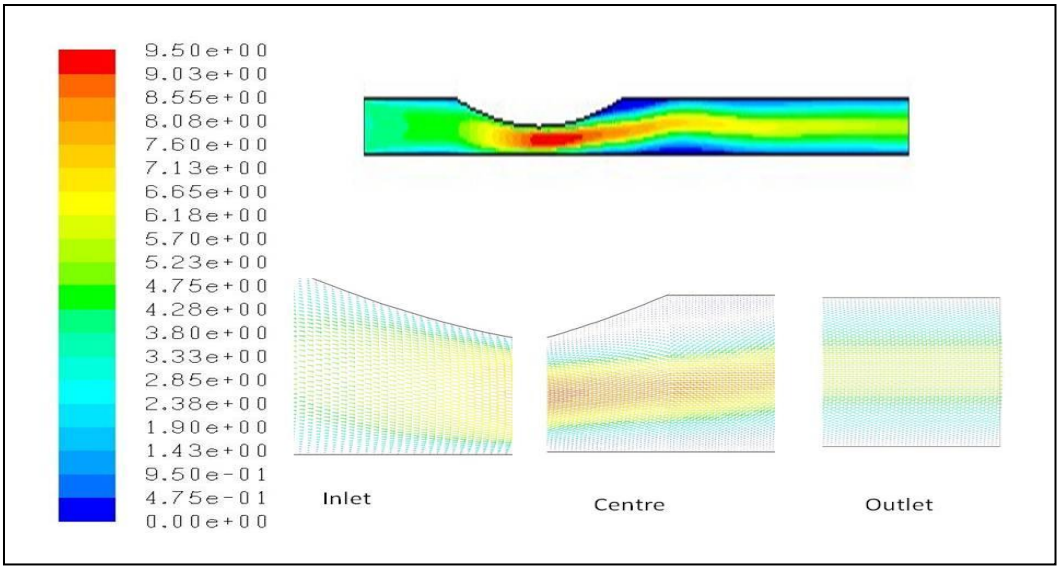

Figure 6.8 Contours of velocity magnitude for a vessel in case 1 of cross-section diameter equal to 0.23cm and constricted by ⅛ the tube diameter.

Note that there is a low velocity pocket with values close to zero just after the notch with a higher velocity at the centerline leading to formation of turbulence. For a cross-section that has a smaller constriction as in case 2, the effects of turbulence are not prominent. The pressure build up just before the notch in Figure 6.9 is lower than in case 1. The velocity contours for case 2 (Figure 6.10) show a much higher velocity at the constriction than in case 1 due to the smaller tube diameter and smaller constriction. There are no pockets of zero velocity in this profile and depicts a more laminar flow throughout the entire length of the vessel.

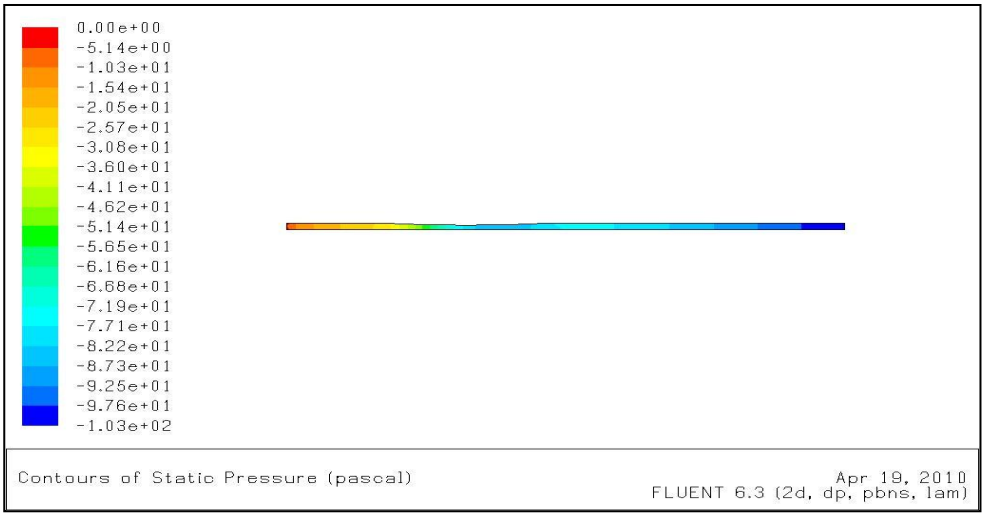

Figure 6.9 Contours of static pressure for case 2 for a tube of cross-section diameter equal to 0.135cm and a constricted by ¼ the tube diameter.

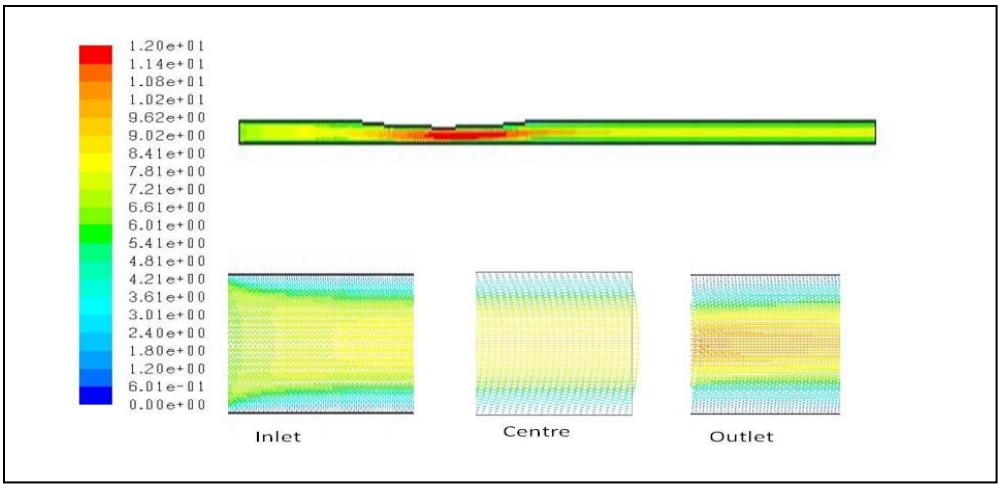

Figure 6.10 Contours of velocity magnitude for a vessel in case 2 of cross-section diameter equal to 0.135cm and a constricted by ¼ the tube diameter.

In the third case, the vessel of cross-section 0.31cm is also constricted by ½.when compared to case 1, we observe increased turbulence in both pressure and velocity contours. There are prominent pockets of low velocity indicative of increased shear forces with the wall.

The presence of low velocity may suggest the formation of eddy currents in the flow after the constriction. Note that the centerline velocity is very high next to the constriction fueling the turbulence. This fluid flow behavior is significant as it affects the percentage of magnetic materials that will be retained at the notch. The presence of eddy currents after the notch increases the hydrodynamic forces in this region. A particle on the outer layer of the notch under lower magnetic force for due to the proximity of the magnet will easily be dislodged.

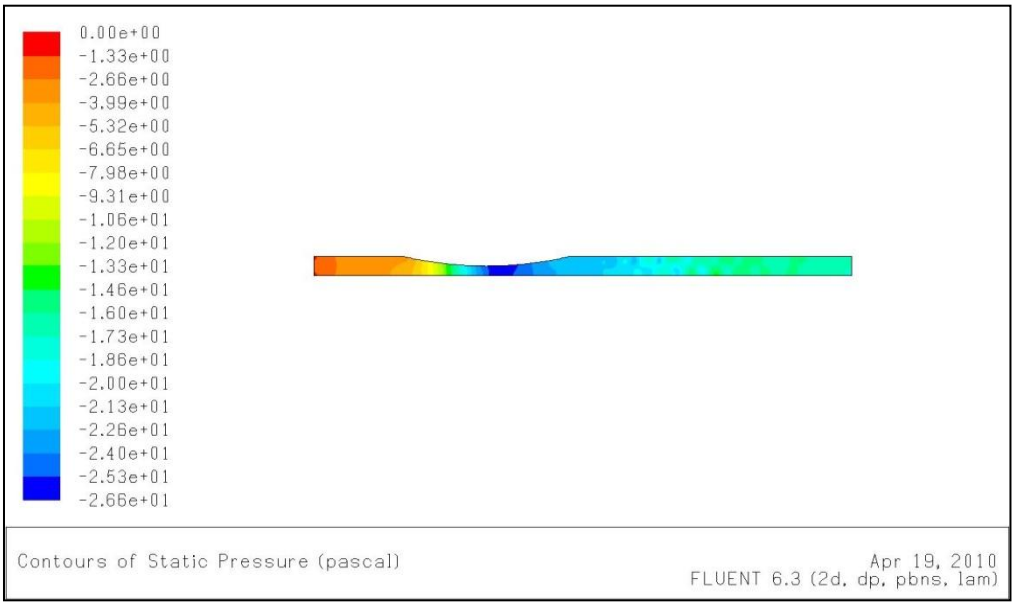

Figure 6.11 Contours of static pressure for case 3 for a tube of cross-section diameter equal to 0.31cm and a constricted by ½ the tube diameter.

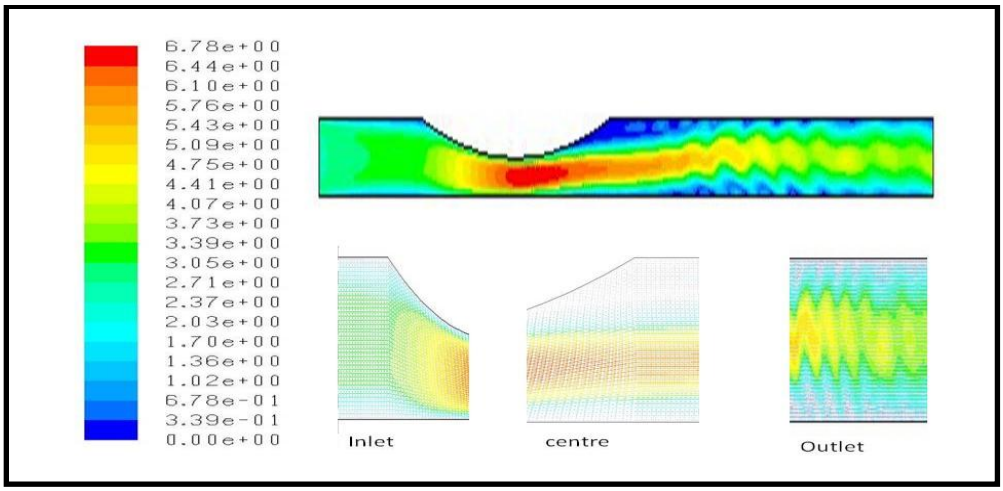

Figure 6.12 Contours of velocity magnitude for a vessel in case 3 of cross-section diameter equal to 0.31cm and a constricted by ½ the tube diameter.

Conclusion

This study has been motivated by the desire to understand the fluid flow mechanism in a hemodynamic system that may be used for targeted drug delivery. In the study, the three cases of vessel constriction were modeled using FLUENT. The axial velocity profiles, velocity and pressure contours were modeled using 2D geometry.

A close examination of the axial velocity profiles reveals a variation in the velocity with high velocity observed with decreasing vessel size in order to maintain the same pressure gradient. The velocity and pressure contours in the three vessels show variation due to the different cross-sections which affect the fluid flow behavior at the vessel inlet, centre and the outlet. The results show the increased velocities and decreased pressure for the tube with larger constriction leads to formation of turbulence just after the notch. The eddy currents formed increase the hydrodynamic forces acting on the captured particles. The outer most particles will be dislodged by the hydrodynamic forces. This decreases the percentage of the magnetic material captured.